PARTICLE IDENTIFICATION TECHNIQUES AND STUDIES OF PARTICLES USING THEM

JAMES N. BUNCH

Keble College

This thesis is submitted in partial fulfilment of the requirements for the Degree of Doctor of Philosophy at the University of Oxford

March, 1976

ACKNOWLEDGEMENTS

I would like to thank all those people who have assisted in some way in the production of this thesis. In particular my thanks are due to the following:

Professor Sir Denys Wilkinson for giving me a place in the Oxford Nuclear Physics Department.

The SRC for giving me a grant to enable me to do this research.

My Supervisor, Dr. W.W.M. Allison for the constant enthusiasm and encouragement he has shown towards me.

Dr J.H. Mulvey for much help in my first year in the Department.

Dr J.L. Lloyd for many interesting discussions.

My friends and fellow graduates, particularly J.H. Cobb and R.W. Pleming, for their help and interest.

The members of the ISIS group not mentioned so far, C.B. Brooks, P.D. Shield, M. Flinn, R.H. Giles, M.W. Walker, whose ideas and hard work have made it possible to perform the experiments described in this thesis, and with whom it has been a pleasure to work.

Mrs Leslie Cosier for producing the diagrams so beautifully.

Mrs Ina Godwin for typing and putting together this thesis so expertly.

Finally, I would like to express my gratitude and affection to my parents for contributing so much towards my education.

CONTENTS

CHAPTER IV

THE NAL EXPERIMENT

CHAPTER V

THEORETICAL CALCULATIONS OF ENERGY LOSS

CHAPTER VI

COMPARISON OF EXPERIMENT AND THEORY

APPENDICES

ABSTRACT

Experimental measurements of the ionization loss caused by charged particles moving with relativistic velocities as they pass through thin samples of gas are presented. These data are the result of three experiments where gas samples of 1.5 cm of Argon or Xenon (mixed with small quantities of other gases) were placed in a beam of pions, protons and electrons whose momenta covered the range such that $p/m_o c = 1$ to 50,000 (where p = momentum, m_o = rest mass).

The shape of the ionization loss distributions obtained, and the size of the 'relativistic rise' of ionization loss with particle velocity are compared with new Monte-Carlo theoretical calculations. The agreement between experiment and theory is shown to be good, as compared with previous theories, where significant discrepancies were observed with thin samples of gas.

The theoretical model is also used to make predictions of ionization detector properties.

CHAPTER I

INTRODUCTION

I.1 INTRODUCTION

This thesis is the description of experimental work and analysis the author has helped carry out from 1972-1975. Most of this work is motivated by the underlying question: How does one identify charged particles at very high energies? As particle velocities approach the speed of light, conventional methods for identifying charged particles become increasingly difficult or, in some cases, impossible without modifications being made. For instance, for bubble chamber techniques to be still feasible when an incident beam momentum of, say, 200 GeV/c is used, giving secondaries each with momentum typically less than ~ 50 GeV/c, it is necessary to use external detectors which could assist in identifying and in measuring the position of the secondaries emerging from the bubble chamber. Incident beam momenta of this magnitude are typical of the FNAL and CERN-SPS accelerators. It is with the idea of building a detector which could assist in particle identification that the following investigations have been carried out.

In the relativistic region of $p/m_0c \approx 5 \rightarrow 200$, ($p$ = momentum, m_0 = rest mass), just where identification methods appear so difficult, there exists a measurable property of charged particle velocities. It is found that if a charged particle is passed through a sample of gas, the amount of ionization produced in the gas is dependent on the particle's velocity. This is caused by the relativistic change in shape of the particle's electromagnetic field as its velocity gets nearer and nearer the speed of light. A more detailed description will be given later.

Three experiments are described in this thesis which investigate this phenomenon of ionization loss at relativistic velocities. The first

was an experiment performed at the Stanford Linear Accelerator Laboratory (SLAC) in 1972, whose prime aim was to measure transition radiation (which incidentally is a possible method of particle identification at ultra relativistic velocities[1,2], i.e. $p/m_o c \geqslant 200$). However, since all the apparatus and conditions required for ionization measurements are the same as for transition radiation, both phenomena were measured. The results of this SLAC experiment are not as good as was hoped for, because it was found impossible to get a consistent calibration to a high degree of accuracy. Consequently it became apparent that a very detailed analysis was not justified, and in this thesis a very small sample of the data is presented from which useful ionization information can be obtained.

The second experiment was performed at the Rutherford High Energy Laboratory (RHEL) in 1973. Its main purpose was to test a prototype detector capable of measuring both the ionization loss of a charged particle and its position. Most of the time in this experiment was used for testing the position sensitive properties of this detector. As a subsidiary experiment, measurements were made, using a different detector, of ionization loss in gas for various charged particle velocities. Conditions were not optimized however for this experiment, and so the accuracy of the results leaves something to be desired. Again there is no justification for an involved description of the analysis.

A third experiment was performed at the Fermi National Accelerator Laboratory (NAL) in 1974, whose main aim was to measure ionization loss in gas accurately, and to find how good particle discrimination is at various energies using this technique. As will be seen, the experiment was fairly successful and it provided information over a wide range of particle velocities.

Besides the three experiments mentioned above, this thesis describes the results of theoretical predictions of ionization loss and the methods

1 atmosphere) are being used the theory as previously developed contains assumptions that do not apply to our case. Consequently a Monte-Carlo technique for handling the theory has been developed.

In the final chapter, comparisons of theory with experiment are summarized.

Much of the work in this thesis follows on from the work described in J.H. Cobb's thesis[3] to which many references will be made. The group at Oxford currently working on particle identification techniques by ionization methods is known as the ISIS group, (Identification of Secondaries by Ionization Sampling). The members of the group are W.W.M. Allison, C.B. Brooks, J.N. Bunch, J.H. Cobb, P.D. Shield and R.W. Pleming.

I.2 WHAT IS IONIZATION LOSS ?

When a charged particle passes through a medium, an electromagnetic interaction can occur between the charged particle and an atom in the medium, resulting in a transfer of energy from the charged particle to the atom. The atom becomes excited or, if enough energy is transferred, it can become ionized. The total energy transferred in the collision processes that result in ionization of the medium, is the quantity measured in the experiments described in this thesis.

In these experiments the medium corresponds typically to a 1.5 cm sample of Argon gas at atmospheric pressure. A relativistic charged particle would make on average about 50 collisions on its way through the gas, but since the process is a statistical one, the number of collisions for repeated traversals of the sample will obey a Poisson-type distribution centred about fifty.

In a collision with an Argon atom the most likely result is the production of an ion pair, i.e. $(Ar^+ e^-)$, with a kinetic energy of a few

eV, this amount depending on the closeness of the collision. The incident charged particle momentum (typically of magnitude 25 GeV/c) will effectively be unchanged by the collision.

It is clear from the above that the probability distribution of ionization loss seen in a sample of gas is the convolution of two probability distributions, i.e. the probability of producing a certain number of collisions, and the probability of the electron freed in each collision having a particular energy. This results in a very wide distribution with a significant tail going to very high energies. It is called the Landau distribution after L. Landau[4], who first calculated it theoretically. Fig.1.1 shows examples of such a distribution for 25 GeV/c protons and electrons (the protons are the peak at lower energy loss). Their width/peak ≈ 100%. The high energy tail corresponds to the small but finite probability of collisions producing very high energy electrons.

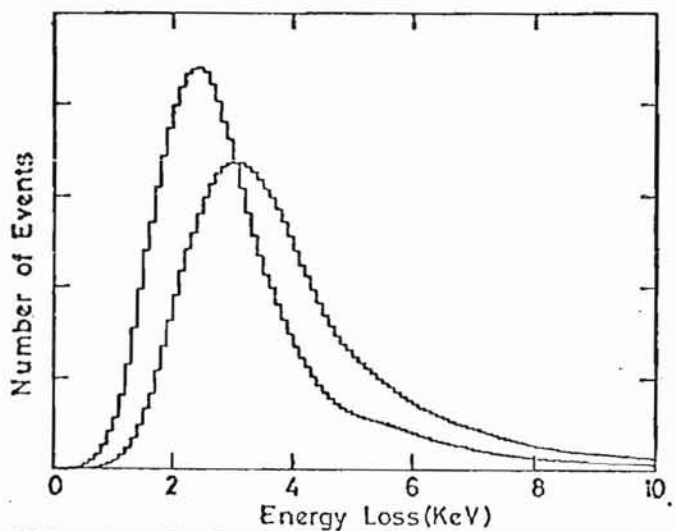

Fig.1.1 Landau Distributions for 25 GeV/c Protons and Electrons

The difference in position and hence the difference in the mean of the two distributions in this figure is the property that can be used to discriminate between charged particles of differing velocity. To explain how this difference arises the following picture from reference (5) is outlined.

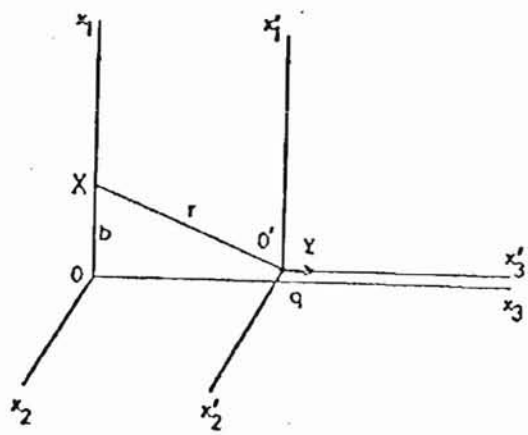

Fig.1.2

Consider a charge q moving with velocity v with respect to another frame

at the point X are given below:

Frame $(x'_1 x'_2 x'_3)$	Frame $(x_1 x_2 x_3)$
$E'_1 = \frac{q\,b}{r'^3} = \frac{q\,b}{(b^2+\gamma^2 v^2 t^2)^{\frac{3}{2}}}$	$E_1 = \gamma E'_1 = \frac{\gamma q\, b}{(b^2+\gamma^2 v^2 t^2)^{\frac{3}{2}}}$
$E'_2 = 0$	$E_2 = 0$
$E'_3 = -\frac{qvt'}{r'^3} = -\frac{q\,\gamma v\, t}{(b^2+\gamma^2 v^2 t^2)^{\frac{3}{2}}}$	$E_3 = E'_3 = -\frac{q\,\gamma v\, t}{(b^2+\gamma^2 v^2 t^2)^{\frac{3}{2}}}$
$B'_1 = 0$	$B_1 = 0$
$B'_2 = 0$	$B_2 = \gamma\beta E'_1 = \beta E_1$
$B'_3 = 0$	$B_3 = 0$

where $\gamma = (1-\beta^2)^{\frac{1}{2}}$; $\beta = v/c$.

Thus at high speeds, when $\gamma \gg 1$, the peak transverse electric field, E_1, of a charged particle as seen by a stationary observer, becomes equal to γ times its non-relativistic value (i.e. the transverse field lines become denser with increasing velocity). Also the duration of appreciable field strengths at the observer is decreased. A measure of the time interval over which the fields are appreciable is given by $\Delta t \sim \frac{b}{\gamma v}$, see Fig.1.3. This time is the typical collision time of the incident charged particle with an electron in the medium being ionized. When this collision time becomes greater than the orbital period of the electron round its atom, the electron will be able to make many cycles of motion as the incident particle passes slowly by. Thus it will only be influenced adiabatically by the fields with no net transfer of energy. So, as a charged particle becomes more relativistic, the shape of its electromagnetic field changes in such a way as to make the collision time smaller at

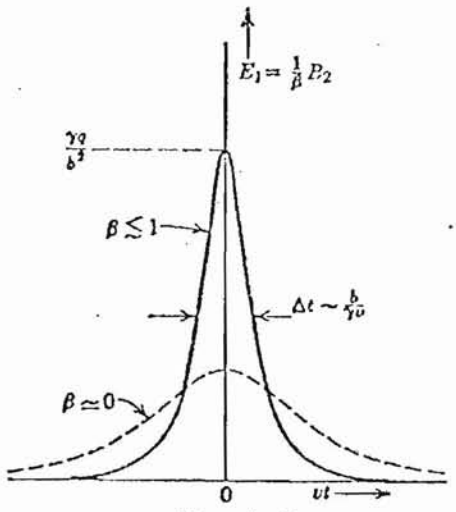

Fig.1.3

larger distances which in turn makes energy transfer more effective at larger distances.

In actual fact, as the incident particle velocity gets faster and faster, the amount of energy transfer to the medium does at first get larger, but at some point it levels off to a constant value. This is due to a screening effect of the atom undergoing collision by the polarization effects of the other atoms of the medium. It occurs when the field of the charged particle has expanded such that the distance for which energy transfer is possible has become comparable with atomic spacing in the medium. This is known as the density effect.

Figure 1.4 shows schematically a plot of how the mean ionization loss varies with γ ($\gamma = (1-\frac{v^2}{c^2})^{-\frac{1}{2}}$. NB. $p/m_o c = \beta\gamma$ and $\beta \sim 1$ for $\gamma \geq 5$.) It shows the relativistic rise from $\gamma \approx 5$ to 500 and the saturation that follows due to the density effect. The region below $\gamma = 5$ has not been discussed since it is of little concern in this thesis. This region is adequately described by semi-classical arguments starting from the Rutherford scattering formula[6]. The fall of ionization with velocity in this region is a kinematic consequence.

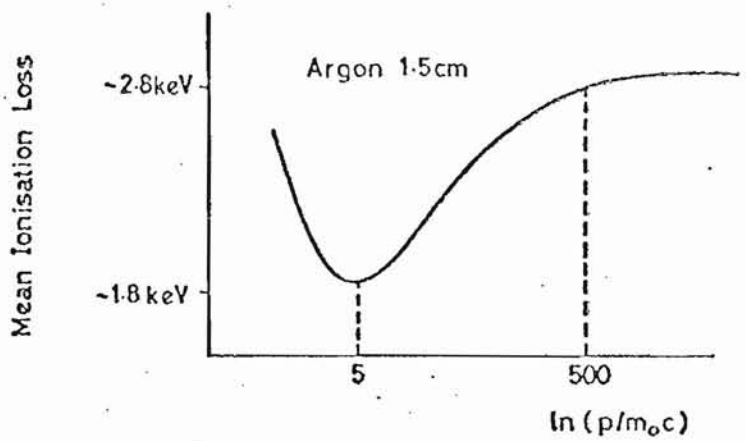

Fig.1.4 Diagram showing main features of relativistic rise curve.

The expression for the mean energy loss as a function of charged particle velocity is given by the Bethe-Bloch formula[7]:

$$\frac{dE}{dx} = 4\pi N Z \frac{z^2 e^4}{m_e v^2} \left[\ln \left\{ \frac{2\gamma^2 m v^2}{h\langle\omega\rangle} \right\} - \frac{v^2}{c^2} - \delta \right]$$

Rate of Energy loss per cm, of particle

Total area covered by electrons in medium $= NZ\pi r_e^2 = NZ\pi\left(\frac{e^2}{m_e c^2}\right)^2$

Relativistic Rise

Density Effect

where N = density of atoms, Z = atomic number, m_e = electron mass, ze = charge of incident particle. δ is a term to allow for the density effect, not included in the original Bethe-Bloch formula.

The logarithmic dependence of energy loss on γ^2 can be seen. One of these factors is due to the relativistic expansion of the electromagnetic field as previously described. The other is due to the kinematic consequence that the maximum energy that can be transferred in a collision increases with γ.

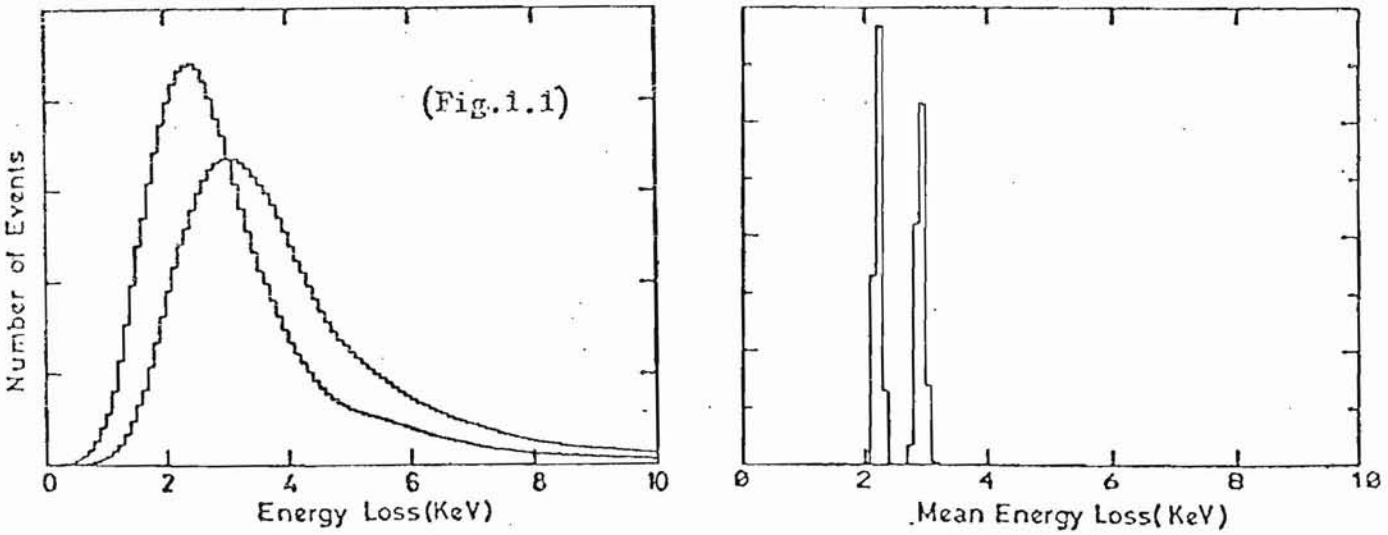

25 GeV/c Protons and Electrons

Fig.1.5

Returning to Fig.1.1 it can be seen that the difference between the Landau distributions for particles having very different γ's ($\sim$ 25 for protons and 50,000 for electrons) is very small compared with the width of the Landau distribution. This means that to discriminate between particles

of different Y with any degree of certainty, repeated measurements of ionization loss for each particle must be made. Fig.1.5 shows how the resolution is greatly improved ~~reduced enormously~~ if the distribution of the mean of 300 measurements for each particle is plotted instead of the Landau distribution. The theory of the Landau distribution is described in more detail in Chapter V.

I.3 HOW CAN IONIZATION LOSS BE MEASURED ?

In the experiments described in this thesis the ionization loss of a charged particle, as it passes through a sample of gas, is measured by using a Multiwire proportional Counter (MWPC) of some form. See Fig.1.6 for side view. A proportional counter produces an electrical signal whose size is proportional to the total energy of the electrons freed in the collision processes. The processes involved in the production of this proportional signal are as follows. The incident charged particle causes ionization of the gas atoms close to its track. This is called 'primary' ionization. Some of the electrons produced in this primary ionization will have enough energy to have further collisions with atoms, causing 'secondary' ionization. The electrons drift down an electric field towards a thin signal wire. In the process they will gain energy from the electric field and lose it by inelastic collisions with gas molecules. The ease with which they will lose energy to the molecules depends upon the possible excited states of the molecule in question. For a noble gas (e.g. Argon), with a closed shell, there are no low lying states and so electrons drifting in Argon will gain a lot of energy which will make them diffuse rapidly. With polyatomic

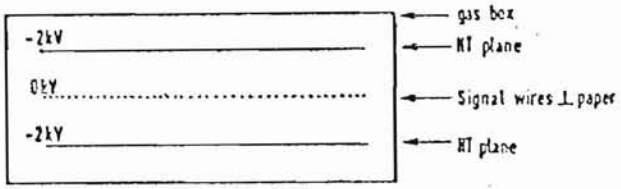

Fig.1.6 A simple layout of multiwire proportional chamber

molecules (e.g. CO_2) there are many low lying levels (e.g. vibrational and rotational) for the electron to excite even when travelling at thermal velocities. Thus, in this case, electrons will not gain a lot of energy and so will not diffuse much[8]. As the electron cloud drifts close to the signal wire, the field intensity increases till, at some point, the electrons acquire enough energy to cause further ionization of the gas. Conditions are controlled in this amplification process such that the total number of electrons arriving at a wire (hence the size of the signal) is proportional to the energy of the primary electrons. (Signal wires are typically 25 μ in diameter and the potential differences between HT planes and signal wires are typically - 2.0 kV when spaced 2 cm from each other.) The characteristic shape of electrical signal (i.e. long tail) is explained when consideration is given to the motion of the positive ions (see reference (9)).

Multiwire proportional counters contain many signal wires and come in many shapes and sizes. For specific examples of MWPC's see Chapters III, IV, V, and for details of the principles and problems of operation, see reference (10). For other experiments where proportional counters are used to measure ionization loss see references (11-15).

CHAPTER II

THE SLAC EXPERIMENT

II.1 INTRODUCTION

An experiment was performed at the Stanford Linear Accelerator in July 1972, by a collaboration of groups from the Universities of Hawaii, Maryland, and Oxford (present author not involved) to observe the properties of the radiation produced by a fast moving charged particle when it crosses a dielectric interface, otherwise known as Transition Radiation. The experiment was supposed to measure transition radiation over a very wide range of parameters, e.g. several different charged particle velocities, radiator thicknesses and spacings, detector gases. As well as measuring the average number of photons produced per charged particle it was supposed to measure the transition radiation spectrum (i.e. a spectrum which was not convoluted with an ionization loss spectrum as obtained by previous results[1]). A considerable amount of time has been spent trying to analyse this very ambitious experiment by the author and T. Katsura (University of Hawaii, working independently). Katsura has up to now, to the authors knowledge, obtained results[16] which are in severe disagreement both with results of other experiments and of theory. The present author has been unable to obtain a calibration of the data that is self consistent to better than 15%, in terms of linearity of the scale and in terms of the absolute position of the TR spectrum[17]. It has been concluded that there is not enough information available to improve the calibration, and so these transition radiation results will not be described here since any conclusions would be highly unreliable.

However, as a by product of this experiment, a large amount of information was obtained on ionization loss. Because of the poor calibration it is only possible to obtain useful information in a very restricted

sense. It is still considered worthwhile to discuss the ionization data here since it gives an independent check to the theoretical predictions of ionization loss in thin gas samples, as described in Chapter V. The part of the experiment relevant to ionization loss and its analysis will thus be described very briefly.

II.2 THE EXPERIMENTAL ARRANGEMENT

A beam from the linear accelerator, containing electrons and pions of defined momentum, was passed through an array of transition radiator foils as shown in Fig.2.1. From the foils the transition X-rays and

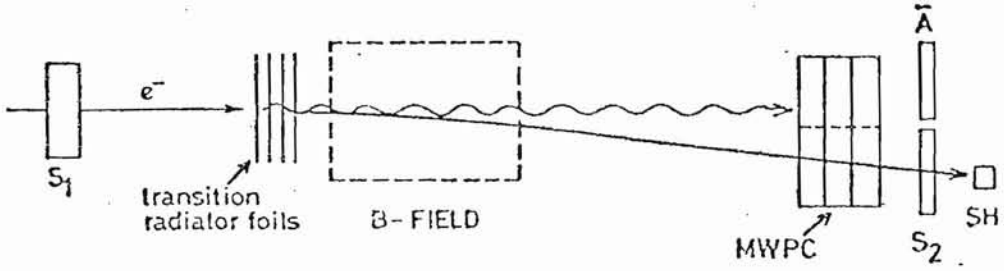

Fig.2.1 Schematic diagram of experiment

charged particles of the beam passed through a Helium bag containing 40 permanent magnets, placed along the beam path, over a distance of 20 metres. Thus the beam of charged particles was slowly deflected a small distance ($\sim$ 6 cm in 100 ft.) away from the transition radiation, which continued to travel in a tight cone about the forward direction. The two beams, i.e. X-rays and charged particles, then travelled through the two halves respectively of each of eight closely spaced multiwire proportional counters (MWPC) along with various scintillation trigger and veto counters. The identity of each charged particle was determined using a shower counter placed behind the MWPC's.

The particle momenta used were 3,9,15 GeV/c for electrons and 9 GeV/c for pions. The MWPC's were sealed and contained Xenon at one atmosphere. They each contained a central plane of signal wires (stainless steel - diameter 20 μ - separation 2 mm - active area 25 × 25 cm^2).

These wires were at earth potential. One half of these wires were connected together and the signal fed to an amplifier. The other half were connected together and fed to a different amplifier. Thus two independent signals were obtained corresponding to the transition X-rays (TR or A side) and charged particle beam (DEDX or B side) respectively. At a distance of 4mm either side of the signal wire plane were placed the cathode planes (Cu wires - diameter 100 μ - spacing 2 mm - wires at right angles to signal wires) at a voltage of - 2.3kV. 3.5mm further from each cathode plane came the chamber windows made of aluminized mylar. These were kept at a potential of - 2.4kV (see Fig.2.2). (For further details of MWPC's used see reference (18).)

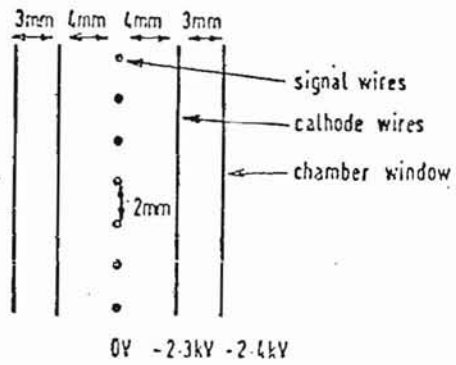

Fig.2.2 MWPC side view

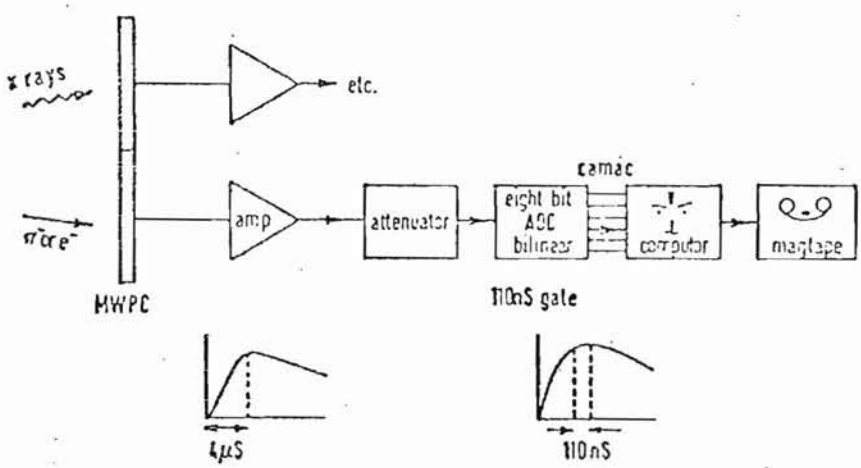

Fig.2.3 Read out system

The Read-out system is shown schematically in Fig.2.3. The attenuators were for equalizing the gain on all 16 channels (= 8 × TR sides + 8 × DEDX sides). The amplifiers had a slow rise time (~ 4 μs). The output pulse had an approximately flat top and was integrated at its peak for 110 ns. The ADC's contained eight bit registers (i.e. 256 channels),

the gain on the first 128 channels being 4 times the gain on the last 128 channels.

For the DEDX side, two out of the eight MWPC's were not used for measuring ionization since their associated electronics was used for other purposes.

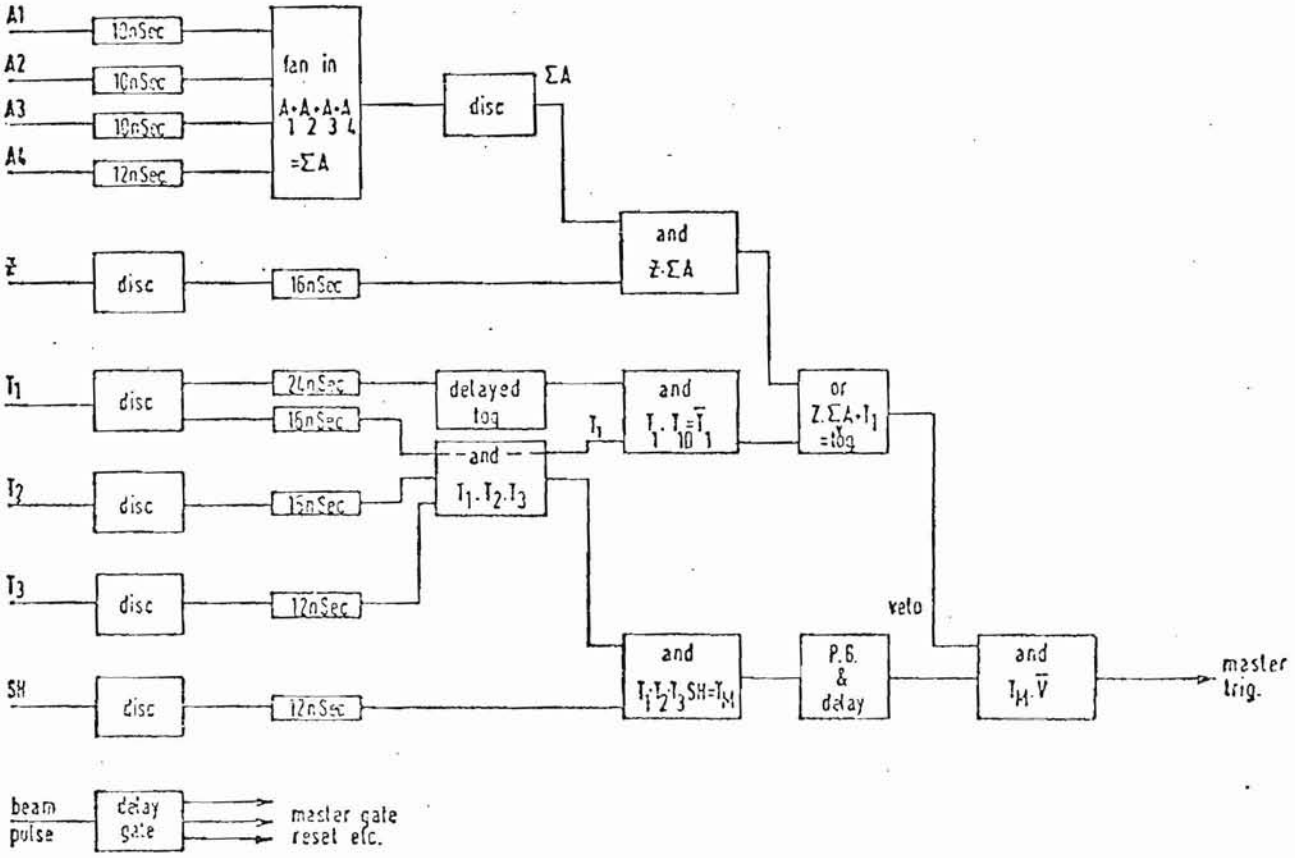

Fig.2.4 Logic for SLAC experiment

Figure 2.4 shows the logic used in the SLAC experiment. Referring to this figure and Fig.2.5, it worked as follows. The beam was defined by counters T_1, T_2, T_3 in coincidence. The shower counter, SH, was sometimes in the trigger to select e's or π's, or otherwise its pulse height was recorded and used later to separate π's and e's. The master trigger to initiate read-out was delayed by 1.7 μs and could be vetoed by (a) a second (or previous) count in T_1 within the same beam pulse, (b) a count in one of A_1, A_2, A_3, A_4 (situated around T_1) in coincidence with Z (i.e. to eliminate background coming in nearly the beam direction).

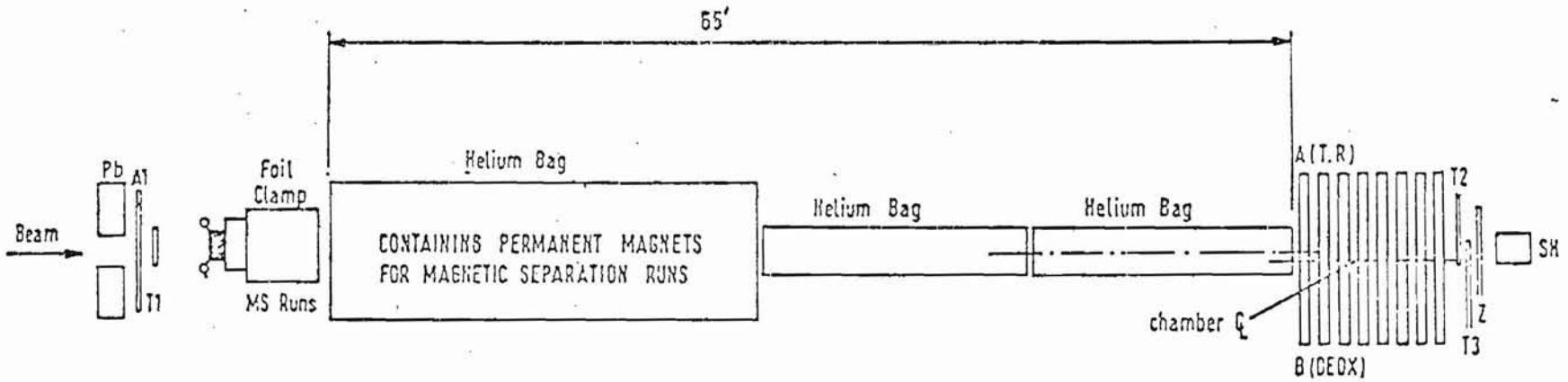

Fig. 2.5 Experimental Layout

11.3 CALIBRATION OF SLAC EXPERIMENT

The calibration is divided into two parts, (i) the time independent part which includes measurements of nonlinearity of electronics, etc., and (ii) the time dependent part which includes variations with time of the gas gain of the MWPC's due to variations of gas density and composition, etc. This calibration procedure is very similar to the one that will be described in detail for the NAL experiment. It will thus only be described here just enough to explain the problems encountered with this calibration.

(i) The nonlinearity of the electronic amplifier and ADC response is corrected for, by feeding in test pulses of known size at the signal wires of the MWPC's and observing the output of the ADC's. An approximately

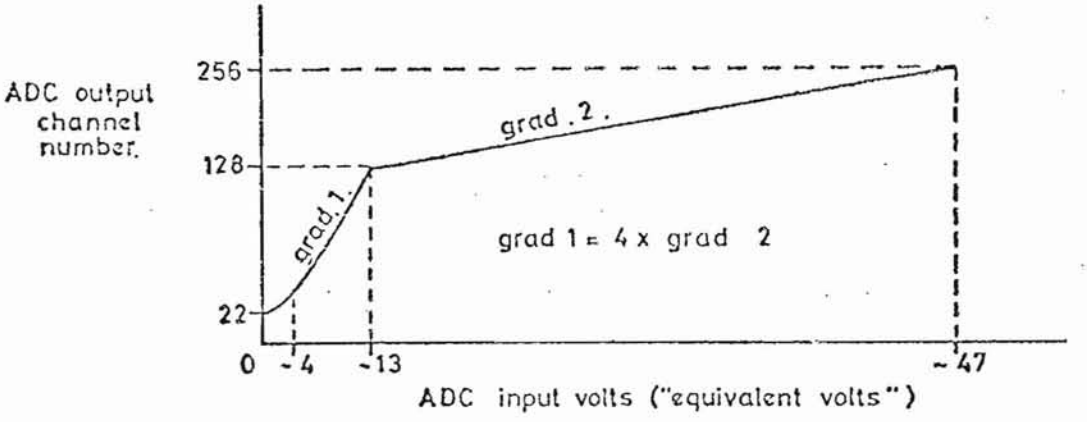

Fig. 2.6

bilinear curve for each of the 16 channels was obtained of the form shown in Fig.2.6. (This is only a schematic diagram. The magnitudes of input test pulses are given in arbitrary 'equivalent volts' units.) As can be seen there is a deviation from linearity as the pedestal (i.e. zero input volts) is reached. This calibration was performed at the start of the experiment, and assumed to remain constant throughout. However, there is data to show that the pedestal fluctuates typically by ±5% between runs, (45 runs in all). This can be corrected for if the shape of Fig.2.6 is assumed to be constant. Also, during the experiment, the power supply

for the ADC's was replaced (due to a fire in the CAMAC crate!) This caused a change in the pedestals of typically ~ 25%.

(ii) The variation of chamber gain with time for the DEDX sides was measured by placing an Fe^{55} 5.9 keV X-ray source in front of each of the MWPC's at approximately 5 hour intervals. (The whole 45 runs took 50 hrs.) The X-ray spectra so obtained were corrected for nonlinearity as explained above and were fitted with a gaussian using a least square minimizing program, and hence their peaks were obtained. A typical spectrum is shown in

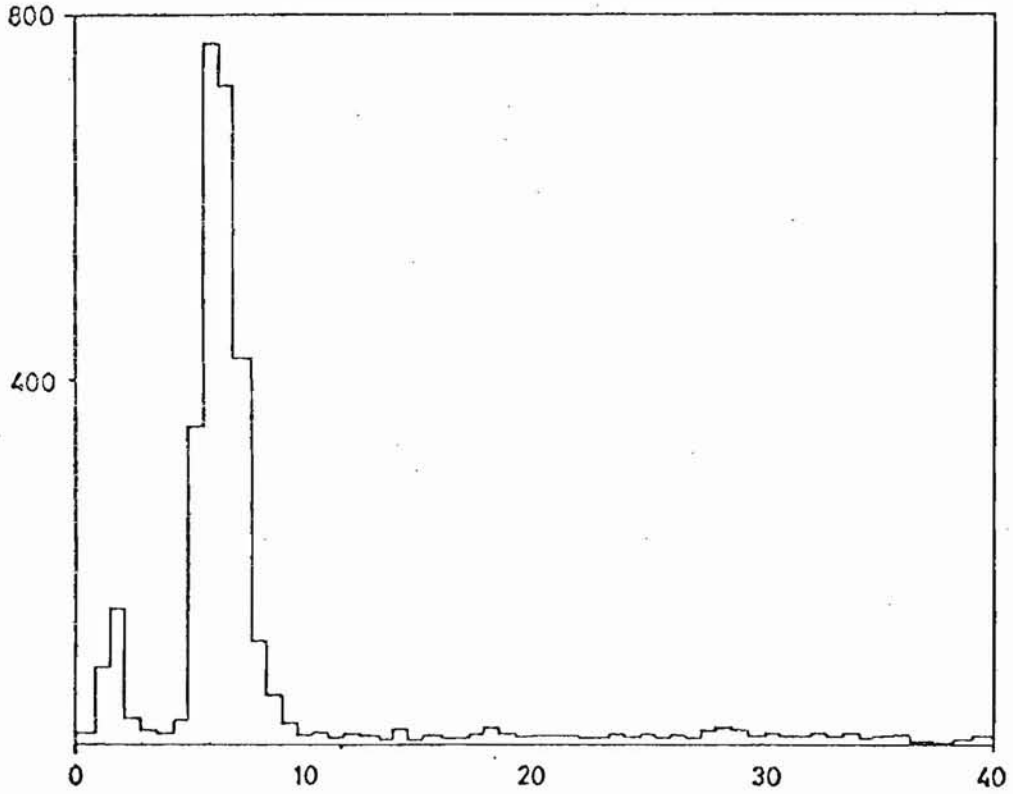

Typical Fe^{55} Calibration Peak

Fig. 2.7

Fig.2.7. As can be seen the useful information is contained within about 10 bins of this histogram. This means that the confidence level of a fit with 4 free parameters (as used) is very low even though it may look very good. In effect the fit gives the peak quite accurately, but its method of calculating the error on this peak will not work. Thus it is better to estimate an error. It is estimated that the peak could be determined

to $\pm\frac{1}{2}$ bin width which implies an error of $\pm 3\%$ in the conversion factor of equivalent volts to electron volts. The variation of this conversion factor, f, with time and chamber is shown in Table 2.1. It can be seen that the conversion factor is consistently larger for the first chamber, DEDX0.

TABLE 2.1

Conversion Factor, f, (equivalent volts/keV) for DEDX Sides of MWPC's

Run No.	DEDX0	DEDX1	DEDX2	DEDX3	DEDX4	DEDX5	DEDX6	DEDX7
95	1.06	0.94	0.92		0.98		0.94	
111	1.11		0.95		0.98		0.91	
119	1.06	0.97	0.97	0.89	0.98		1.01	
125	1.07	0.96	0.95	0.88	0.95		1.00	
129	1.11	1.02	0.99	0.93	1.06		1.11	

It should be mentioned that for the TR sides of the MWPC's, three different calibration X-rays (5.9 keV, 22 keV, 38 keV) were used. It was found that at 38 keV the MWPC's were not proportional to better than 10%.

There is one further problem in this calibration which will only be mentioned here. When data-taking, an X-ray passes through one half of a MWPC simultaneously with a charged particle passing through the other half. Capacitative cross talk effects exist such that a signal in one half of an MWPC induces a signal in the other half of magnitude equal to $-0.157 \times$ its own magnitude.

II.4 PARTIAL ANALYSIS OF SLAC DATA

With the calibration as outlined above, it is found that the overlap between supposedly identical spectra from different chambers is not very good. The positions of the peaks of ionization distributions differ by as much as 9% from chamber to chamber. The calibrated distributions for the first chamber, DEDX0, are almost always lower than for the other chambers for all particles and velocities. It is thought unlikely that this is a real physical effect (e.g. possible bremsstrahlung effects at exit windows of first chamber !) and much more likely to be a calibration problem (e.g. possible non-uniformity of gain across DEDX0, since it is highly unlikely that the X-ray source was placed in exactly the position of the beam).

With these problems in mind the amount of useful information is somewhat limited and thus only the following small subset of the data is shown. Using the results of only one chamber, Figs.2.8 and 2.9 show the Landau ionization distributions of 9 GeV/c e's and π's from data collected simultaneously in one run. The relative position of the two distributions is probably thus fairly reliable. Also shown in these two figures are the theoretical distributions for 1.5 cm Xenon calculated by Monte-Carlo methods as outlined in Chapter V *. The agreement is surprisingly good with respect to the position of the peaks of the Landaus, considering the accuracy of the calibration. The shape is not so surprising since very large calibration errors would be needed to have an effect on a distribution that is ~100% wide. Figs.2.10 and 2.11 show similar distributions for 3 GeV/c and 15 GeV/c electrons respectively. (The pion statistics for these energies are too low in these runs to obtain any useful information.)

---

* The theoretical distributions contain a resolution function with $\sigma = 5\%$. This is made up of electronic noise and statistical fluctuations in the gas amplification process. It has negligible effect on these broad spectra.

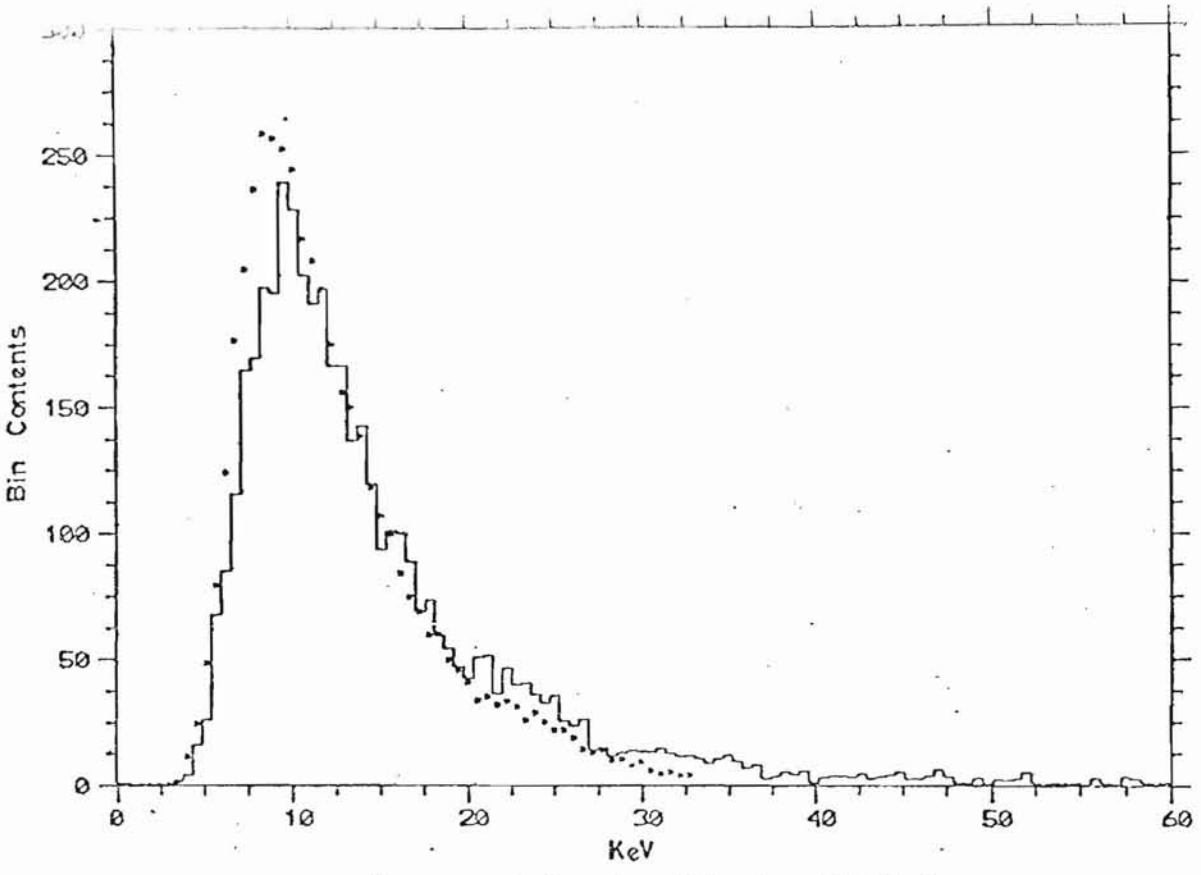

Theory and Experiment Landau Distributions
9 GeV/c e^- through 1·5 cm Xenon.

Fig. 2.8

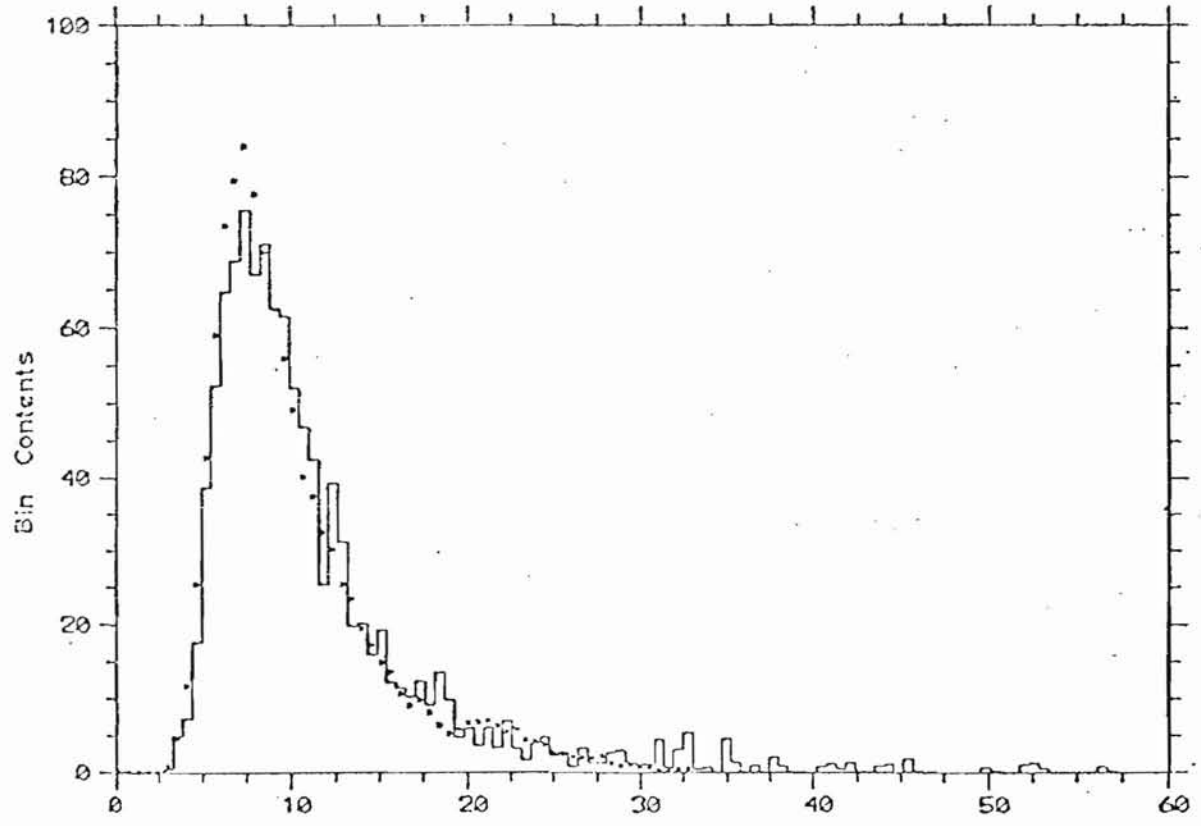

Theory and Experiment Landau Distributions
9 GeV/c π through 1·5cm Xenon.

Fig. 2.9

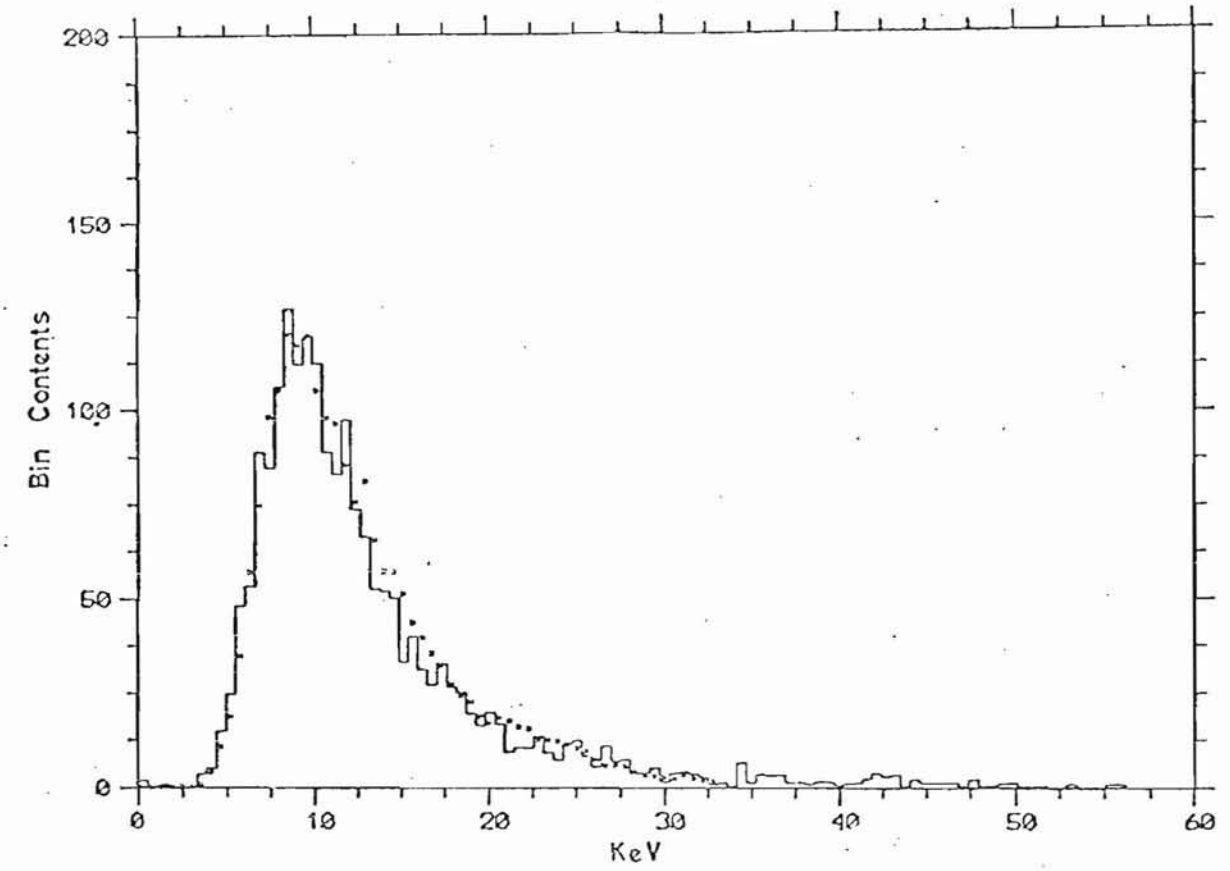

Theory and Experiment Landau Distribution
3 GeV/c e^- through 1.5 cm Xenon.

Fig. 2.10

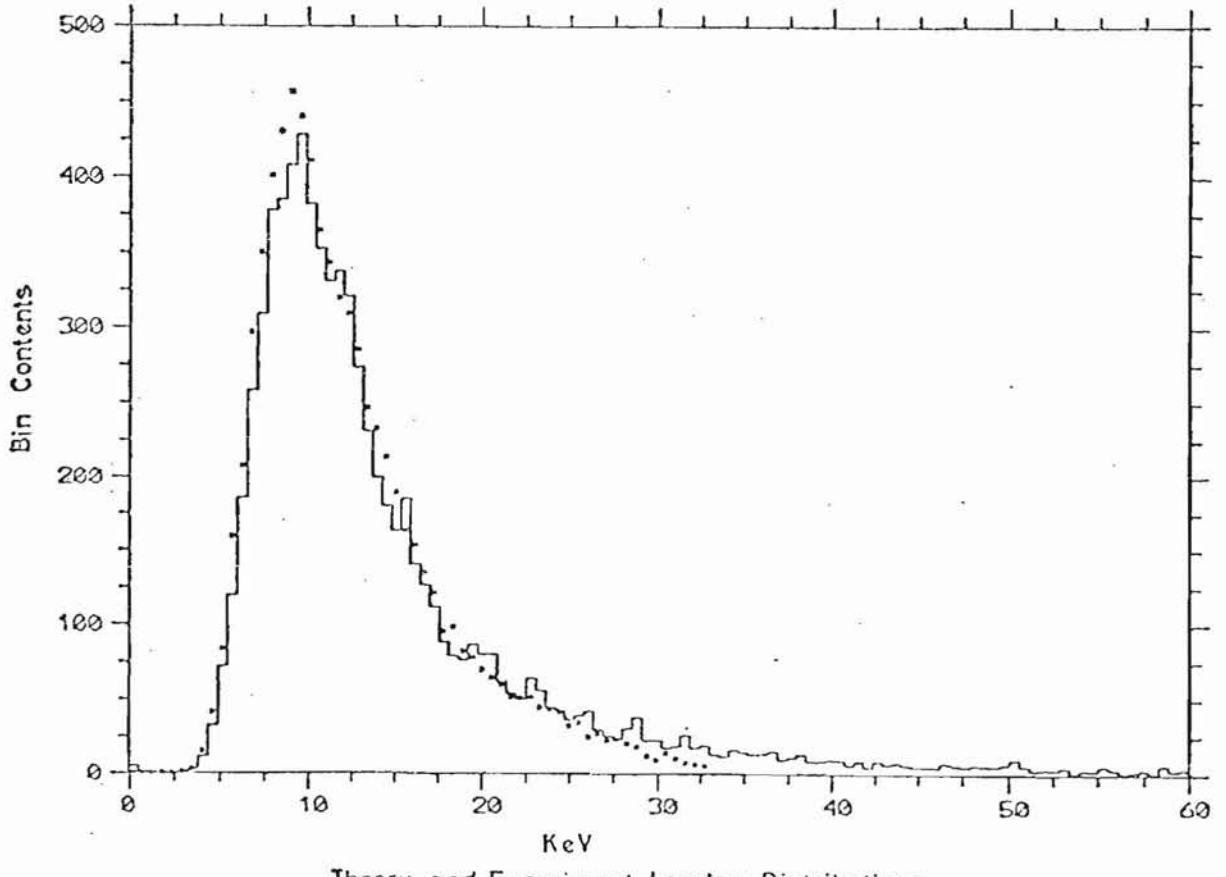

Theory and Experiment Landau Distributions
15 GeV/c e^- through 1.5 cm Xenon.

Fig. 2.11

II.5 CONCLUSIONS FROM S L A C EXPERIMENT

The Landau distributions for 3 , 9 , 15 GeV/c electrons and 9 GeV/c pions have been shown to be in good agreement with theory.

This is the only useful direct piece of quantitative information obtained from this experiment by this author. The experiment seems to have suffered from trying to do too much in too short a time and the analysis hindered by the author not having helped in the running of the experiment, so not being quite sure exactly what was done.

CHAPTER III

THE RHEL EXPERIMENT

III.1 INTRODUCTION

An experiment was performed by the Oxford I S I S Group at the Rutherford High Energy Laboratory (R H E L) in December 1973, using the P 71 test beam line from NIMROD. The measurements made, that will be described in this chapter, are of the ionization loss produced when charged particles at various velocities pass through a thin sample of 90% Ar/10% CH_4. These are used to plot a 'relativistic rise' curve of the most probable ionization loss against incident charged particle velocity. This curve is then compared with that generated theoretically by Monte-Carlo calculation as described in Chapter V.

These measurements formed a small part of a much bigger test experiment[19]. They were made in a very restricted time interval during which it was possible to make only a fairly crude attempt at data collection. For this reason the experiment and the analysis are not presented in any great detail.

III.2 APPARATUS AND METHOD

The ionization detector was a multiwire proportional counter (MWPC). It consisted of a plane, 25 cm square, of signal (anode) wires of diameter 20 μ spaced at 2 mm intervals. This plane was sandwiched between two planes of high voltage (cathode) wires, diameter 100 μ, also spaced at 2 mm intervals. The distance of the signal wire plane from each of the high voltage planes was 0.4 cm. The high voltage wires were at right angles to the signal wires. This sandwich of wire planes was contained in a gas-tight box containing 90% Ar/10% CH_4. The high voltage wires were all connected together to a power supply at ~ -1800 volts. As can be seen, the chamber was similar to the type used in the S L A C experiment, i.e. see

Fig.2.2, p.12, the only difference being that the voltages used in the two experiments were different.

The method of data collection is shown in Fig.3.1. Particles of defined momentum and type (0.5 - 2.0 GeV/c π, p, or e) enter the MWPC causing ionization of the gas. This ionization is amplified and detected by the signal wires which are all connected together to a common amplifier. The output of this amplifier is fed into an ADC, the ADC being gated for a fixed time about this output pulse. The ADC gate was self-triggered for the calibration X-ray signals and triggered by beam defining scintillation counters for real particles. The ADC outputs were read via CAMAC by a PDP8 computer.

Particles were identified using time of flight (to distinguish protons from pions and electrons), a gas Cerenkov counter (to detect pions and electrons), and a shower counter (to detect electrons).

For each event, the computer allowed the ADC output to enter the appropriate histogram plot if it received the correct preselected combination of signals from the particle identifying counters mentioned above, and if the magnitude of the ADC output was large enough. (The presence of a software discriminator will be seen at low energies in the spectra that follow). Histograms of the dE/dx loss (in arbitrary ADC channel number units) for the particles, $e^{\pm}$, $\pi^{\pm}$ and p were obtained and written onto magtape. The histogram for the escape peak in Argon of the 5.9 keV X-rays of Fe^{55} was also recorded at various times throughout the experiment for calibration of the chamber (i.e. conversion of ADC channel number units to energy units).

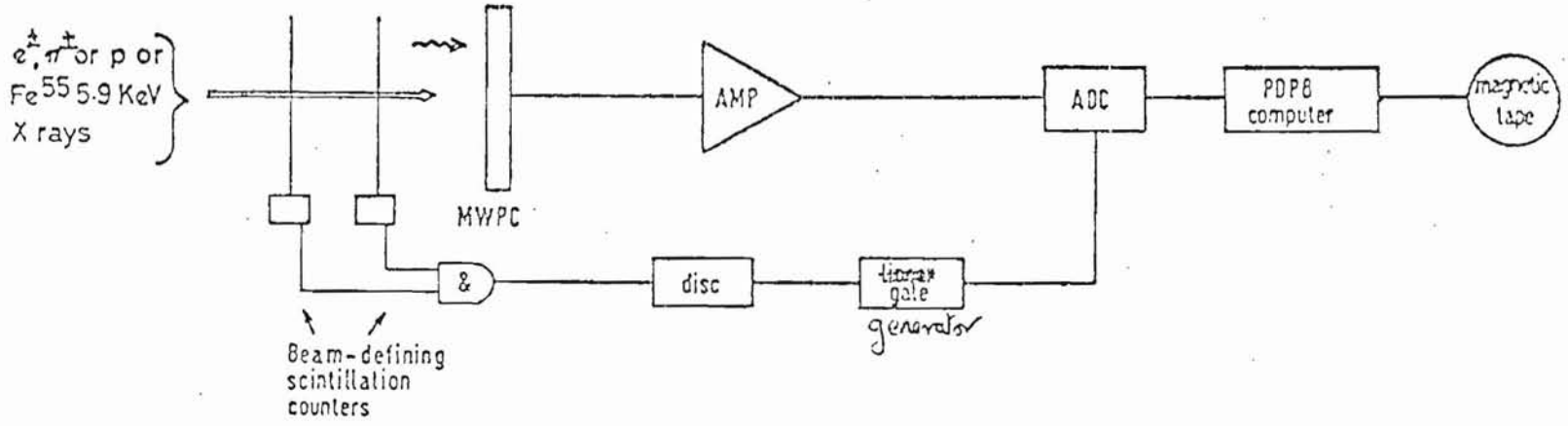
$e^{\pm}, \pi^{\pm}$ or p or
Fe^{55} 5.9 KeV
X rays
MWPC
AMP
ADC
PDP8
computer
magnetic
tape
&
disc
gate
generator
Beam-defining
scintillation
counters

Fig. 3.1

III-3 DISCUSSION AND TREATMENT OF DATA

Figures 3.2 and 3.3 show typical Landau distributions obtained for π's and e's from this experiment. On these are superimposed theoretical curves normalized to the experimental number of events and shifted along the x axis till they give the best fit to the data. As can be seen, in the pion case the fit is very poor and for the electron case, statistics are so low that it is difficult to say anything about the fit. It is believed that the theoretical shape is good since it agrees with previous experiments (see Chapter VI). There is not much that can be done to understand these plots better, since no further information is available than that contained in the plots shown. The peak at the low energy end of these distributions is known to be due mainly to electromagnetic pick-up by the detector, of a quadrupole magnet situated about 1 m away from it. This effect was reduced considerably by putting an earthed conducting sheet between this magnet and the chamber. How far under the Landau distribution these low energy 'events' spread is not known.

To obtain a relativistic rise curve from the data, the peaks of the Landau distributions for all particle velocities must be obtained and then calibrated into units of energy from those of ADC channel number. The methods used in these two steps are described in the next two sections.

Having obtained the experimental relativistic rise curve, it is then compared with that obtained theoretically.

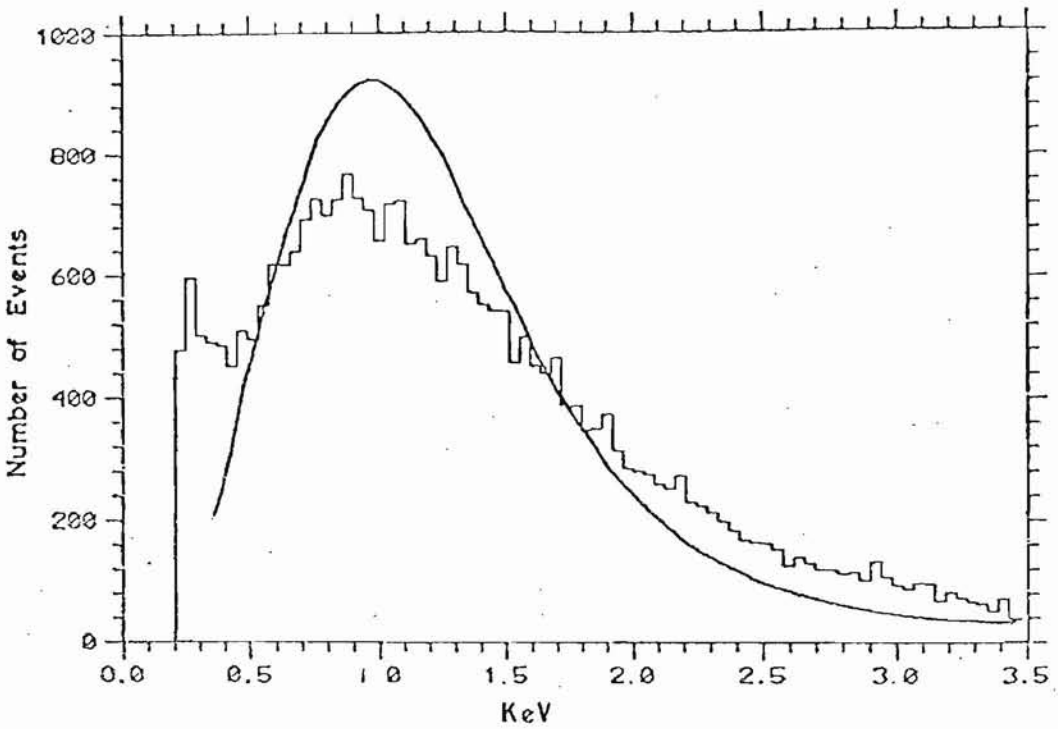

Fig. 3.2 Typical Pion Spectrum

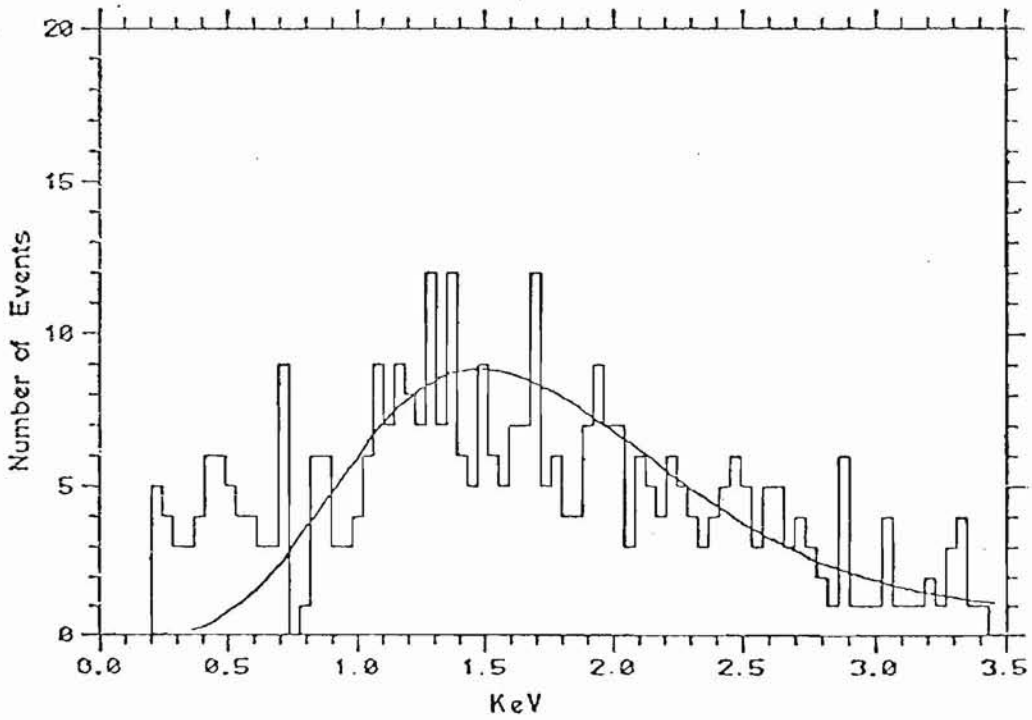

Fig.3.3 Typical Electron Spectrum

III.4 DETERMINATION OF PEAKS OF HISTOGRAMS

The low energy noise peak of the type shown in Fig.3.2, and/or the poor statistics, made the determination of the position of the Landau peak very difficult. For instance a fit of theory to experiment, by minimizing χ^2 is meaningless since the χ^2 is so large. The following procedure was thus adopted[20].

The original histogram, whose peak must be determined, is used to generate four further histograms in the following way. Two empty histogram plots are set up. An event is put into one of these histograms chosen randomly, and this is repeated until the sum of the contents of each two corresponding bins in the two new histograms is equal to the corresponding bin in the old histogram. This procedure is repeated so that a total of four 'random' histograms is obtained. In a particular histogram the bin with the largest contents is taken as the peak of that histogram (the position of the peak within this bin is determined by the relative contents of the two adjacent bins). The five peaks thus obtained from the four 'random' histograms and the original histogram, are averaged and their r m s deviation is taken as the error on the peak. This error is the error due to statistical fluctuations in the histogram. It says nothing about the error in the real peak due to low energy spikes etc. Errors of this kind can only be estimated in a somewhat crude way. The error due to the low energy spike was estimated by extrapolating the high edge of the spike under the Landau distribution, then subtracting it out of the histogram. The resulting change in the position of the peaks is estimated to be of the order 5 to 10% in the region of $p/m_o c$ defined by 1.0 GeV/c protons to 1.5 GeV/c pions. For higher values of $p/m_o c$ where the Landau peak is further from the low energy spike, the position of the peak is estimated to change very little. Very roughly this means that

points near the minimum of the relativistic rise curve (Fig.3.5) would be shifted up in energy by the length of their error bars, leaving points further away approximately the same. This would reduce the size of the relativistic rise seen.

III.5 CALIBRATION OF THE PEAKS OF THE HISTOGRAMS

The X-ray calibration peak used was the Argon escape peak of the 5.89 keV X-rays from an Fe^{55} source. (This occurs when the 5.9 keV X-ray excites an Argon atom with subsequent de-excitation and escape of a 3 keV X-ray.) This peak was measured regularly at various times during each run. The peak was taken to be at 5.89 − 3.0 = 2.89 keV (the Kα lines in Argon are at 2.96 keV and the Kβ line is at 3.19 keV). A typical calibration histogram is shown in Fig.3.4, the peak on the right of the figure being the escape peak. Since the calibration histograms are cut off at high

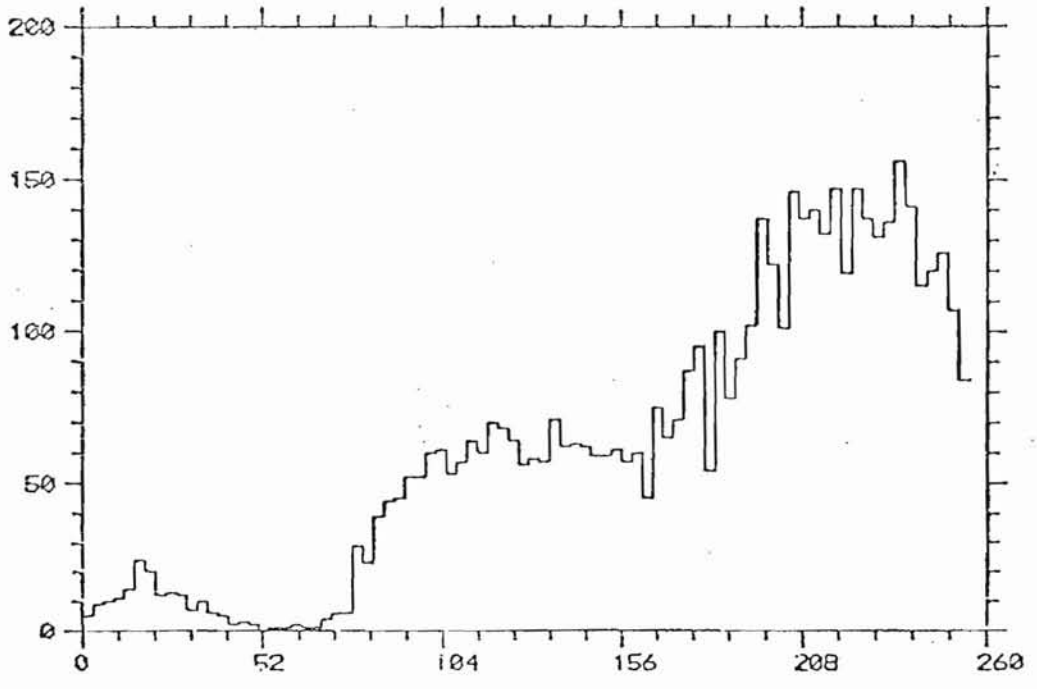

Fig. 3.4 Typical Fe^{55} Calibration Spectrum

energies it is not possible to be certain that the escape peak is completely resolved from the main peak. Incomplete resolution would cause a systematic shift in the direction of making the dE/dx peaks appear lower in energy than they really were. It is thought the absolute normalization of the data could be shifted by as much as 10% due to this effect.

Having determined the calibration peaks and their errors, using the method described for the Landau peaks, it was found that variation between peaks for different calibration runs was of the same order as the error (due to statistical fluctuations) in determining them and since no trends were observed in these fluctuations it was decided to assume a constant calibration peak and to use the mean of all the calibration peaks to calibrate all histograms, and the r m s deviation of this mean as the error in the calibration peak.

III.6 RESULTS AND COMPARISON WITH THEORY

The results of this experiment and the theoretical predictions are given in Fig.3.5 and Table 3.1. There may be an energy normalization problem between theory and experiment due to the effective thickness of the chamber not being known. In the theoretical calculation it was taken as the physical thickness of the gas between high voltage planes, i.e. 8 mm. Also there could be a normalization problem due to the incomplete resolution of the escape peak from the main X-ray peak, as mentioned in the calibration section. In Fig.3.5 the theory has been normalized to the point where $p/m_o c = 0.8$.

On top of these normalization problems the size of the experimental relativistic rise, as shown in Fig.3.5, might be too large by 5%, due to systematic errors in determining the Landau peaks around the minimum. (See previous section on determination of peaks.)

The relativistic rise is found to be 1.8 ± 0.5 (error estimated from errors in Fig.3.5). Theory gives 1.58.

Fig.3.5 Experiment compared with theory(curve) for (dE/dx)mp vs p/mc

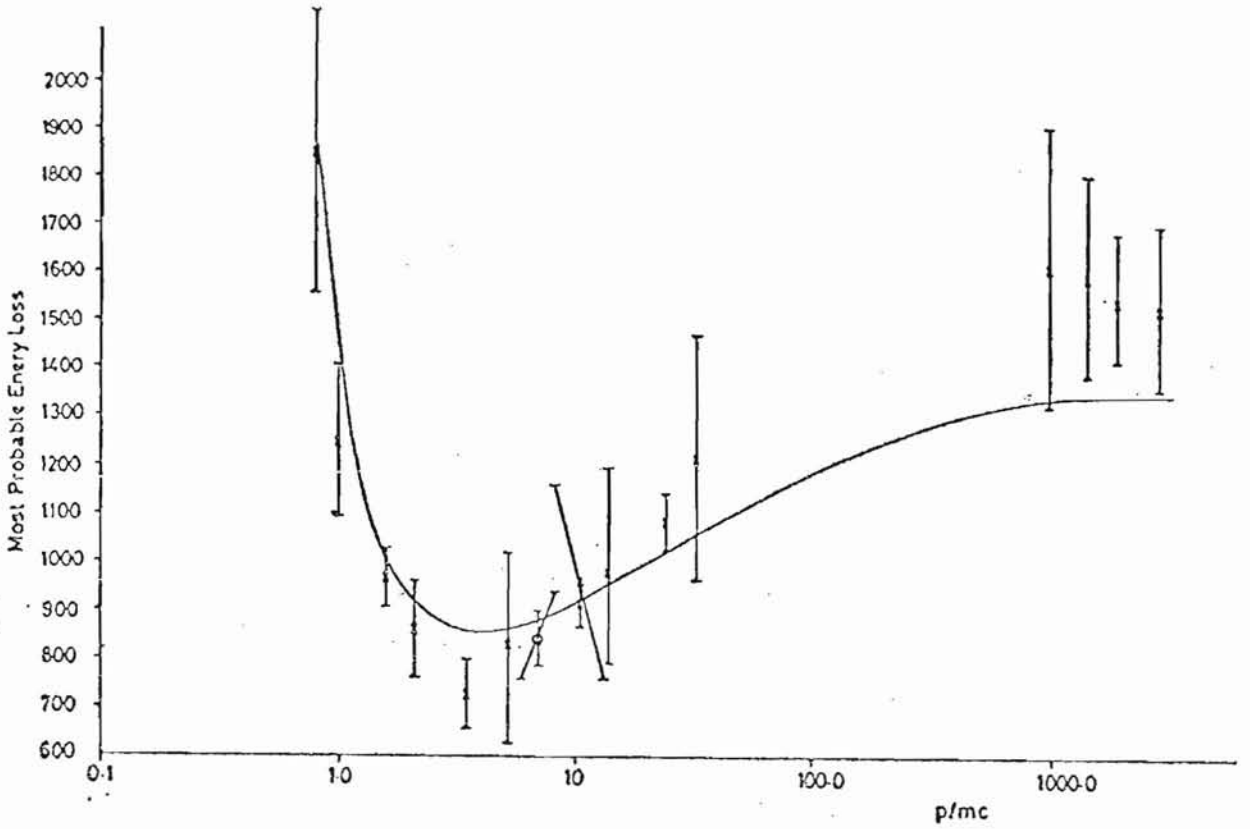

TABLE 3.1

PARTICLE TYPE	MOMENTUM GeV/c	p/mc	EXPERIMENTAL PEAK eV	THEORY PEAK eV
e^-	0.49	953.4	1604.1 ± 291.4	1432
π^-	0.49	3.5	722.8 ± 64.8	910
e^+	0.73	1430.2	1584.2 ± 219.7	1420
π^+	0.73	5.2	829.8 ± 205.1	914
P	0.73	0.8	1848.5 ± 293.8	2003
e^-	0.97	1906.9	1538.5 ± 131.8	1423
π^-	0.97	7.0	842.3 ± 56.2	939
π^+	0.97	7.0	858.2 ± 90.2	939
P	0.97	1.0	1248.9 ± 159.2	1556
e^-	1.46	2860.3	1517.5 ± 172.2	1435
π^-	1.46	10.5	911.7 ± 41.0	973
π^+	1.46	10.5	961.0 ± 208.1	973
P	1.46	1.6	969.1 ± 60.0	1087
π^-	1.95	13.9	985.7 ± 206.1	1018
P	1.95	2.1	862.2 ± 113.3	984
π^-	3.41	24.4	1084.2 ± 48.6	1084
π^-	4.69	33.6	1214.8 ± 253.9	1128

III.7 CONCLUSION

The quality of the data is not good enough to form any very positive conclusions. It is not possible to say that theory is definitely inconsistent with the experimentally determined relativistic rise curve. It is also not possible to predict from these results the upper limit of the range of $p/m_o c$ for which particle discrimination is possible by this technique.

Consequently the conclusion is made that a more accurate experiment is needed.

CHAPTER IV

THE NAL EXPERIMENT

IV.1 INTRODUCTION

This experiment was performed at Fermi National Accelerator Lab. in January 1975 by W.W.M. Allison, C.B. Brooks, J.N. Bunch, R.W. Pleming and P.D. Shield[21]. Its aim was to measure the ionization deposited simultaneously in many samples of gas by charged particles of known type and velocity passing through the gas. From repeated measurements, probability distributions of ionization loss were obtained and also distributions of the mean ionization loss of all samples for each particle traversal of the gas. The amount of overlap between mean distributions for different values of charged particle velocity, gives an indication of the confidence with which one can hope to discriminate between particles. The variation of the most probable mean ionization loss with particle velocity gives the so-called 'relativistic rise' curve. The experiment was also used to investigate correlation effects between the supposedly independent samples of ionization collected simultaneously, and to test the theory of Garybian[22] that the relativistic rise curve as measured, is modified by effects due to detector windows.

The ionization detector used was a purpose built multi-wire proportional chamber with a small drift region. It will become clear that this chamber, in which proportional and drift properties are combined, is an unconventional design. It is built in such a way that it forms a small prototype of a device which will hopefully be able to identify charged particles in the difficult region of 3 - 50 GeV (where other methods fail).

FLOW DIAGRAM OF NAL EXPERIMENT

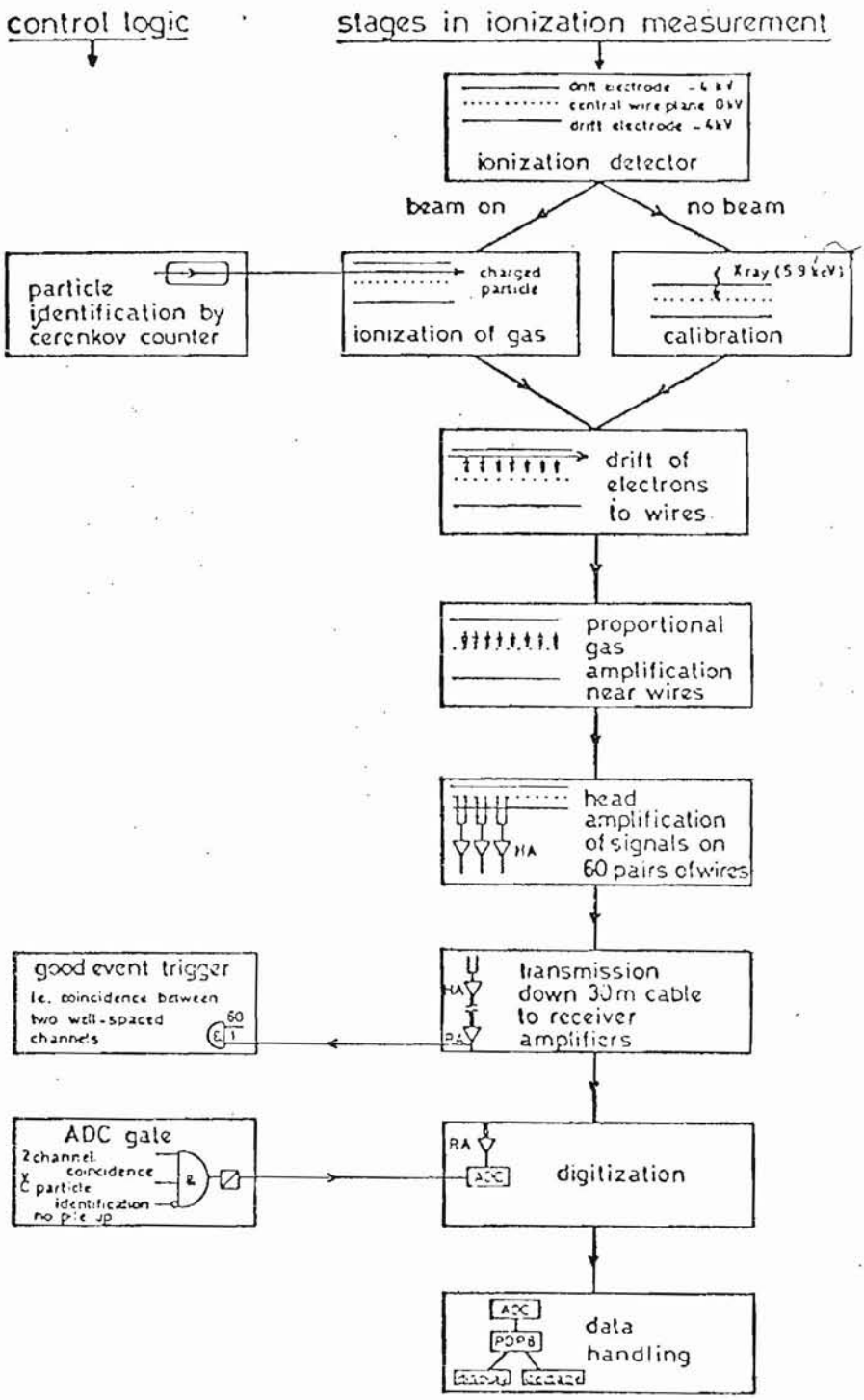

Fig. 4-1

IV.2 THE EXPERIMENTAL ARRANGEMENT

A simple picture of how the detector works and how the experiment was performed is given in the flow diagram, Fig.4.1. A diagram of the experimental arrangement is shown in Fig.4.2.

The particle beam was the N3 hadron beam as used for the 30" bubble chamber at NAL. The ionization detector was placed 200 m upstream of the bubble chamber at a point coinciding with a vertical focus, where the beam size was approximately 1 cm in the vertical direction, and less than 10 cm wide. Particles of defined momentum were passed through the upper drift region of the detector parallel to and ~1 cm away from the wire plane. A Cerenkov counter provided particle identification, and scintillation counters, S1, S2, either side of the Cerenkov counter with S3 behind the ionization detector, provided information on particle pile up. An X-ray source of known energy in a thick metal box was placed above one of the channels of the ionization detector to provide calibration information. The box had a remotely controlled shutter on it, operated by the computer, which was opened between particle beam bursts.

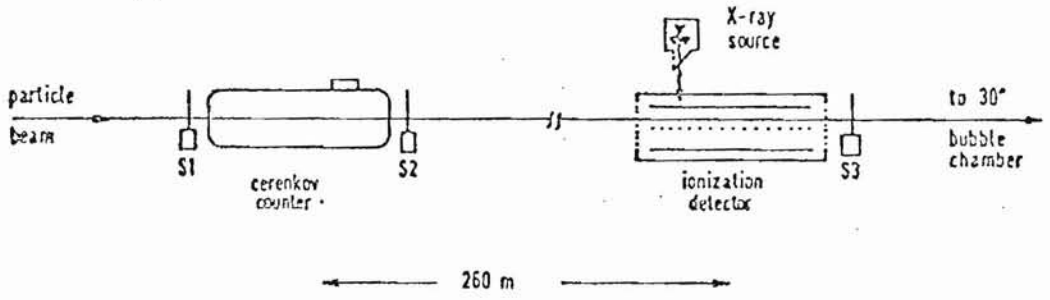

Fig.4.2 Schematic diagram of main elements used for measuring ionization loss.

IV.3 DETAILS OF APPARATUS

IV.3.1 The Ionization Measuring Detector

A diagram of the detector is shown in Fig.4.3.

The central signal wire plane consisted of stainless steel anode wires, length 35 cm, diameter 25 μ, spaced at intervals of 0.75 cm at earth potential. In the same plane and midway between each pair of these signal wires was a 250 μ stainless steel cathode wire. At a distance of 3.5 cm either side of the signal wire plane was a flat metal sheet which acted as a drift electrode.

3.5cm = 1in / 2.54cm × 3.5
= 1.378 in

plane cathode at 1.378 in from anode

ours, .25"

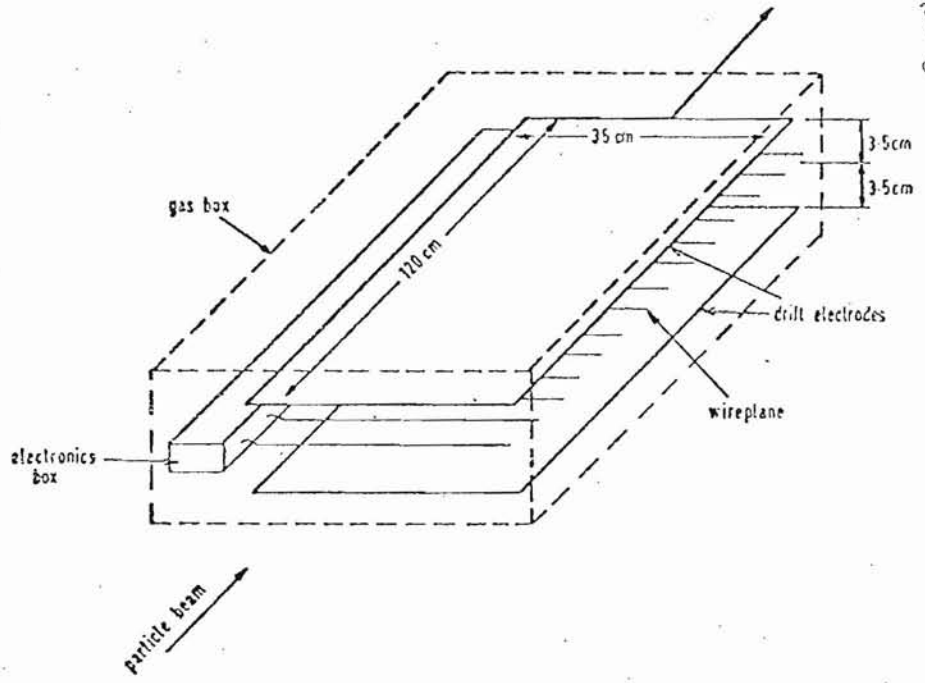

Fig.4.3a) Schematic diagram of NAL chamber

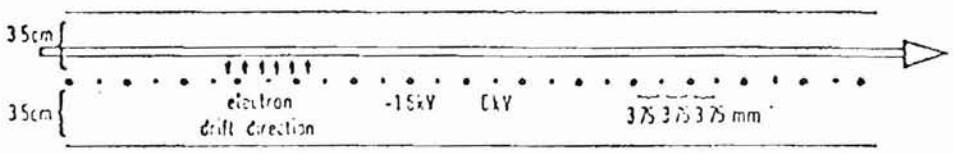

Fig.4.3b) Side view of NAL chamber

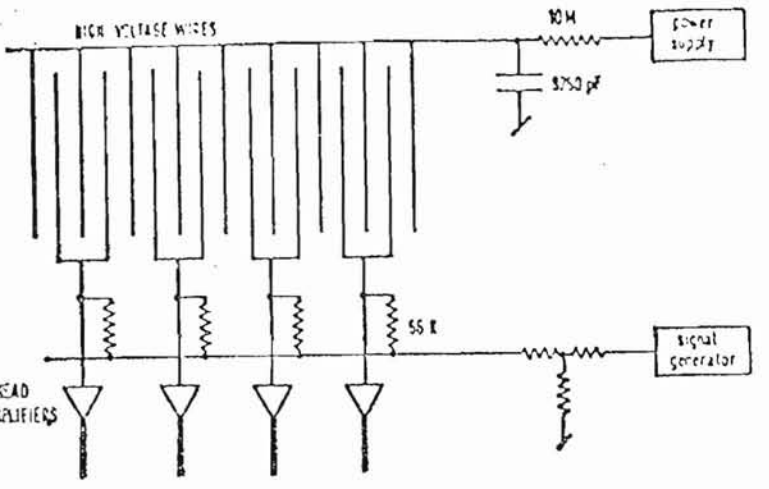

Fig. 4.4a) Electrical connections to signal wire plane

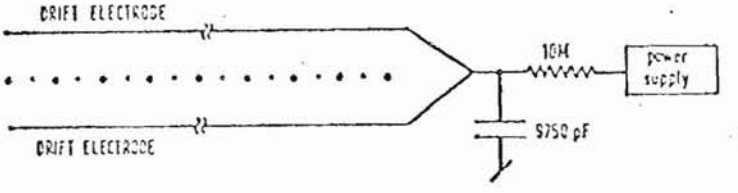

Fig. 4.4b) Electrical connections to drift electrodes

The electrical connections in the chamber to these electrodes are shown in Figs.4.4(a) and (b). Fig.4.4(a) shows pairs of adjacent signal wires sharing a common head amplifier so defining a 1.5 cm sample size. Sixty such samples were created. Each of these channels was also connected to a common signal generator that generated signals of comparable shape to real signals. This was used to monitor and calibrate the electronics. The thicker cathode wires between the signal wires were used to control the amount of gas amplification around a thin signal wire, independently of the drift field, which was determined by the voltage on the two drift electrodes. Fig.4.4(c) shows the electric field lines in the detector for typical operating conditions[23]. As can be seen, all the drift field lines end up on the signal wires. This condition is obtained with this geometry when V(signal-cathode) $\geq$ V(signal-drift)/3.55 [24], and it ensures that all the electrons from ionization processes go to the signal wires.

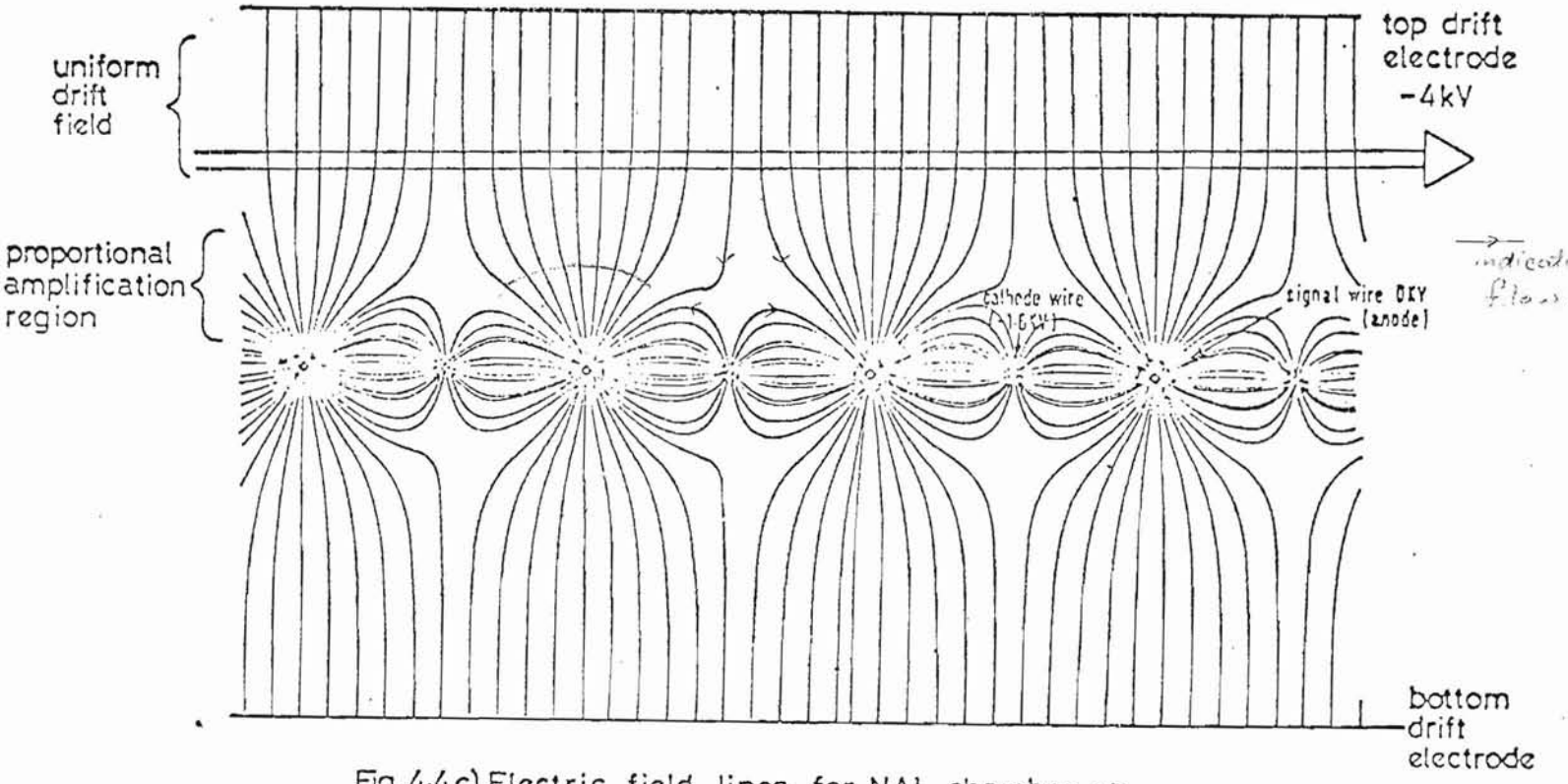

Fig. 4.4c) Electric field lines for NAL chamber as generated by a computor program for solving Laplace's equation iteratively. (The field lines are not drawn very close to the wires.)

The active region of the detector from which data was obtained was defined as being 10 cm away from any edge of the signal wire plane. It contained 120 signal wires and 120 cathode wires. Thus the size of this active region was 90 cm (span covered by signal wires coupled to electronics) × 10 cm (horizontal beam size).

The electrode assembly and head amplifiers were contained in a gas box as shown in Fig.4.5. The gas box was all metal (Aℓ) so that it also acted as an electromagnetic screen. The gas used was commercial 80% Ar/ 20% CO_2 which was chosen as being the optimum combination of drift and ionization properties[25] and practical and economic availability. It was passed at a typical running rate of 1 litre/min through a baffle system to ensure complete flushing of the chamber. (The typical purging rate was 10 litre/min and a safe purge period was 1 day.)

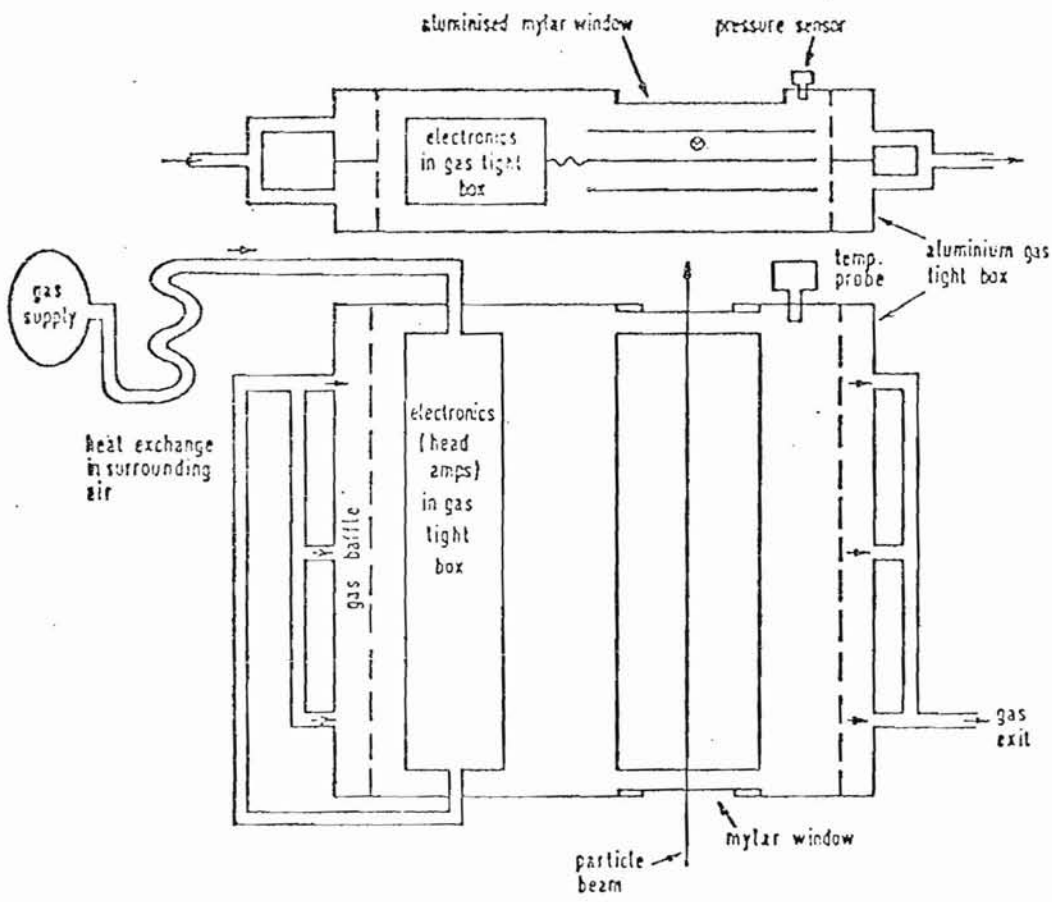

Fig.4.5 The gas system of the NAL chamber

The pressure and temperature of the gas in the chamber were monitored continuously and were assumed uniform throughout. The electronics was contained in its own gas-tight box flushed independently of the main gas box (see Fig.4.5), so that the possibility of a temperature gradient being set up across the chamber from the heat dissipated by the electronics contained in it was reduced.

Facilities to measure the oxygen concentration in the chamber were incorporated in the system but at the time of experiment the oxygen meter failed. (Oxygen causes electron attachment, consequently attenuation of the signal seen.)

The X-ray source was mounted in a box above one of the 1.5 cm samples (Channel 2) during data taking runs. It shone in through an aluminized Mylar window on the top side of the gas box. A diagram of this X-ray box is shown in Fig.4.6.

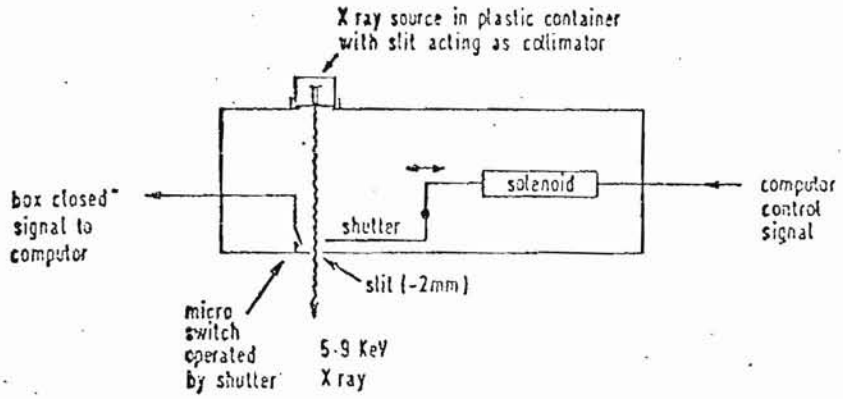

Fig 4·6 X ray shutter box

To conclude this section some mechanical aspects of construction are detailed.

Uniformity of gas gain and drift field in the device demand drift electrode spacing, wire plane positioning, wire spacing, and wire tensioning to be very accurately defined. (See calibration table, p.64 for exactly what this means.) With this, the problem of electrical insulation must be considered. A photo of the detector out of its gas box is shown on the following page. The lower drift electrode was a $\frac{1}{4}$" aluminium

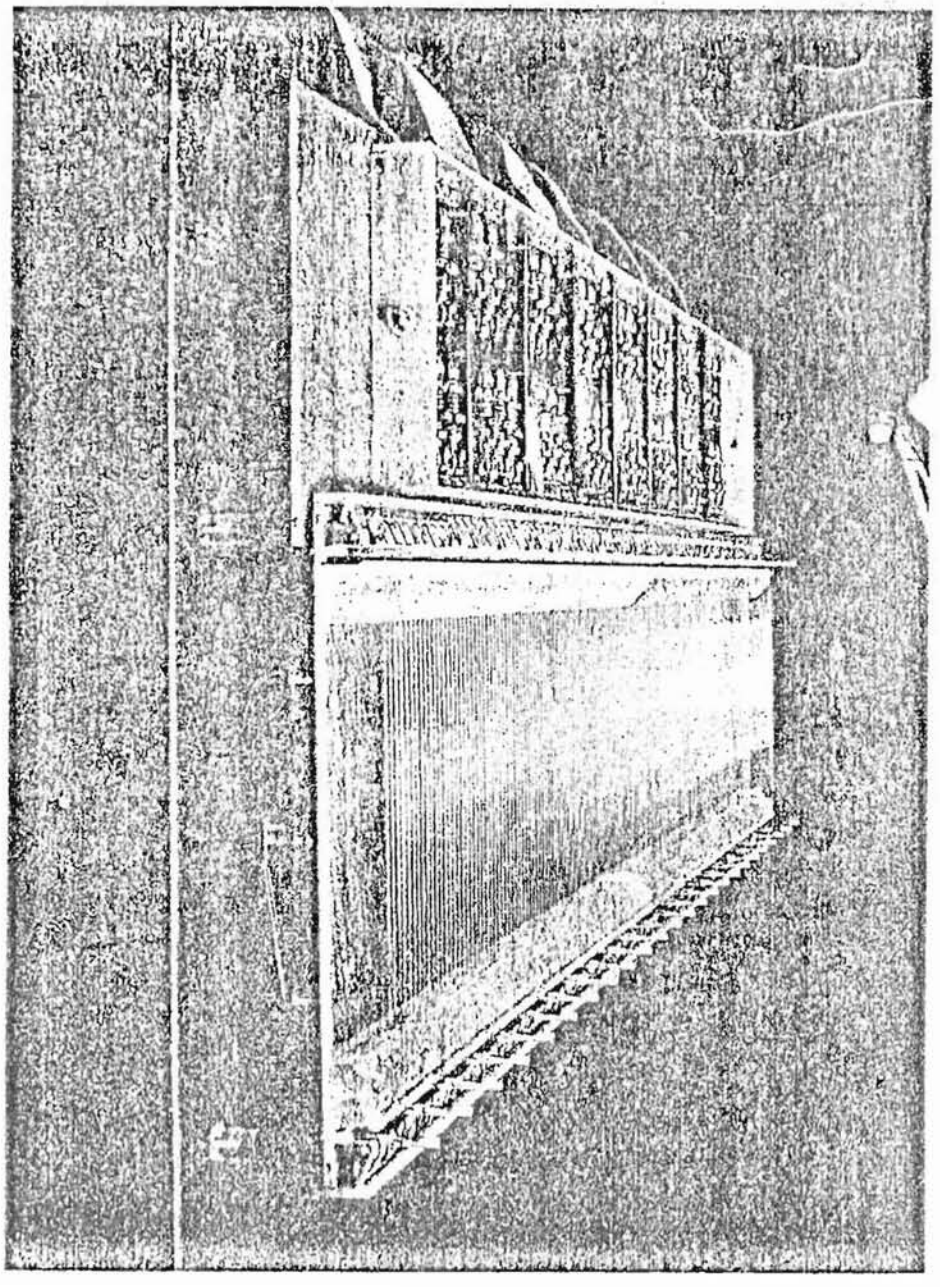

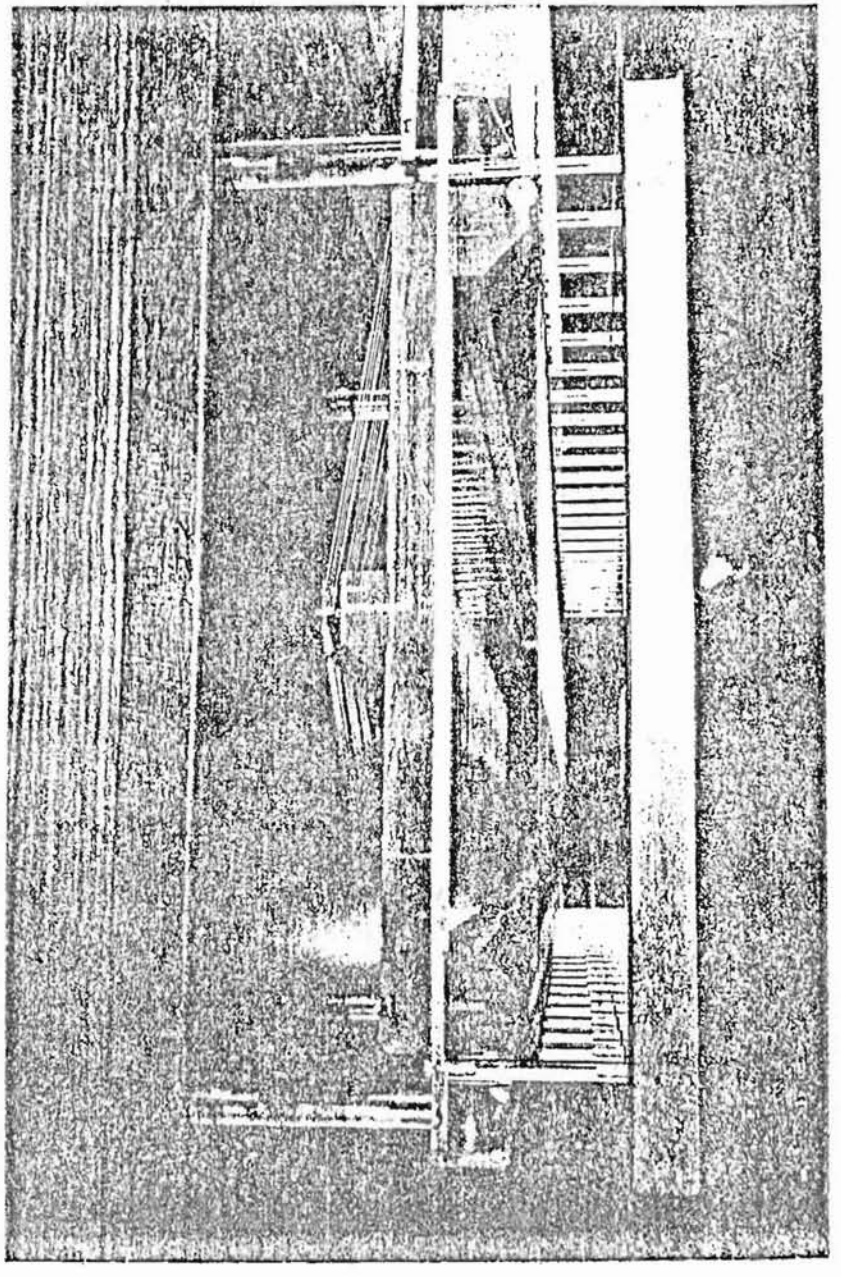

jig-plate. This provided the mechanical rigidity required and was the reference plane of the active region, i.e. the wire plane and top drift electrode were defined parallel to this lower plate by spacers.

The method of tensioning the cathode wires can also be seen in the previous photograph. These were complete loops of wire held under the jig plate by a tensioning screw. The reason for this arrangement was to stop the jig plate distorting by ensuring forces on either side were as symmetrical as possible. They were each tensioned to 8 kgs by tuning them to F natural.

The signal wires were mounted by soldering to a printed circuit board at either end. Each wire was tensioned by hanging a weight of 30 gm on it while soldering.

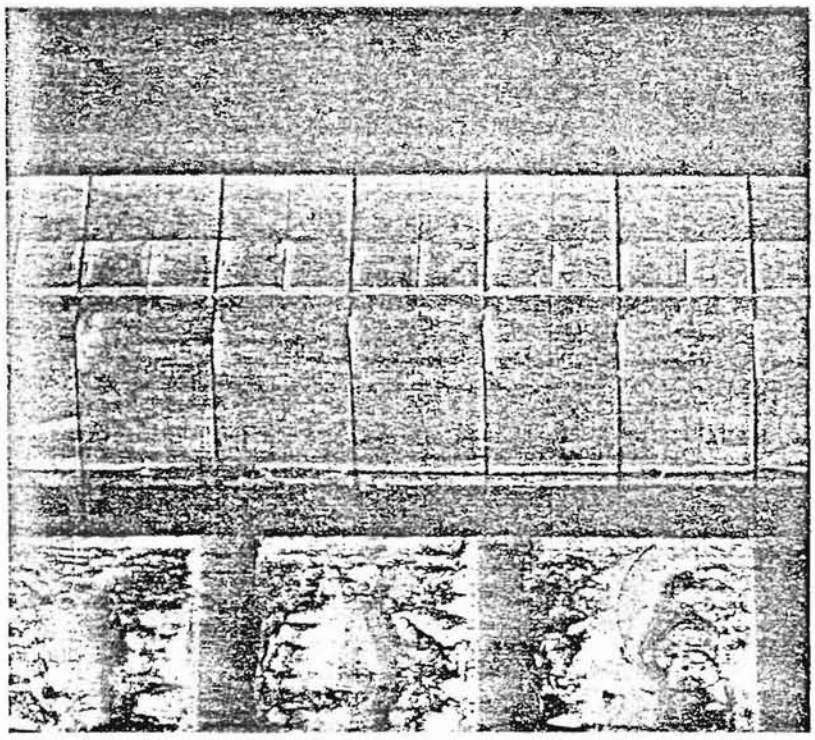

Accurate wire spacing was achieved by melting slots in a perspex rod using a securely mounted heated razor blade (see above photo). The rods were slotted when already mounted to the lower jig plate. The jig plate was in turn mounted on a mill bed, so the accuracy of the spacing of the slots was

equal to the accuracy of positioning the mill bed. The spacing was checked using a travelling microscope and was found to be good to < 8 μm for the signal wires which was very satisfactory.

our accuracy
$1.5\times10^{-3}\,\text{in} \times 2.54\,\text{cm/in} \times 1\,\text{m}/100\,\text{cm} = 3.81\times10^{-5}\,\text{m} = 38\,\mu\text{m}$

The top drift electrode was 1/1000" aluminium foil stretched pneumatically onto 1/16" aluminium frame strengthened on the top side, in the direction parallel to the wires of the wire plane, with fibre glass sections (see previous photo, p.40). This electrode was mounted on perspex pillars, machined to 3.5 cm, attached to the lower jig plate electrode. The spacing of the top electrode relative to the bottom one was tested, before the wires were put in, using a very sensitive capacitor bridge technique, (see Fig.4.7). Two metal plates were held by a perspex support near the two drift electrodes respectively, in such a way as to form two capacitors. The change in capacitance of the top capacitor with respect to the bottom one, was measured while the support was moved around the active region. Typical changes of 40 μm in the spacing were measured.

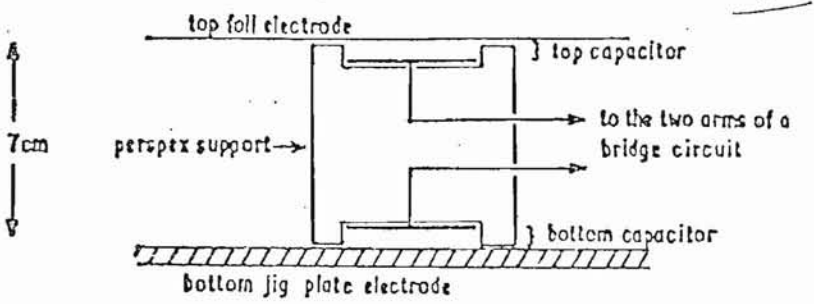

Fig.4.7 Capacitor Bridge Technique

The leakage current between drift electrodes and ground was measured as 8 nA, and that between cathode wires and ground as 4 nA. These were both satisfactory. (A typical mean signal current was 1 μA.)

As can be seen in Table 4.6 the mechanical tolerances achieved were very satisfactory, and some useful techniques were learnt for future chambers.

IV.3.2 The Electronics

The electronics section is divided into (A) measurement of the signal received, and (B) the logic for recognizing a good event and rejecting or flagging an unwanted one.

(A) is shown in Fig.4.8 and in the diagrams and tables on the following three pages.

Fig.4.8 Measurement of signals received

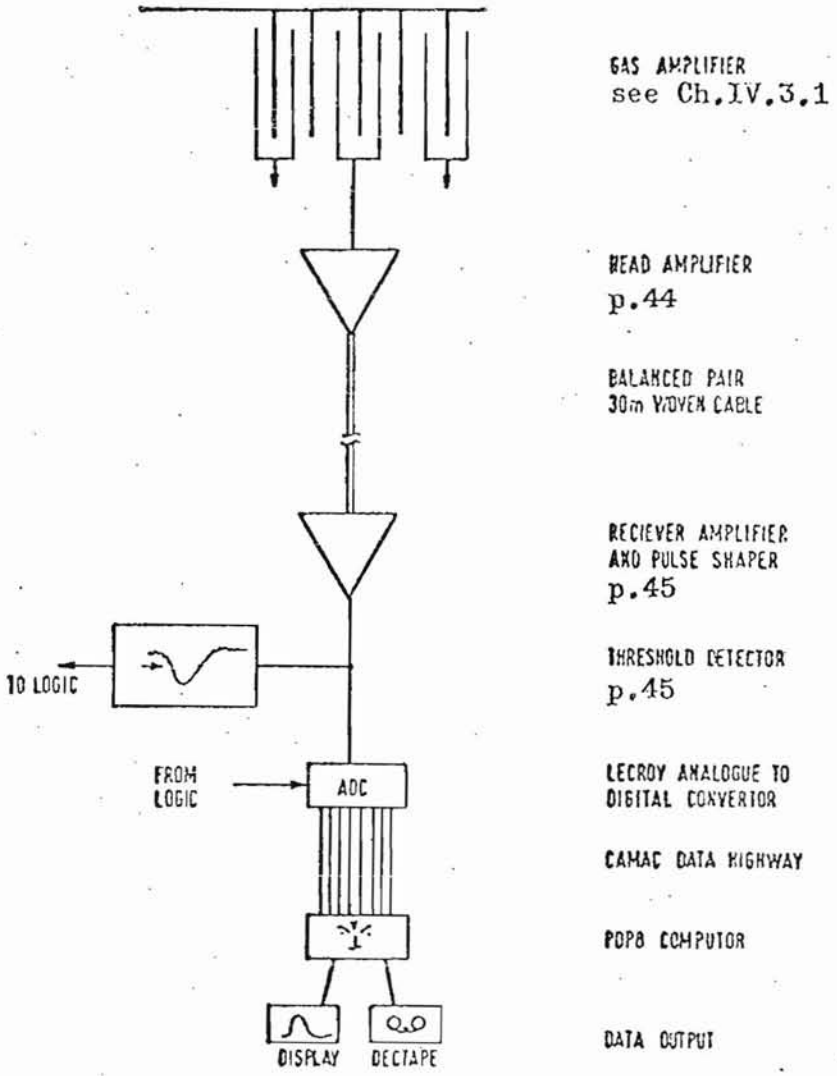

Fig.4.9(a)

Head Amplifier-low i/p impedance amplifier - ref (26)

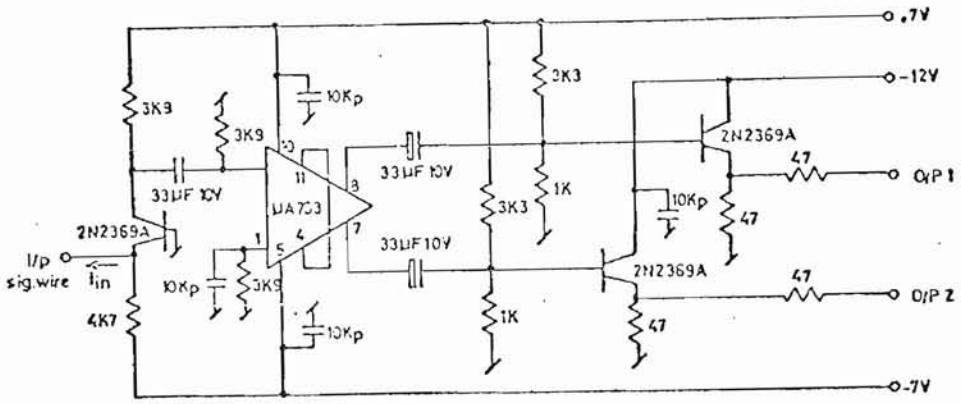

TABLE 4.1

SPECIFICATIONS OF HEAD AMPLIFIER

Rise Time	7 ± 1 ns
Propagation Time	6 ± 1.5 ns
Fall Time	11 ± 2 ns
I/p Impedance	~ 20 Ω
O/p Impedance	50 ± 1 Ω
Gain O/P 1 , 2	39 ± 2 mV/μA
Noise (10 MHz BW)	0.8 ± 0.05 mV rms
O/p d.c. offset	0.3 ± 0.03 mV

Fig.4.9(b) Receiver amplifier and pulse shaper ref. (26)

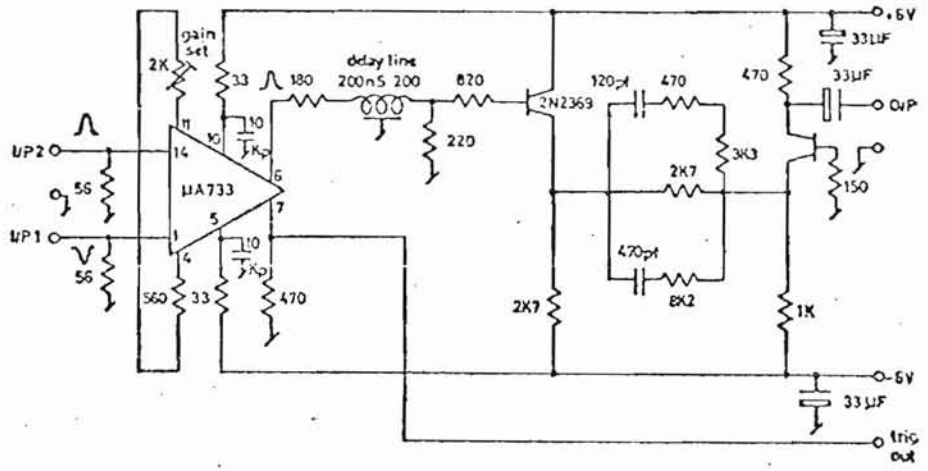

Fig.4.9(c) Receiver amplifier and threshold detector

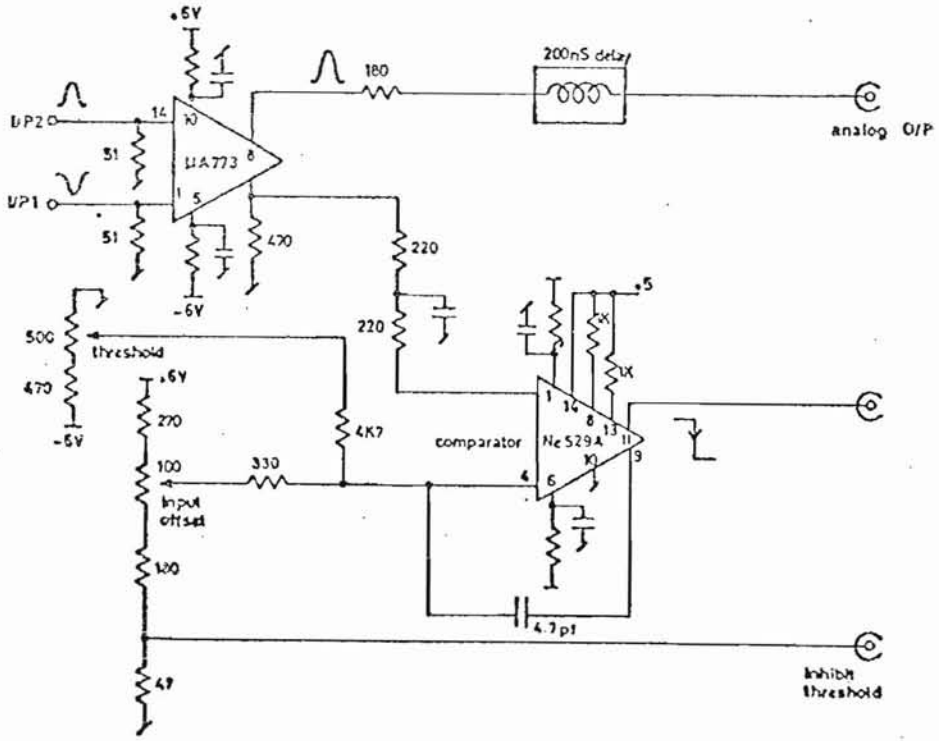

TABLE 4.2

SPECIFICATIONS OF RECEIVER AMPLIFIER

Trigger O/P : (3.3 kΩ load)	Voltage gain	~ 9
	Rise time	~ 10 ns
	Propagation time	~ 10 ns
Shaped O/P (50 Ω load	Min. voltage gain	~ 0.5 ± 0.01 at 1.6 MHz
	Rise time	~ 25 ns
	Propagation time	~ 210 ns

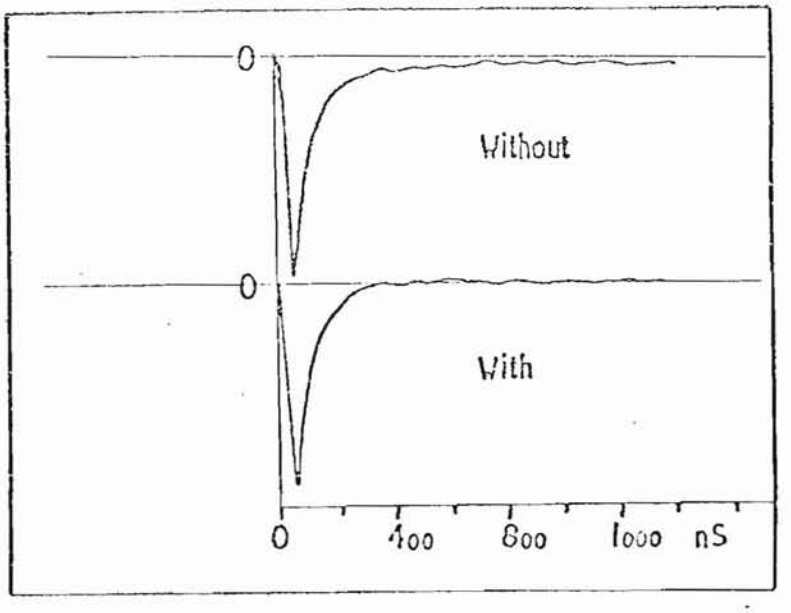

Fig.4.9(d) Trace of a photo showing the effect of the pulse shaper (see Fig.4.9(b)) and how it removes the long tail from the observed signals. This is to improve the resolution time of the detector. Each receiver amplifier had its own pulse shaper.

(B), the logic, is shown in Fig.4.10. Referring to this figure, a good event is either (1) a particle coincidence or (2) a calibration coincidence. These require the following conditions:

(1) (i) The computer recognises a 'BEAM ON' condition. This requires a signal to the computer from the accelerator control room, which is in fact the magnet ramp signal of the main accelerator ring.

(ii) Calibration information is not being received by the computer, which requires a signal from the X-ray box saying it is closed.

(iii) A coincidence between the signal wires of two of the detector's gas samples, spaced far apart from each other, implying that a particle has passed right through the detector. Channels 30 and 59 were used for this. Note these are the only channels that can be classed as self-triggering when collecting ionization data.

(iv) The appropriate Cerenkov signal corresponding to the selected particle type passing through the chamber.

(v) The absence of an inhibit signal due to (a) the computer not being ready, (b) the particle coming in a noisy interval of the mains cycle, (c) there being more than one particle going through the chamber within its resolution time, as seen by the scintillation counters, i.e. a pile-up condition.

(2) (i) A 'BEAM OFF' condition analogous to (1)(i) above.

(ii) The computer is receiving calibration information analogous to (1)(ii) above.

(iii) A trigger signal from channel 2, i.e. the channel above which the X-ray source is placed. This channel is thus self triggering in the calibration mode.

(iv) The absence of an inhibit signal analogous to (1)(v).

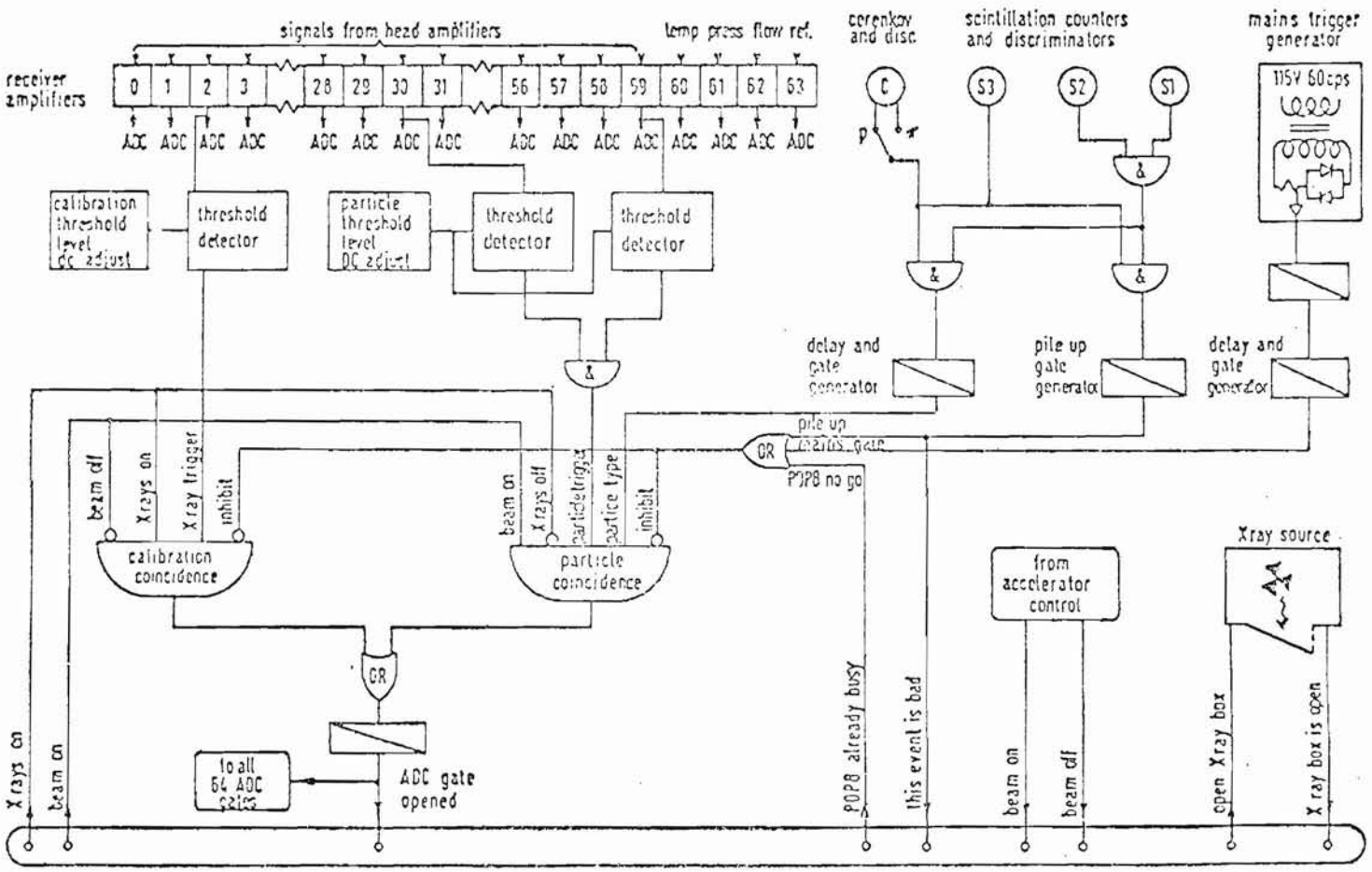

Fig.4.10 Logic diagram of NAL experiment

System status register for 2-way communication between PDP8 and logic via camac

As can be seen from Fig.4.10, two-way communication between computer and logic was by a series of bistables making up a status register. The status word of each event was recorded on DEC tape along with the event. Also a title word was recorded. This was from a register set up manually and contained information on particle type etc.

The presence of a mains trigger generator can be seen in Fig.4.10. This was incorporated since it was necessary to gate out part of each mains cycle since it was noisy for the same fraction of each cycle, probably because of the SCR stabilization of magnet power supplies etc. The effect of this gate on a fixed size test input signal can be seen in Fig.4.11.

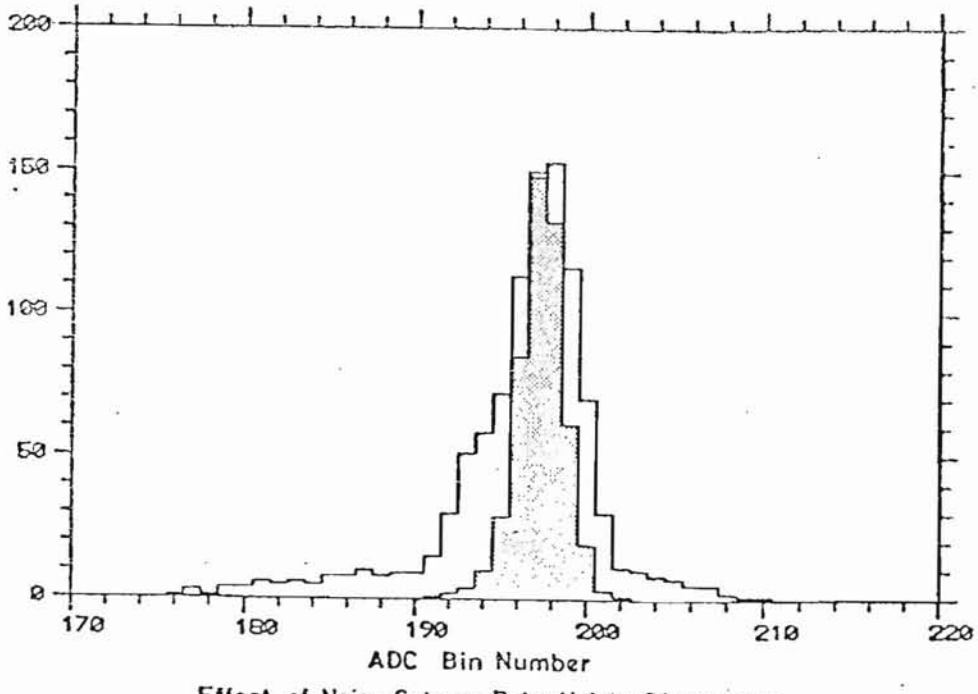

Effect of Noise Gate on Pulse Height Distribution

Fig. 4-11

IV.3.3 The Cerenkov Counter

This was an NAL facility and so was not set up or tested at the time of experiment. Operating conditions as specified by NAL and as quoted below, were assumed reliable and consequently our knowledge of this detector is limited [27,28].

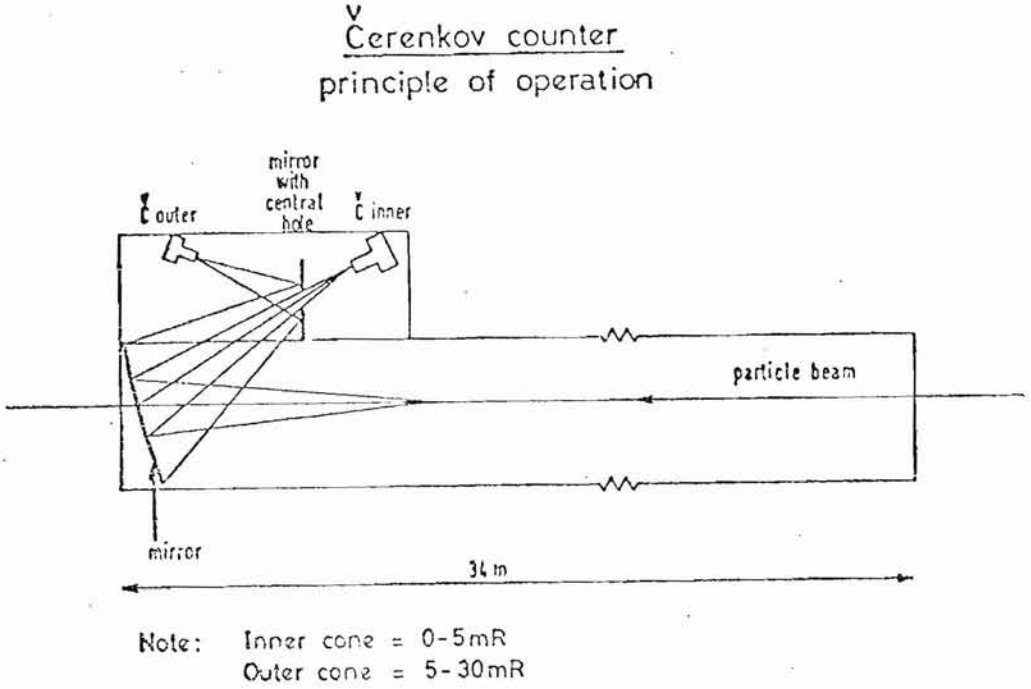

Fig.4.12

The Cerenkov was a 34 m differential counter filled with helium, capable of working at pressures in the range 0 → 14 psia. It contained two photomultipliers and a mirror system so that it was able to look separately at light contained within a cone of angle 5 mR about the particle beam and light defined between the two cones of angle 5 mR and 30 mR respectively. Fig.4.12 shows schematically the principle of operation of the counter. The operating pressures were calculated from Figs.4.13(a) and (b), and are listed in Table 4.3. To find the Cerenkov angle for 100 GeV π's, for example, from the two figures, the following procedure is adopted. From Fig.4.13(b) for 100 GeV π's the threshold pressure for Cerenkov radiation is 0.45 psia for helium. Fig.4.13(a) shows that to see the π Cerenkov radiation in the inner cone, the pressure must be less than

Cherenkov angle vs. Pressure above threshold

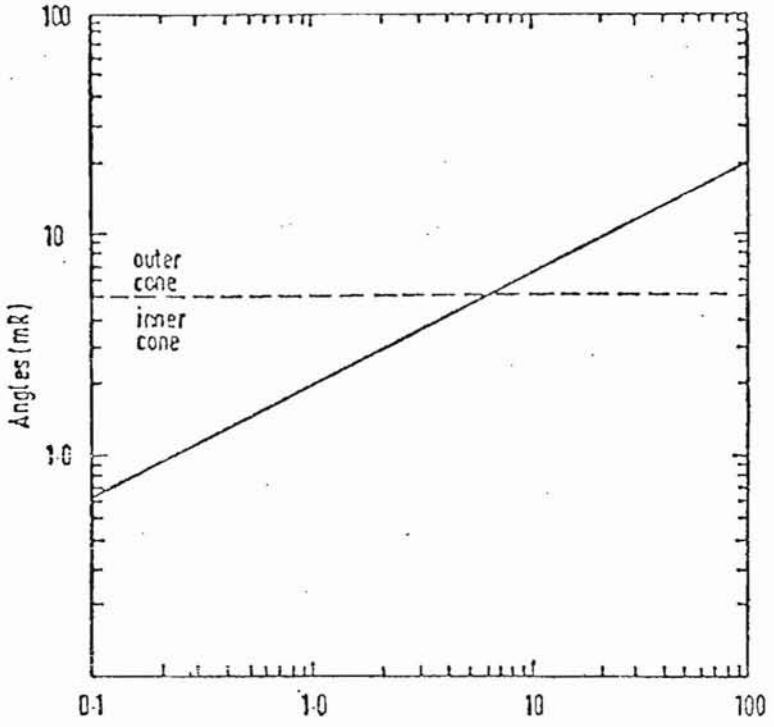

Fig 4·13a) PRESSURE ABOVE THRESHOLD (psia)-Helium

Incident particle momentum vs. Threshold pressure

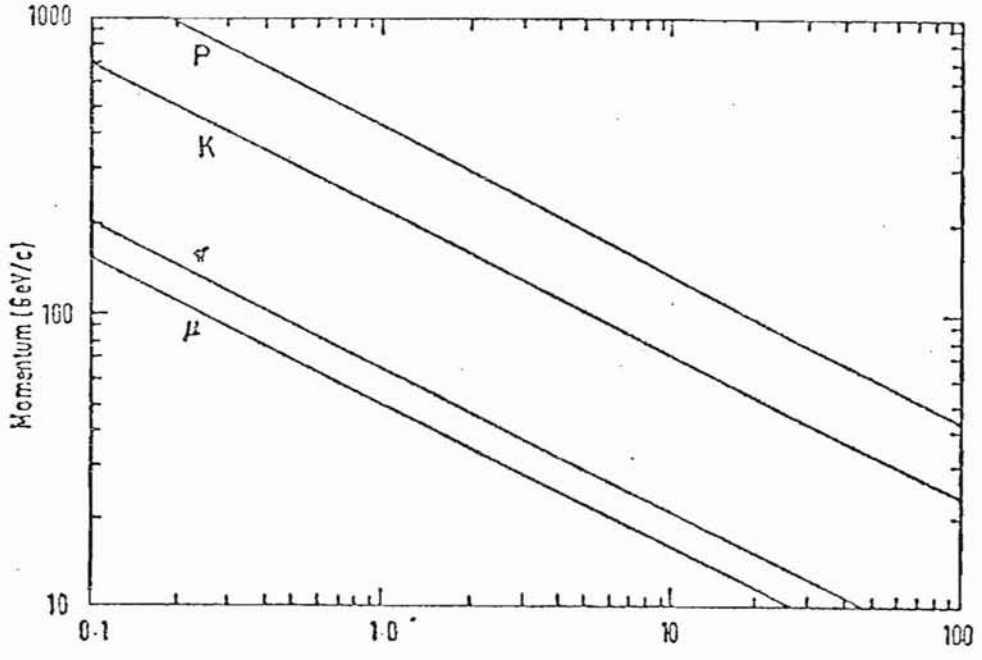

Fig. 4·13b) THRESHOLD PRESSURE (psia)-Helium

TABLE 4.3

CERENKOV OPERATING CONDITIONS

MOM.	C PRESS.	THRESHOLD PRESSURE					PRESSURE ABOVE THRESHOLD					CERENKOV ANGLE				
GeV/c	psia	π psia	K	p	e	μ	π psia	K	p	e	μ	π mR	K	p	e	μ
150	7.125	0.2	2.5	8.9	0	0.11	6.925	4.625	1.775	7.125	7.015	5.5	4.5	-	5.6	5.5
100	8.55	0.45	5.5	20.0	0	0.25	8.10	3.05	-11.45	8.55	8.30	6.0	3.65	-	6.1	6.0
50	7.01	1.8	22.0	80.0	0	1.0	5.21	-14.99	-73.0	7.01	6.01	4.8	-	-	5.5	5.2
25	11.0	7.2	90.0	>100	0	4.2	3.8	-80.0	<-90.0	11.0	6.80	4.1	-	-	7.0	5.5

The cross-over characteristics of this counter as pressure, hence Cerenkov angle, is increased are shown in Fig.4.14. C_i and C_o refer to the inner and outer mirror signals respectively. From this and Table 4.3 it can be seen that for some operating points there is the possibility of contamination of data by other particle types. These are listed in the next section.

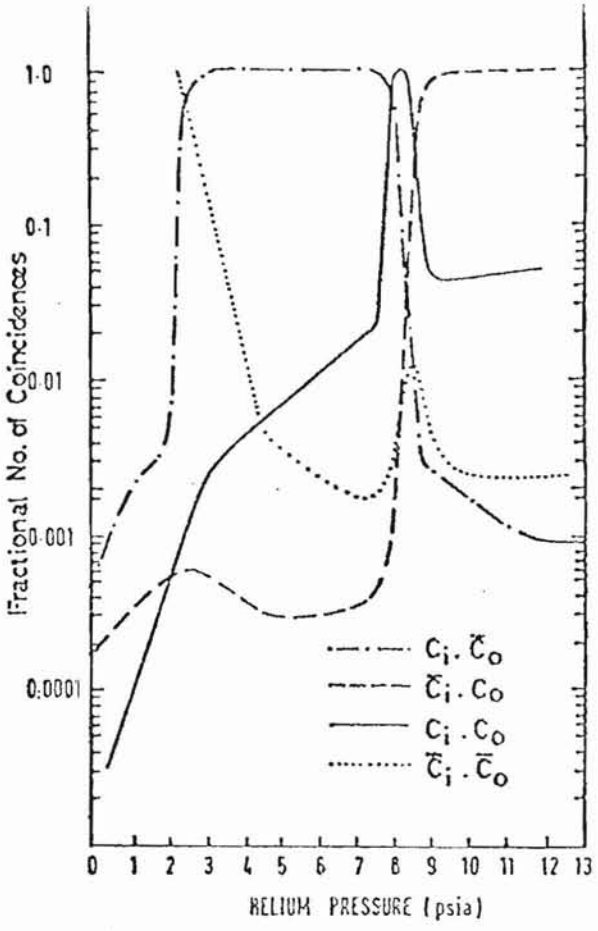

Fig.4.14

IV.4 RUNNING OF EXPERIMENT

Table 4.4 gives the main parameters of each run performed when recording ionization information. The beam spill used was either in a 'pinged' mode or a 'slow spill' mode. This choice was arbitrary as it appeared to make no difference to the resulting data. For the pinged part of the experiment the beam was being controlled by an experiment further down the beam line. Pinged spill consisted of four short bursts of particles per accelerator cycle. Each burst was 300 μs long and contained of the order of 5 particles at the ionization detector. Each burst was separated from the next by 100 ms. Slow spill consisted of one pulse per accelerator cycle of length $\sim\frac{1}{2}$ sec and containing about 20 particles. Each time a particle passed through the chamber the event, which included the outputs of the 64 ADC's, the event number, the event status word, and the title word, was recorded on DEC tape.

TABLE 4.1

RUN NUMBER	MOMENTUM GeV/c	DURATION OF RUN hours	NUMBER OF EVENTS	BEAM SPILL MODE	PARTICLE TYPE	POSSIBLE CONTAMINANTS	CHERENKOV SETTINGS psia He
30	150	3	5264	Ping	p	-	7.1 Below Threshold
					π	μ, e	Outer Mirror
31	150	4	5756	Ping	p	-	7.1 Below Threshold.
					π	μ, e	Outer Mirror
32	50	1.5	3253	Slow	p	K	7.0 Below Threshold
33	100	1.5	5800	Slow	p	-	8.5 Below Threshold
					π	μ, e	Outer Mirror
34	25	4	5345	Slow	p	K	11.0 Below Threshold
					π	μ	Inner Mirror
					e	μ	Outer Mirror

During that part of the accelerator cycle for which there was no spill, calibration data was recorded, i.e. the X-ray source box was opened. This data, which all came from channel 2, was histogrammed in core. The histogram was written to DEC tape and then zeroed once every twenty minutes approximately.

Before recording ionization information the chamber was scanned over its whole area for non-uniformity of gain, etc., and ADC 's and amplifiers were adjusted to have equal pedestals, gains etc. The results of this preliminary period are outlined in the calibration section following.

The following peculiarities existed in the 60 signal wire channels:

(1) Channel 2 not only acted as a normal ionization measuring channel but also acted as the self-triggering channel for looking at X-rays from the calibration source in otherwise idle times.

(2) Channel 59 was one of the two channels that made up the particle trigger coincidence. As can be seen later in Fig.4.16 (point marked 'trig'), this leads to its average signal size being biased large.

(3) Channel 30 was the other channel in the particle trigger. ADC 30 did not work and so the ionization information on this channel was lost (despite the fact that it would have been biased anyway).

(4) Channel 58 was not a conventional channel. The electronics of this channel were connected to a pair of thick 250 μ wires at the far end of the chamber outside the 'active' region (instead of the normal 25 μ signal wire). Because of the increased radius no appreciable gas amplification could take place around these two wires. Hence the signals seen on this channel were those due to noise and pick up. An interesting effect was observed in this channel and will be discussed later in the analysis (p.66).

IV.5 CALIBRATION OF NAL DATA

The preliminary calibration and setting up problems at the start of the experiment are concerned with the linearity and uniformity of the measuring system. Working in order down the system, the following measurements were made.

(i) Uniformity of gas gain down the length of each signal wire. This was measured by scanning signal wires down their length with a collimated X-ray source, (see Fig.4.15). Typical variations in gain were < 2%. The large drop in one of the scans of Fig.4.15 is the fall off of gain as the end of the wire is reached. It is not in the central 10 cm of the wire length used for measurement.

we have some variation ≤ 2%

(ii) Uniformity of gas gain from signal wire to signal wire. Two separate measurements were made: (a) A collimated X-ray source was scanned across the signal wire plane at right angles to the signal wires. The variation in gain was 2% (rms deviation from mean signal size). (b) The peaks of the Landau distributions for 25 GeV/c protons obtained from each of the 58 channels were compared, see Fig.4.16. The variation is estimated as $\sigma \leqslant 5\%$. (The accuracy of this second measurement was limited by statistics.)

Depends upon constants chosen actually used

(iii) Linearity of gas gain. The signal size from a wire was measured as a function of various X-ray energies, see Fig.4.17. In the region used, i.e. 0 - 8 keV, the gas gain is proportional.

(iv) Linearity of electronics. Test pulses of similar shape to real signals were put onto each signal wire. For each channel a scan was made of ADC output versus size of input test pulse, see Fig.4.18 for a typical channel. All channels were very similar to this one. The size of the test pulse is measured in arbitrary 'equivalent volts', since the voltage actually measured should be multiplied by an unknown constant factor to obtain the actual peak size of the test pulse in volts.

(v) Linearity of ADC's. Before performing (iv) above, the zero current of each of the ADC's was adjusted such that the required range of signal wires was in the linear region of the ADC's response.

(vi) Constancy of the ADC integration gate time. This was checked throughout the experiment by putting a fixed d.c. reference voltage into one of the ADC's (ADC 63). Its output was never observed to vary. All ADC's used the same gate signal.

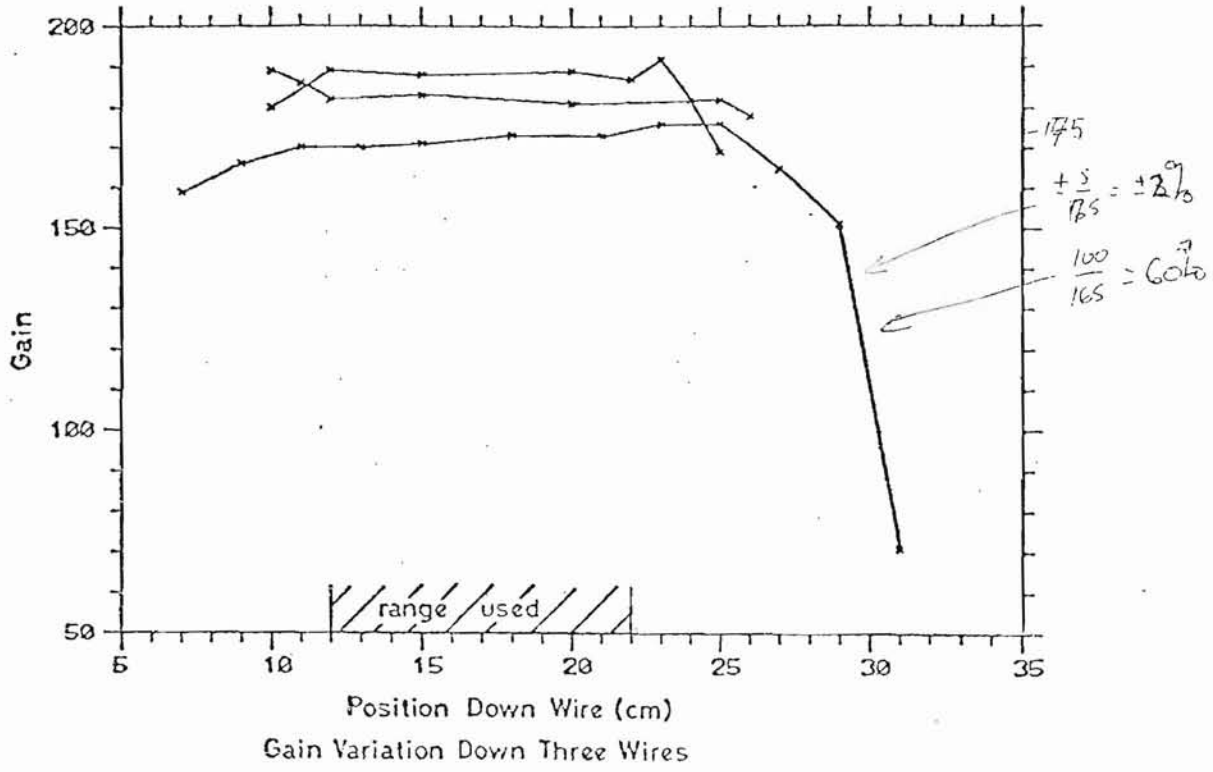

Gain Variation Down Three Wires

Fig.4.15

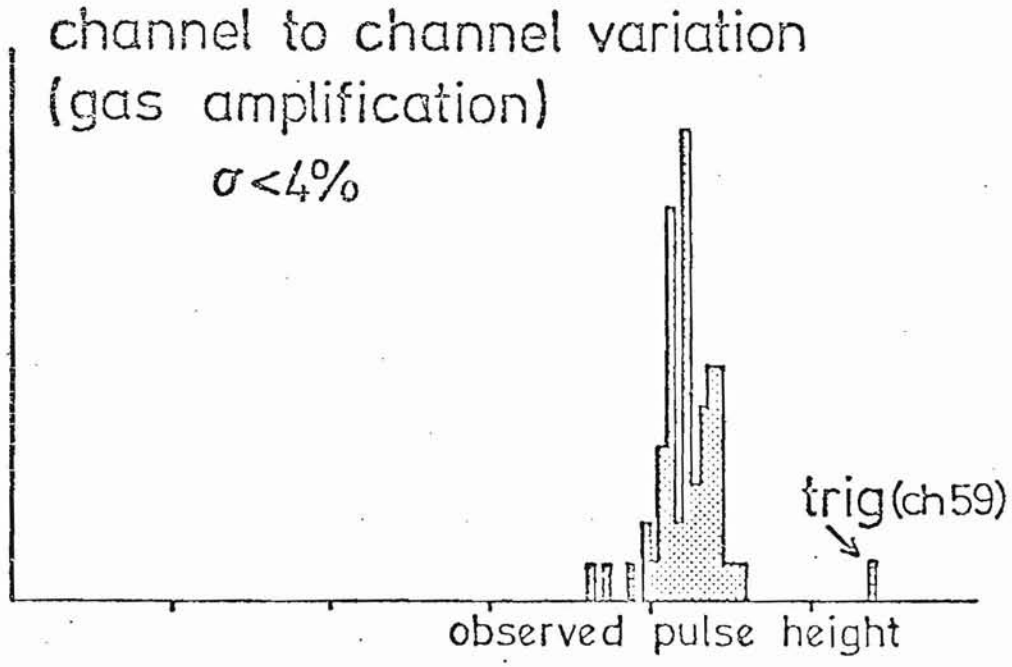

Fig.4.16

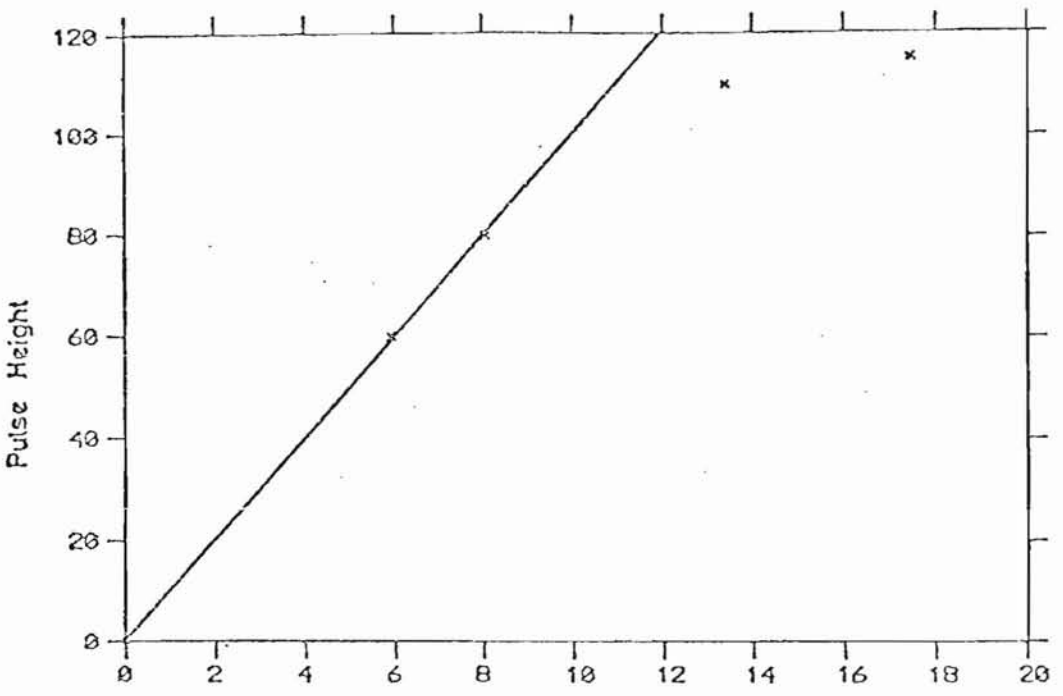

Proportionality of Gas and Electronic Gains

Fig.4.17

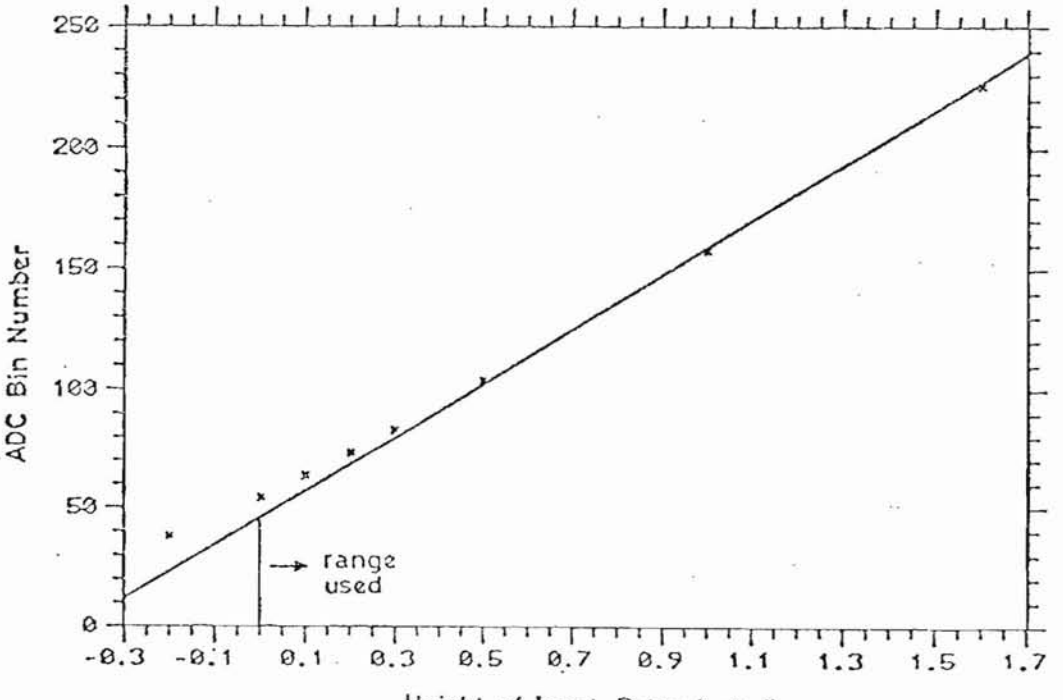

Proportionality of Electronics

Fig.4.18

The calibration of the detector during the time that ionization data was being collected was by use of the X-ray shutter box. Fig.4.19 shows a typical calibration spectrum obtained while running. The main peak corresponds to the ionization from the 5.9 keV X-rays of Fe^{55} (caused be electron capture by the Fe^{55} nucleus with subsequent de-excitation of the Mn^{55} atom). The smaller peak is the argon escape peak at 2.9 keV. The position of the 5.9 keV peak was determined by fitting a Gaussian to it. The width of this peak is caused by fluctuations in the number of ion pairs for a given energy loss and in the gas amplification factor[29]. A table of iron peaks versus run number and the event number at which these histograms were recorded is given below.

TABLE 4.5

RUN NUMBER	EVENT NUMBER	A D C BIN NUMBER OF 5.9 keV PEAK	RUN NUMBER	EVENT NUMBER	A D C BIN NUMBER OF 5.9 keV PEAK
30	803	217.1 ± 0.2	32	1725	227.8 ± 0.2
(150 GeV/c)	1224	220.2	(50 GeV/c)	2095	228.0
	1699	223.2		3216	224.9
	2174	224.4			
	2921	226.0	33	2927	193.3
	3679	227.2	(100 GeV/c)	5308	189.1
	4615	228.3		7568	184.6
	5614	229.0			
31	836	221.2			
(150 GeV/c)	1643	221.7	34	3715	213.2
	2465	223.1	(25 GeV/c)	4972	208.3
	2984	223.0		6108	203.2
	3549	223.1		6535	200.0
	4183	222.9		6735	198.5
	4722	223.2		7084	197.3
	5479	220.9		7844	195.8
	5756	220.4		8875	195.6

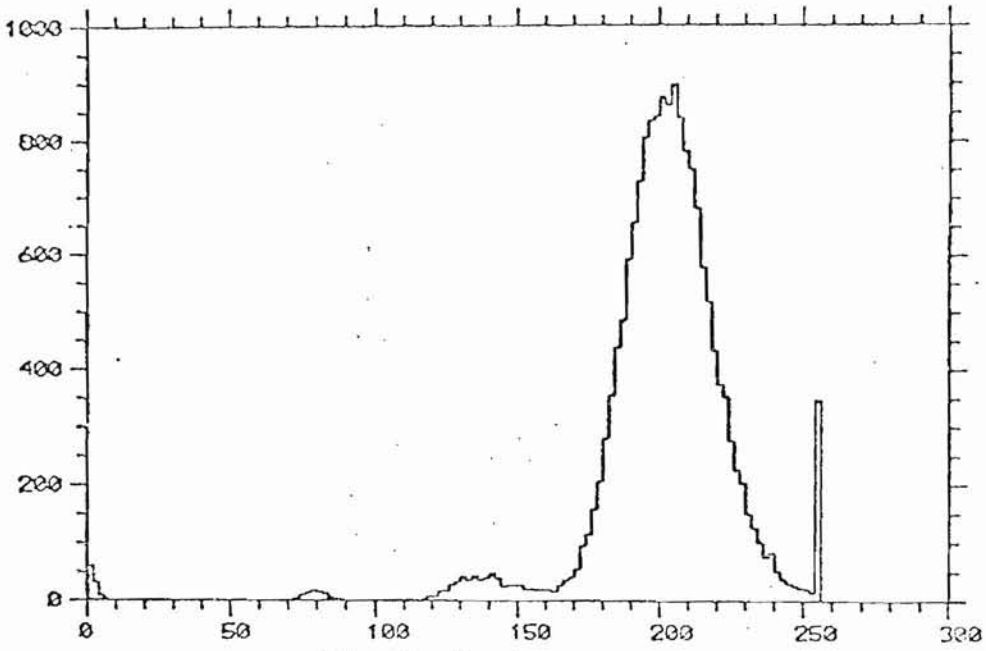

Typical Fe Calibration Spectrum
(zero energy corresponds to about 50)

Fig.4.19

Summarizing, the following steps are thus performed in the calibration of an ionization event, (i.e. the conversion of the recorded digitized output of the ADC's into the corresponding number of electron volts energy deposited in each sample)

(1) Convert each ADC output bin number to 'volts' using the conversion of the type shown in Fig.4.18. This corrects for non-linearity in electronic amplification.

(2) Interpolate between the nearest two calibration Fe^{55} X-ray peaks either side of this event in time (more precisely the interpolation is with respect to event number, not time).

(3) Convert interpolated calibration peak to 'volts' using Fig.4.18 again.

(4) Use the known energy of the calibration peak and the proportionality of the chamber to give the required result in energy units, i.e. eV.

(5) Correct the eV result further for density etc. as outlined below.

The X-ray calibration automatically corrects for variations in the gain of the gas amplifier due to variations in gas density. However it does not correct for variations in the primary ionization by the charged particle when there are variations in the gas density. This variation is small and linear, and was eliminated by converting all histograms of ionization loss to N T P using the mean temperature and pressure measured for the appropriate run.

The variation of density (= pressure/temperature) and X-ray peak during the course of runs 30 and 31, are shown in Figs.4.20(a) and (b). As can be seen, the variation of density is not a good measure of the variation of the X-ray signal size. This is at first surprising but it can be explained, and in the process leads to the following question. How well defined is the relation between the measurement of an energy deposited by an X-ray and the measurement of an energy deposited by a charged particle, and hence what is the usefulness of calibrating with X-rays? Factors influencing this relation are the following:

(a) Rate effects. If the rates of either charged particles or X-rays are too great, the accumulation of charge in the gas amplification region will change the gain significantly. This space charge effect was considered non-existent for this experiment[30], but the almost certain existence of another rate dependent effect is outlined in the data analysis following (p. 71).

(b) Gas composition effects. The distance from the signal wire plane to the conversion point of an X-ray and to the track of a charged particle, differed by ~ 2 cm in this experiment. Hence the drift distances to the signal wires of the ionization electrons in the two processes are different. Therefore, if there is a change in gas composition, the two processes can be affected in different ways. For instance any oxygen present will attenuate the signals (by attachment of electrons to the oxygen molecule).

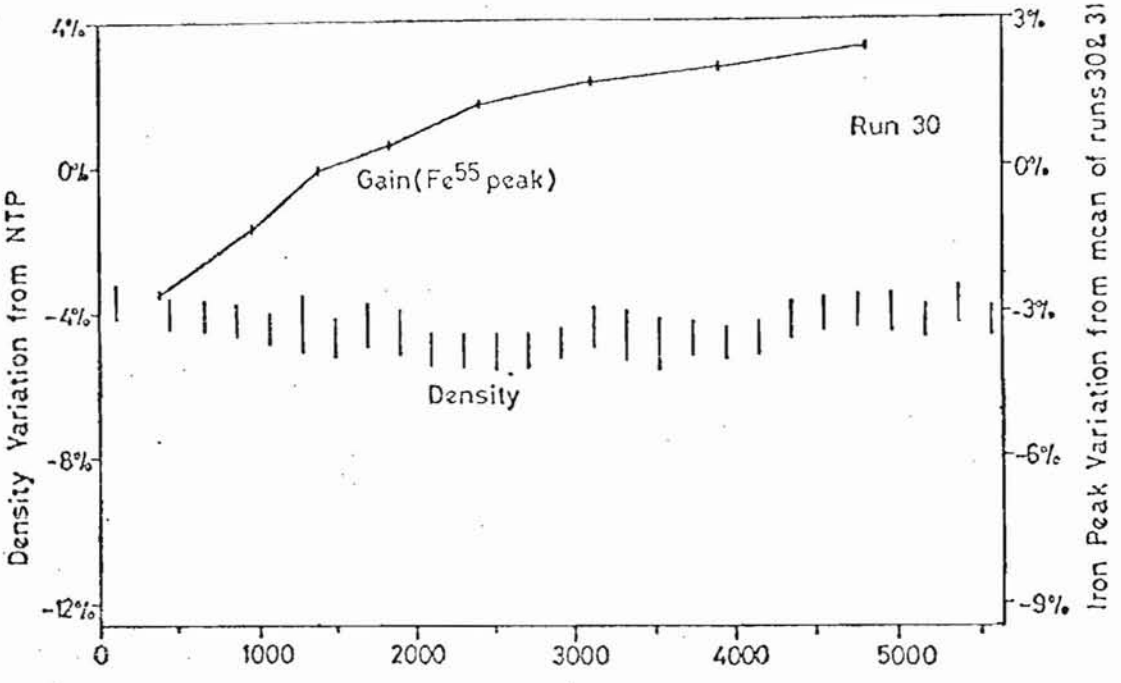

Fig.4.20(a)

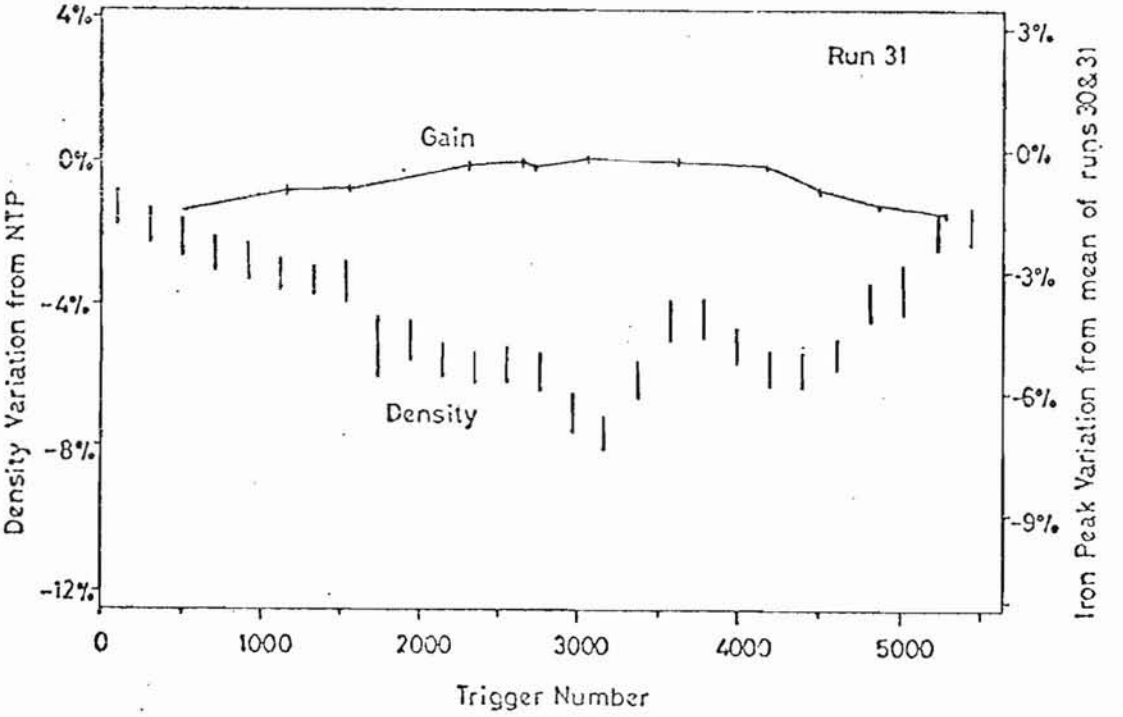

Time Variation of Gas Density and Gain for Runs 30 and 31

Fig.4.20(b)

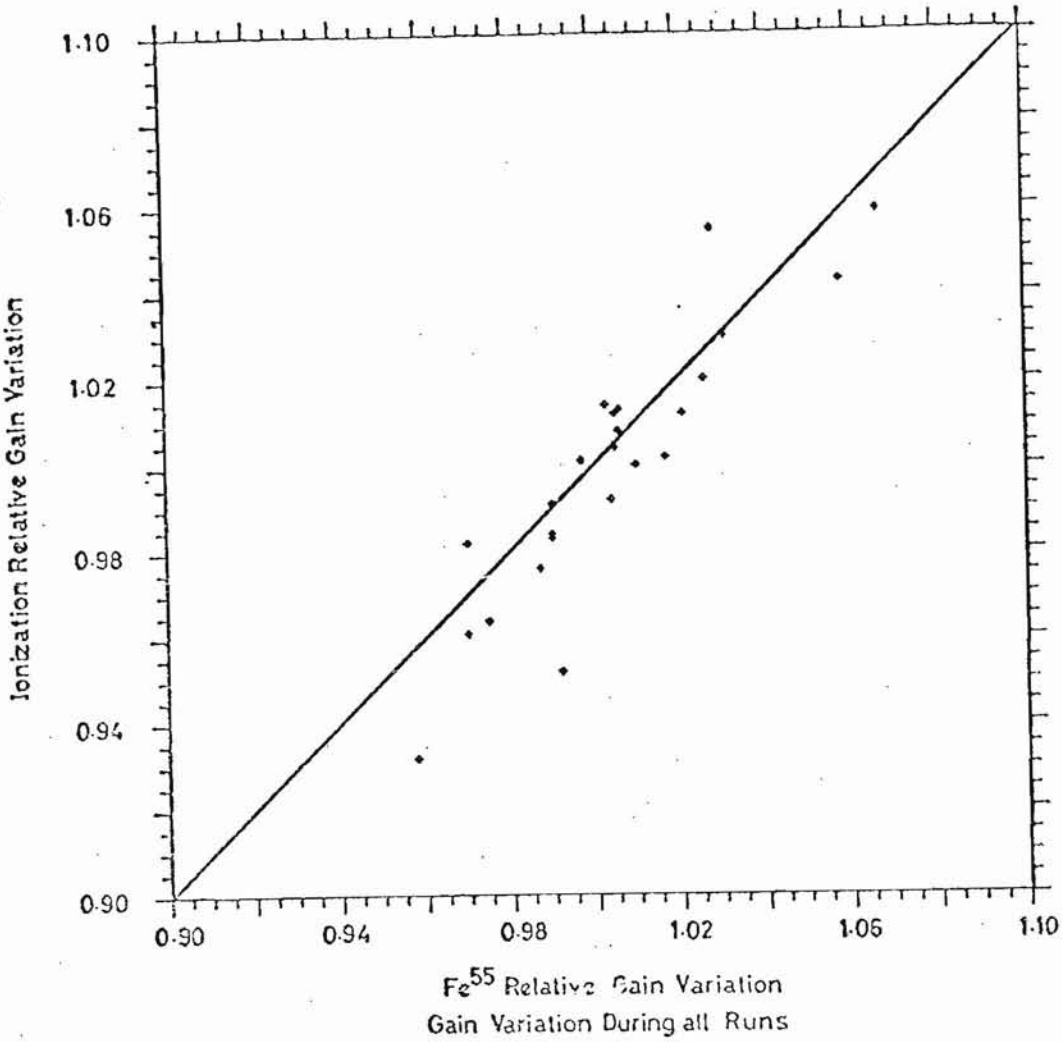

Fig.4.21

In Fig.4.21 a plot is made of the variation within a run of gas gain as measured by X-rays against the gain as measured by the mean ionization of a particular type of charged particle. It should be emphasized that although this plot contains points from all runs it only contains information about gain variations within a run. (The 'gain variation' as measured by mean ionization would of course vary between runs !) The variation of points from the straight line is this figure give $\sigma = 1.5\%$. Unfortunately it is not justifiable to say that this will be the typical magnitude of the variation between runs, since the time intervals between them were large and also not much is known about changes of gas composition between the different gas bottles used in different runs, or about changes in beam fluxes. However, two supposedly identical runs (30 and 31

at 150 GeV/c) were made at different times and the change in the position of the calibrated mean ionization, for π's and p's, is 3.3% between these two runs. It will be assumed that this is typical between any other two runs.

Here a summary is made of all the errors involved in the calibration. First there are the factors that cause the gain to vary within a run and which act in such a way as to widen the Landau distributions that would otherwise be obtained. These are mainly caused by the mechanical tolerances of the detector and the accuracy of the electronics. Table 4.6 summarizes these factors. Secondly, there are the factors that cause gain variations between runs. These are thought to be gas composition and/or rate effects. Thirdly, there is the possibility of a systematic shift of the Landau distributions, as yet not discussed.

TABLE 4.6

SOURCES OF GAIN VARIATION WITHIN A RUN

Source	Measurement	Variation	Effect on Gain (σ)
1. Drift voltage stability in absence of charged particle	Digital voltmeter	$< 10^{-3}$	
Drift voltage ripple	Oscilloscope	$< 10^{-3}$	< 0.7%
HT wire voltage stability in absence of charged particle	Digital voltmeter	$< 10^{-4}$	
HT wire voltage ripple	Oscilloscope	$< 10^{-4}$	< 0.1%
LT power supply and other sources of short term electronic gain variation, e.g. random electronic noise	Observed dispersion of test pulse response averaged over all channels (see Fig.4.11)	$\sim 10^{-2}$	~ 1.0%
4. Gas gain variation with time within a particular run, e.g. due to gas composition variations, fluctuations of d.c. level shift	See Fig.4.21	15×10^{-3}	1.5%
5. (a) Gas gain variation along wire	X-ray scan See Fig.4.15	$\leq 20 \times 10^{-3}$	< 2.0%
(b) Gain variation from wire to wire	X-ray scan	20×10^{-3}	2.0%
	Charged particles See Fig.4.16	$\leq 50 \times 10^{-3}$	$\leq$ 5.0%
5(b) includes:			
(i) Wire diameter variation	Laser diffraction	< 0.2 μm	~ 2.0%
(ii) Signal wire position	Travelling microscope	< 8 μm	
(iii) HT wire position	Travelling microscope	30 μm	
(iv) Drift electrode position	Capacitor bridge	40 μm	~ 2.0%

IV.6 INTER-CHANNEL CORRELATIONS

If the ionization data is calibrated as in the previous section, the Landau distributions obtained have peaks very much lower than expected from theoretical predictions and other previous comparable experiments. This is mainly caused by a serious problem which could not be completely rectified at the time of experiment (because of lack of time and components). It was due to insufficient decoupling capacitance of the drift electrodes and cathode wires to ground. Thus when a charged particle passed through the chamber, the voltage changes on each of the signal (anode) wires contributed, via capacitive coupling, to voltage changes on the drift electrodes and cathode wires (the latter were connected together). This meant that each signal wire was seeing effects due to the other (150-1) signal wires. These d.c. level shifts of the high voltage electrodes reduced the observed signal sizes. A very crude estimate of the magnitude of this effect can be made as follows. In Fig. 4.22, a picture which is a very rough approximation of the circuit causing this effect is shown.

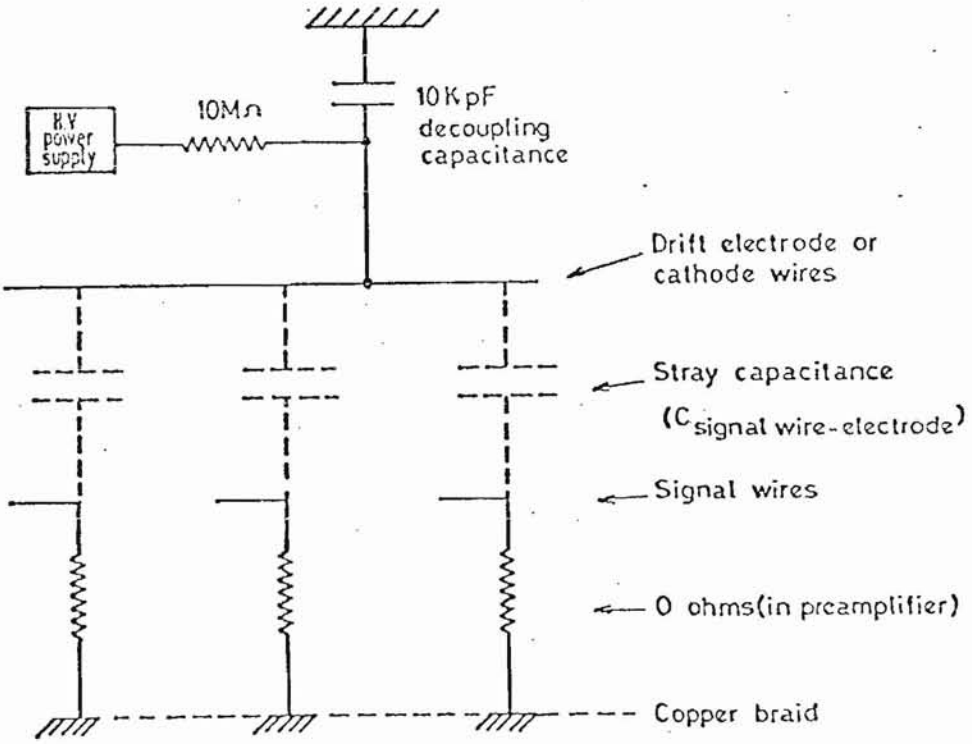

Fig. 4.22

A rough idea of C(signal wire - electrode) is obtained from the standard formula for a wire to plane capacitance[31]:

$$C = \frac{2\pi\epsilon\epsilon_o \ell}{\ell n(2d/a)}$$

where ℓ is length of wire, d is wire to plane spacing, and a is wire radius. In our case $\ell = 0.35\,m$, $d = 3.5\,cm$, $a = 0.0025\,cm$ giving $C \approx 2\frac{1}{2}$ pF. Thus if it is assumed the total stray capacitance per signal wire is $7\frac{1}{2}$ pF (two drift planes and cathode wires $\Rightarrow 3 \times 2\frac{1}{2}$, and since there are 150 signal wires (including signal wires not coupled to electronics) then the induced signal on any pair of wires (for each sample) is of order

$$2 \times \frac{C(\text{signal-electrode})}{C\ (\text{decoupling})} \times (150 - 2) \times \begin{pmatrix}\text{original mean}\\ \text{signal size}\end{pmatrix}$$

$$\approx 0.23 \times (\text{original mean signal size})$$

where we have considered the stray capacitance to a signal wire and the decoupling capacitance acting together as a voltage divider.

This effect is estimated as described later in this section, to be - 25% but because this figure cannot be obtained accurately by measurement or calculation, it forces one unknown normalization parameter into the results. This effect was also seen on channel 58 with the dummy signal wires (see p. 55) i.e. a small positive signal was observed (a genuine signal due to an ionization event is negative going), but since this channel was not calibrated for positive signals (where the ADC response is nonlinear) no quantitative information could be obtained.

Another less important source of interchannel correlations was the nearest neighbour cross-talk due to stray capacitance between signal wires in adjacent channels. This cross-talk was measured, using a calibration X-ray source to be $-(3 \pm 2)\%$.

effects between samples due to δ rays, (i.e. high energy electrons from primary ionization in one sample travelling through into an adjacent sample causing secondary ionization on their way). The magnitude of any δ ray effect is estimated from reference (32) to be of order 1% for adjacent channels and from this experiment, all that can be said is that it is very much smaller in magnitude than 4.5%, the capacitative cross talk magnitude.

With the above problems in mind it was decided that the best procedure for attempting to handle inter-channel correlations was the following:

(1) Nearest neighbour cross talk. Two calibrated Landau distributions, (i) and (ii), are obtained for the events in channel N when the signals measured in channel N+1 are (i) larger than average, and (ii) smaller than average. The difference between these two Landaus is compared with the shape of similar plots obtained theoretically with different values of nearest neighbour cross-talk. (Of course for zero cross-talk and high statistics there is no difference between these two Landaus.) This procedure gives a rough estimate of the nearest neighbour cross-talk, e.g. see Fig.4.23(a) where the experimental difference histogram is shown with one of the Landaus used in the subtraction, and also with the curve of the best theoretical Monte-Carlo fit. (The 'best fit' is taken as when the positive going peaks of theory and experiment are approximately the same height. The odd looking overflow bins are due to the imperfect calibration causing the overflow bins of the 58 contributing ADC's not to overlap precisely.)

The best theoretical fit was taken as given by

$$\alpha = -0.045 \pm 0.01,$$

where α is defined by

$$\epsilon_i = \alpha E_{i-1} + E_i + \alpha E_{i+1},$$

where ϵ_i is pulse height observed on channel 'i' and E_i corresponds to the charge actually collected by that

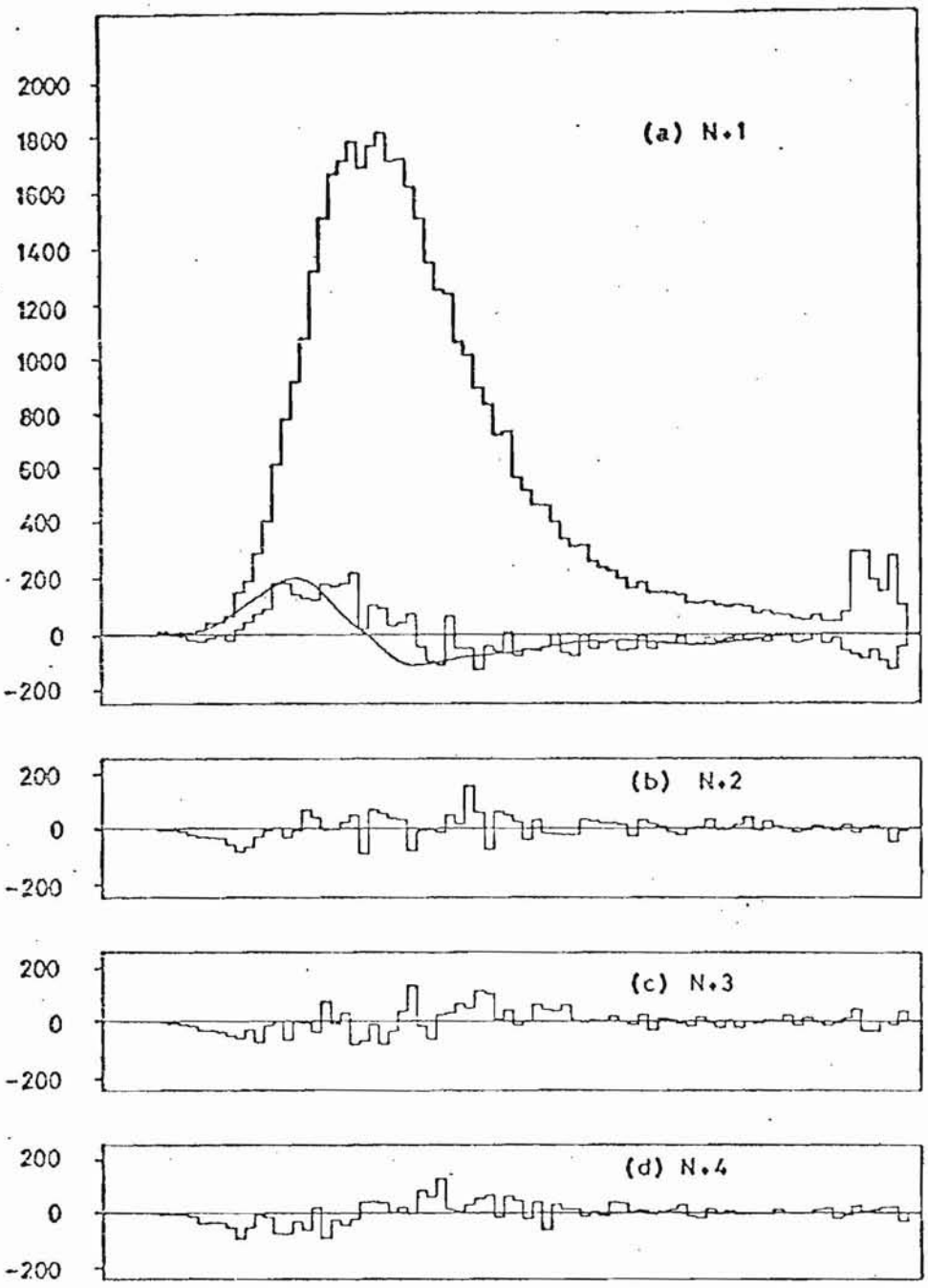

25 GeV/c Protons

Cross Talk Difference Plot

Fig.4.23

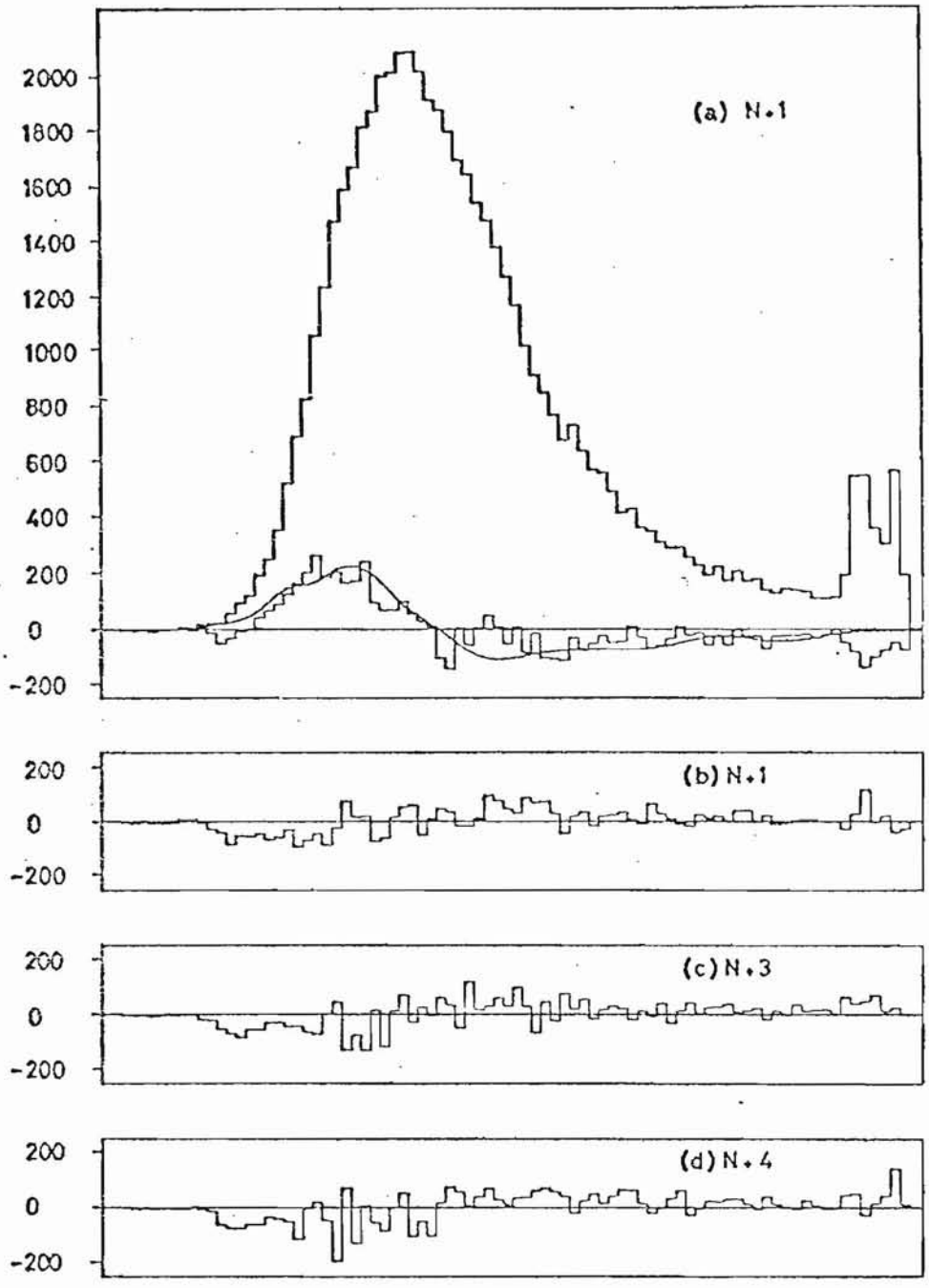

25 GeV/c Electrons
Cross Talk Difference Plot

Fig.4.24

channel. (The ±0.01 comes from the definition of 'average'. Here it is defined such that the two Landaus, big and small, have equal statistics. Different definitions can vary α by ±0.01). The plots in Figs.4.23 (b,c,d) are similar plots to Fig.4.23(a) but for channel N when N+2, 3 or 4 is big or small, i.e. non-nearest neighbours. They show that the effect just described is confined to a nearest neighbour effect. Fig.4.24 shows the same for electrons.

(2) DC level shift. For each energy and each particle, the peaks of the mean of the lowest 60% distributions* are plotted against the equivalent obtained from theory (calculated with -4.5% nearest neighbour cross-talk in it), see Fig.4.25. From the gradient of this line the unknown normalization factor, β, for the experimental data is obtained. β is defined by extending the previous equation

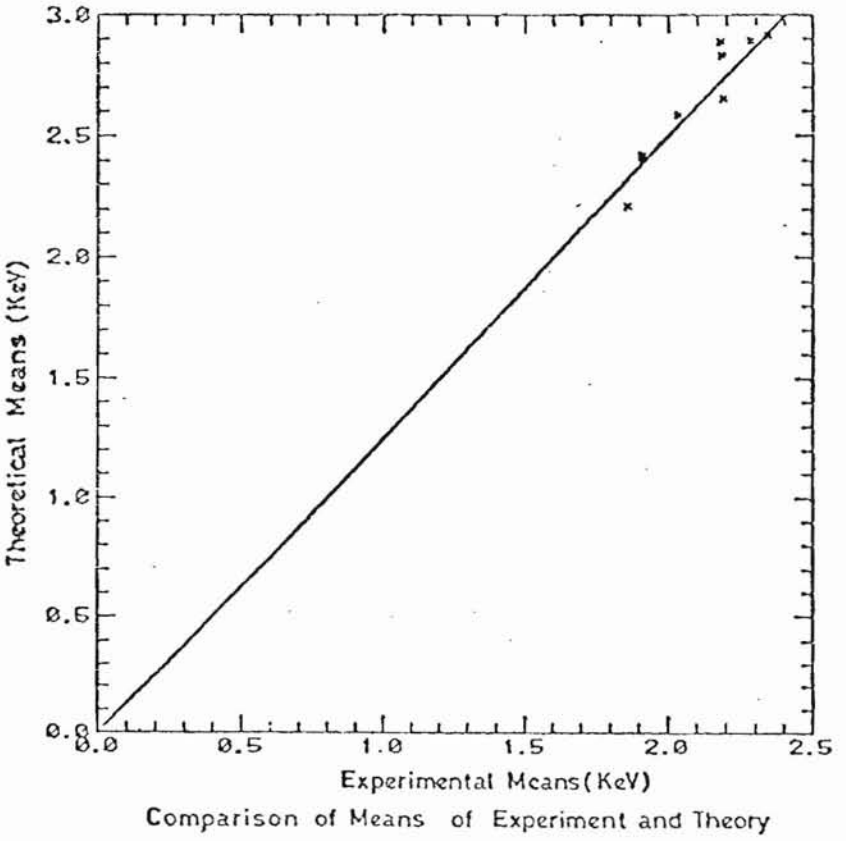

Fig.4.25

*The mean of the lowest 60% distribution is obtained as follows: for each event, find which 35 channels of the total 58 measuring ionization loss, have the smallest signals and then determine the mean of these lowest 60%.

as follows:

$$\epsilon_i = \alpha E_{i-1} + E_i + \alpha E_{i+1} - \beta \bar{S}$$

where $\bar{S}$ is a suitably defined mean ionization for a particular particle velocity. The value of β obtained was

$$\beta = 0.25 \pm 0.05 \qquad [\text{or} \quad \beta \bar{S} \approx 500 \pm 100 \text{ eV}].$$

The 'error' quoted for β is the variation of this parameter due to fluctuations in the d.c. level shift. These are caused by the Landau fluctuations of the ionization in 120 cm of gas. (120 cm = distance a charged particle travels across the signal wires.) The Landau fluctuations are typically 50% (FWHM) for this thickness of gas[33] which gives a σ of $\sim 20\%$, hence the variation of β.

Thus, in the procedure detailed above, theory has been used in two ways. Firstly, it is used to obtain a value of nearest neighbour cross-talk by fitting the shape of theoretical (Monte-Carlo) distributions to the experimental Landau distributions, (using the data from the 25 GeV/c run). The value for nearest neighbour cross-talk so obtained (-4.5%) is consistent with the experimental X-ray measurements ($-3 \pm 2\%$). Secondly, theory has been used to give a value to the unknown energy normalization parameter, β. Again good agreement with a previous crude estimate (see p.65) is obtained (i.e. -25% as opposed to -23%).

A further related problem is observed when the equivalent of Figs.4.23 and 4.24 for 25 GeV/c particles are plotted for any other energies, e.g. see Fig.4.26 for 150 GeV/c protons. Here a positive long range correlation is seen. It is not completely understood but it is thought to be due to a rate effect related to the recovery time of the d.c. high voltage levels, i.e. in runs other than the 25 GeV/c run, particle rates were possibly higher, such that the d.c. level did not have time to recover completely between some events, making all the signals lower than average for such cases. This would produce a long range correlation. Since

the time constants associated with the power supplies used are not known, it is difficult to estimate the magnitude of this effect. However some idea of its importance can be obtained from the previous figure (Fig.4.21) showing how the X-ray peak fluctuations follow the mean ionization fluctuations. Deviations from the straight line could possibly be explained by this rate effect as also could variations between runs.

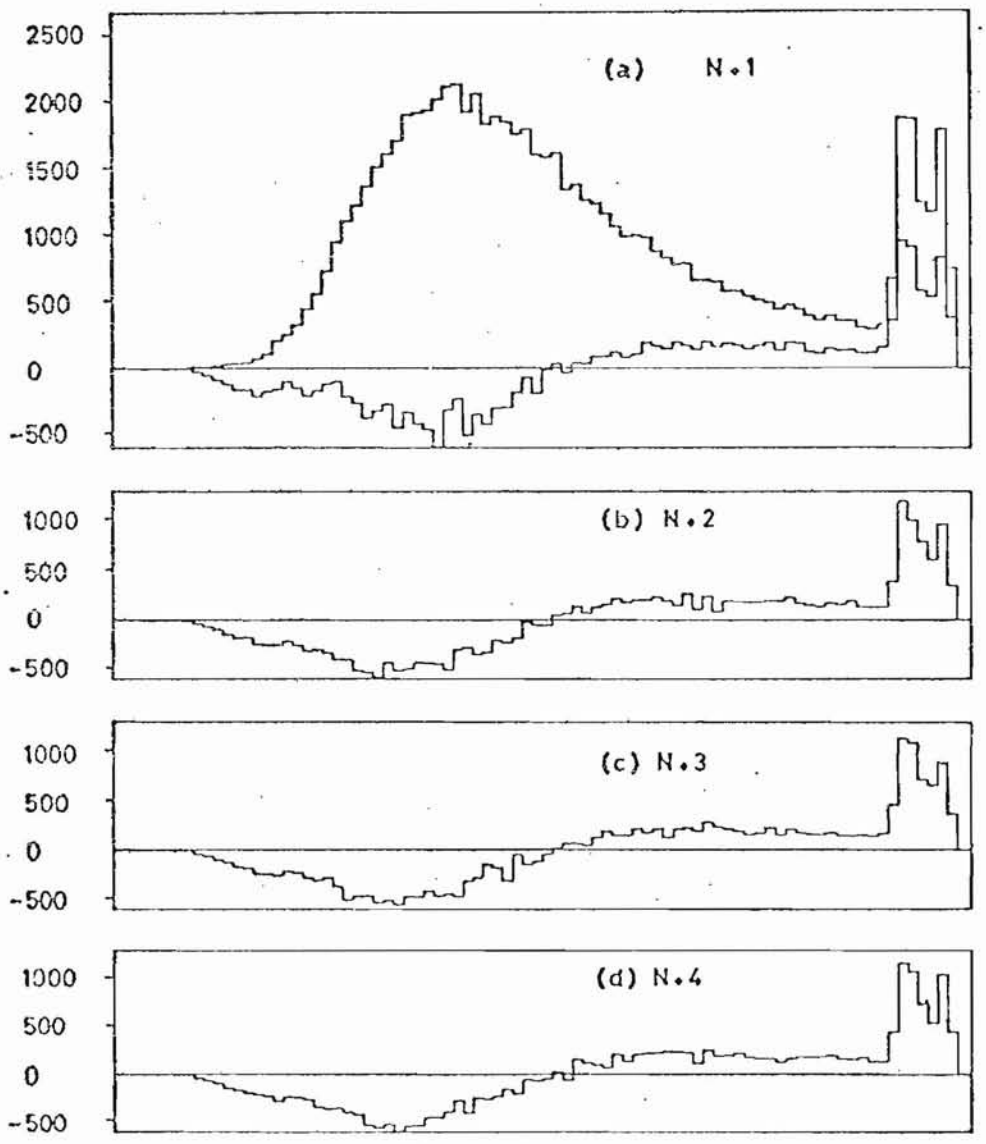

Fig.4.26

IV.7 DISCUSSION AND SUMMARY OF RESULTS OF NAL EXPERIMENT

The Landau distributions of ionization measured for various particles and velocities, calibrated as described in the previous two sections, are shown in Fig.4.27. Curves of energy loss are superimposed which are derived from the theory as outlined in Chapter V. They contain ~ 4.5% nearest neighbour cross-talk and a resolution function with $\sigma = 10\%$ *. The latter has a negligible effect on broad spectra. The fits are good compared with previous theories (see Chapter VI), both in terms of shape and absolute position. The absolute position of course contains one unknown parameter that has been chosen for the best fit to theory but nevertheless one parameter can be chosen to satisfy the Landaus for all different velocities quite well. The errors occurring in ionization loss measurement have been listed in Table 4.6. They are all so small compared with the width of the Landau (typically 100%) that they have little effect on its shape, and so the theoretical and experimental widths agree to $< 2\%$.

The calibrated mean of the lowest 60% distributions for 25 GeV/c protons, pions and electrons are shown in Figs.4.28(a) and (b). The separations seen are of the order of a full width at half maximum for this 58 channel detector. A photograph of 25 GeV/c proton and pion means, is also shown (p.76) which was taken from the on-line display at the time of the experiment and is of uncalibrated raw data. (cf. Fig.4.28(b)). The separation that can be seen in the photograph (p.76) is almost completely due to ionization differences between the two particle types, since gas gain fluctuations etc. have been shown to be relatively unimportant. It is

---

* This is made up of electronic noise and statistical fluctuations in the gas amplification process[29].

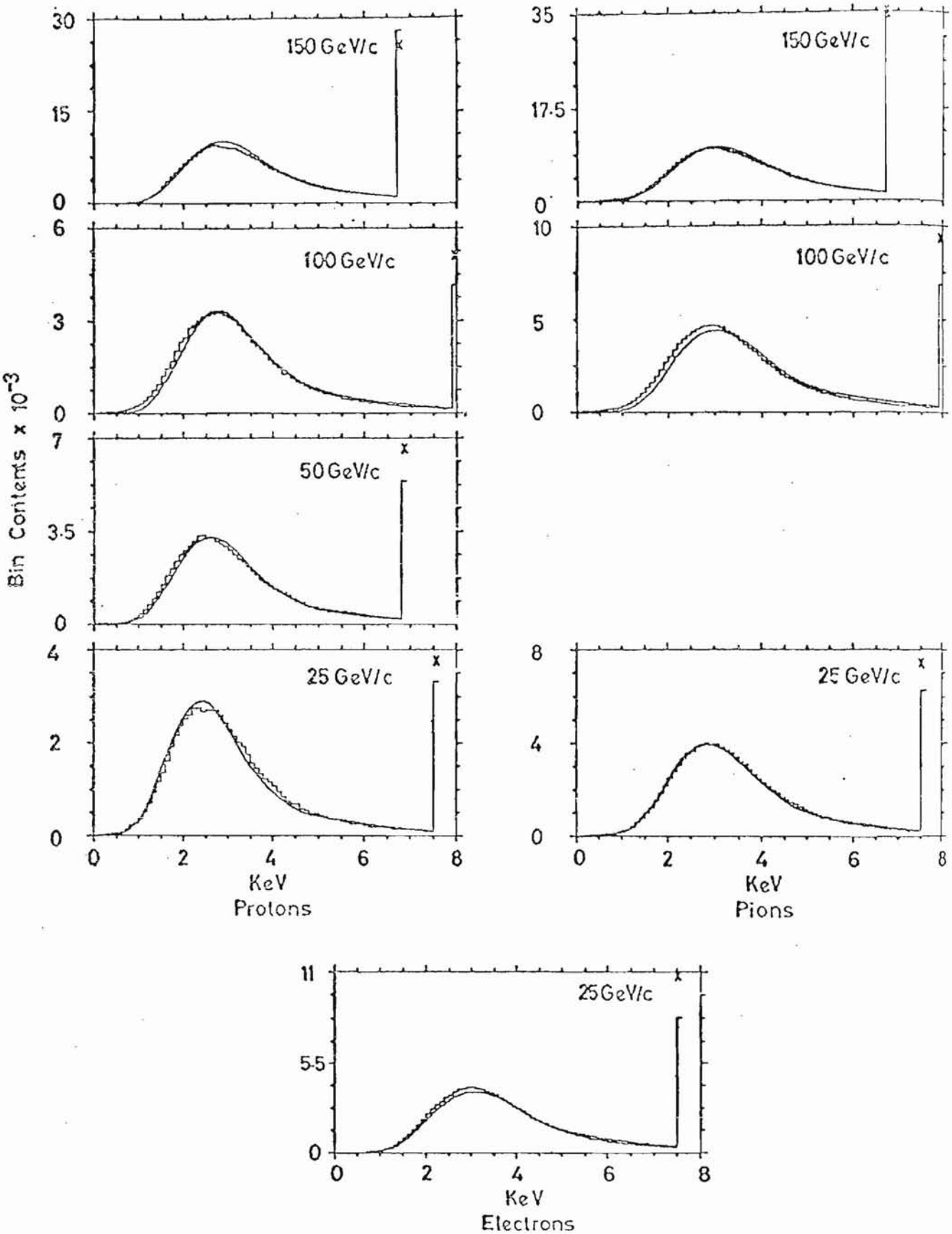

Theory (curve) and Experiment Landau Distributions
(Theory overflows are given by x.)

Fig. 4.27

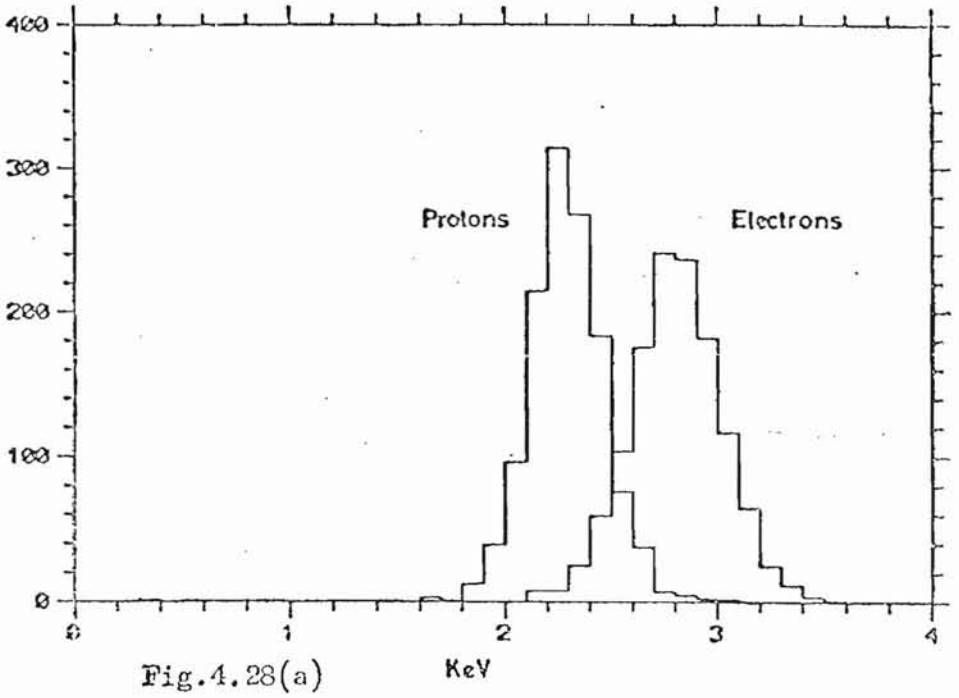

Fig.4.28(a)

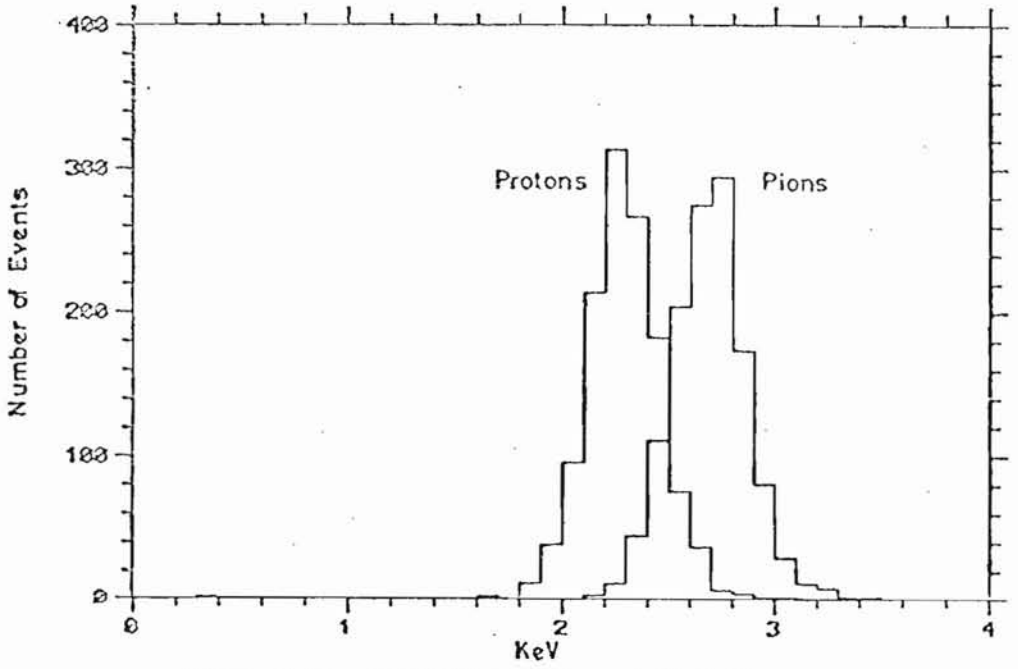

Mean of Lowest 60% Distributions at 25 GeV/c

Fig.4.28(b)

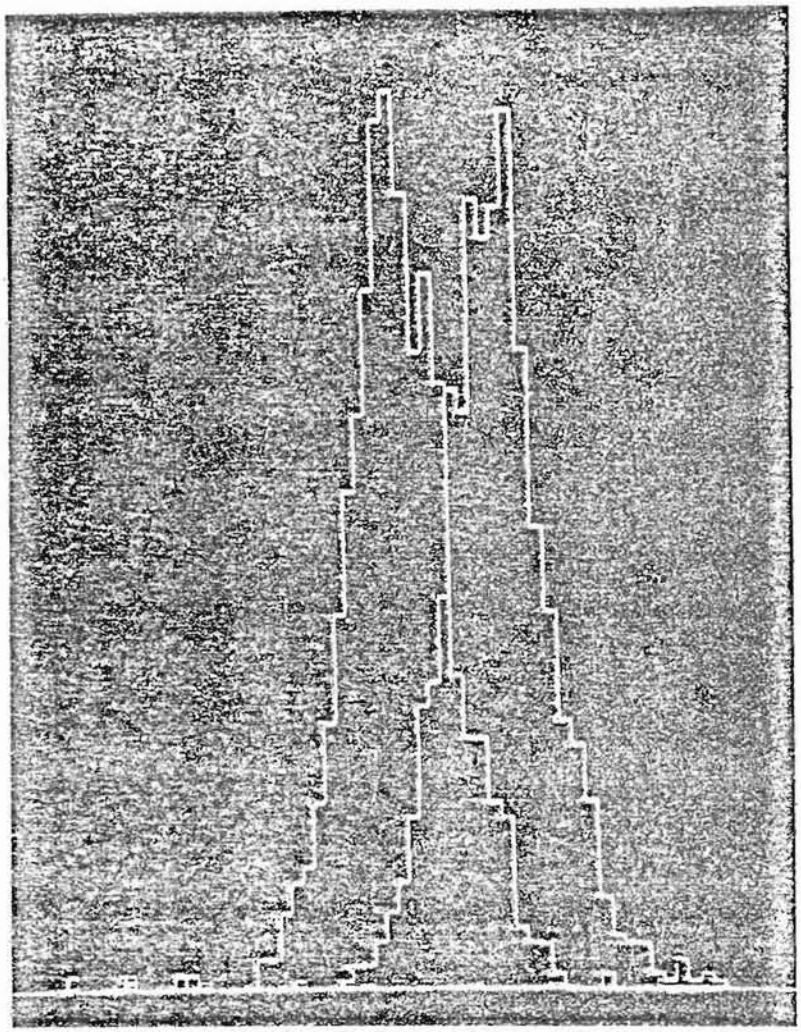

thus a convincing demonstration of how a detector of this form would be able to discriminate between charged particles of different velocities.

Table 4.7 lists the position of the peaks and widths of all the mean of the lowest 60% distributions obtained in the experiment. It also lists the theoretical values derived by Monte-Carlo calculation. It can be seen that the theoretical widths (typically 6%) are less than the experimental widths (typically 8%). This is due mainly to the Landau fluctuations associated with the d.c. level shift, ($\beta = 0.25 \pm 0.05$) which widens the mean distributions. (Most of the errors listed in Table 4.6 are negligible when averages over 60 channels are taken.)

TABLE 4.7

THE MEAN OF THE LOWEST 35 OUT OF 58 × 1.5 cms SAMPLES

Argon + 20% CO_2 at NTP

P/mc	Run	Number of Events	Experimental Distribution Before Shift		Experimental Mean After Shift ($\beta\bar{S}$)	Monte Carlo	
			Mean	FWHM		Mean	FWHM
26.6	Protons at 25 GeV/c	1263	1859	165	2324 ± 116	2211	105
53.3	50 GeV/c	1521	1909	182	2386 ± 119	2414	116
106.6	100 GeV/c	2473	2033	177	2541 ± 127	2582	122
159.4	150 GeV/c	4969	2187	189	2734 ± 137	2652	122
179.1	Pions at 25 GeV/c	1968	2185	172	2729 ± 136	2730	126
716.4	100 GeV/c	2381	2177	190	2721 ± 136	2890	133
1074.4	150 GeV/c	5538	2340	199	2925 ± 146	2912	134
48924	Electrons at 25 GeV/c	2114	2280	212	2850 ± 143	2891	143

All energies in electron volts

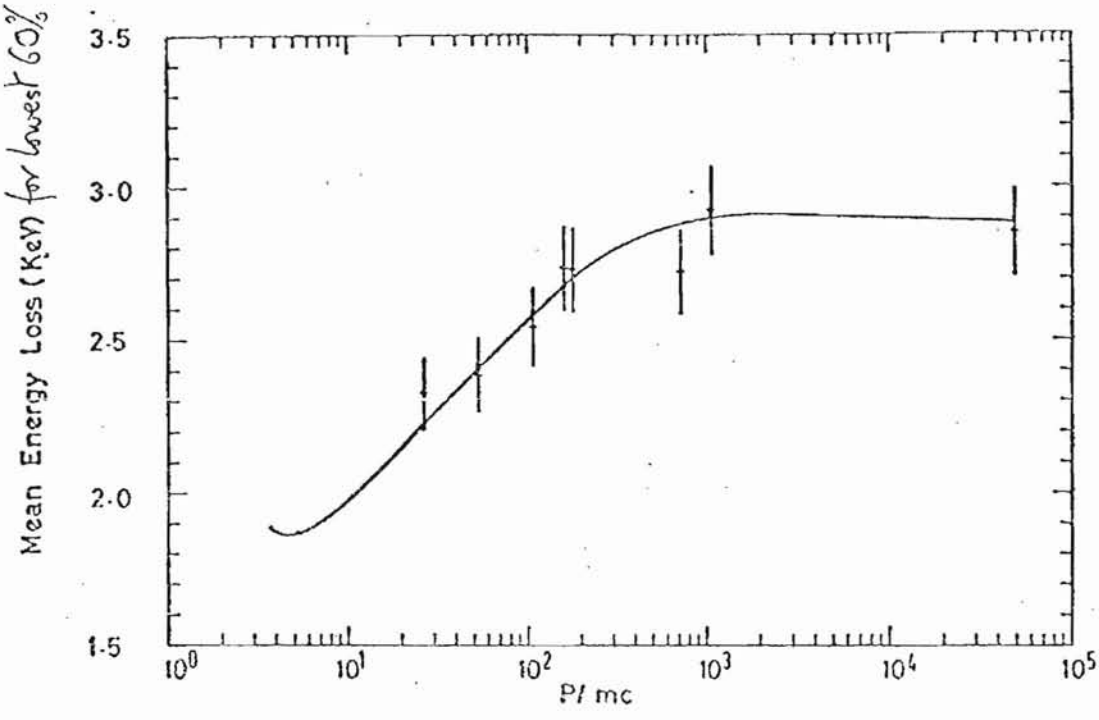

Experimental and Theoretical Mean Ionization Loss vs. P/mc

Fig.4.29

Figure 4.29 shows the experimental and theoretical relativistic rise curves, i.e. a plot of the peaks of the mean of the lowest 60% distributions against particle velocity. The error bars on the experimental points have been taken very conservatively as ± 5%. These are mainly to cover the uncertainty of the relative calibration between runs due to rate effects and gas composition effects and also the uncertainties associated with the d.c. level shift. With these errors theory and experiment are consistent with each other. Although the possibility of some muon contamination of the 25 GeV/c electrons cannot be ruled out, the electron point is compatible with the 150 GeV/c pion point. The relativistic rise is 54 ± 5% and the Fermi plateau extends from $p/m_o c \approx 500$ upwards.

4.8 CONCLUSIONS FROM N A L EXPERIMENT

With the introduction of a single unknown parameter into the calibration of the experimental data, the results of Monte-Carlo calculations of energy loss can be shown to be in good agreement with experimental measurements of ionization deposited in 1.5 $\frac{cm.}{\lambda}$ samples of argon/20% CO_2 at N T P. This holds for charged particle velocities in the range given by $p/m_o c$ = 26 - 50,000.

The resolution of the experiment was limited by instrumental effects which can be avoided in future. Nonetheless on-line separation of pions and protons at 25 GeV/c was obtained and there seems no reason in principle why very much better separation could not be achieved with improved systematics and more samples.

The relativistic rise obtained agrees with results measured by others in gas samples defined by thin windows, (see Chapter VI). This argues against the speculation of Garibyan and Ispirian[22] that the disagreement with calculations is due to the effect of the windows. This experiment shows that the same results are obtained without windows. (See also reference (34) for independent confirmation of this result.)

The results show that the mechanical construction of the chamber and the method of ionization measuring used would not stop one from measuring ionization loss to ±1 or 2 percent assuming the systematic effects that were encountered in this experiment could be eliminated. This is encouraging from the point of view of using this technique as a means of particle identification.

CHAPTER V

THEORETICAL CALCULATIONS OF ENERGY LOSS

V.1 INTRODUCTION

The main problem discussed in this chapter is how to obtain theoretical probability distributions of energy loss for charged particles of various velocities, passing through thin samples of various gases. This chapter first summarizes some ideas and results of the theory of energy loss. Secondly it shows how the theoretical cross sections can be applied, by means of a Monte-Carlo calculation, to obtain predictions of energy loss distributions. Thirdly, some results for various gas compositions, detector resolutions, evaluation of means, etc. are presented.

This work is an extension of work started by Cobb[3]. Some of the results presented here have already been published in a previous paper[35], which also contains further qualitative ideas concerning the interpretation of the theory of energy loss in terms of exchange of virtual photons. A simpler Monte-Carlo approach has also been put forward recently by Ispirian[36].

V.2 SUMMARY OF THE THEORY OF ENERGY LOSS

V.2.1 General Ideas

The theory of energy loss seems to be reasonably well understood. However the application of the theory to explain experimentally obtained probability distributions of ionization loss has not been very successful in the case of thin samples of gas until comparatively recently. (By 'thin' is meant a few cm). The reason for this is due to the fact that certain simplifying assumptions have been made in past calculations which do not hold good for thin samples of gas. To demonstrate this problem the theoretical solution of Landau is described briefly[4].

The required distribution function will be denoted by $f(x, \Delta)$. This is the probability that a particle of given initial energy E_o, on traversing a layer x, will lose an amount of energy lying between Δ and $\Delta + d\Delta$. Let $w(E, \epsilon)$ be the probability (per unit path length) of a single collision giving an energy loss, ϵ, for a particle of energy, E. Considering cases where ionization loss is small compared with E_o, then

$$E \approx E_o \Rightarrow w(E, \epsilon) \approx w(E_o, \epsilon)$$

which will be written as $w(\epsilon)$ in future.

The change of the distribution function $(\partial f/\partial x)\, dx$ in a length dx is equated to the 'collision integral', which expresses the difference between the number of particles that acquire, due to ionization losses along dx, a given energy E, and the number of particles that leave the given energy interval. The following equation is obtained:

$$\frac{\partial f}{\partial x} = \int_0^\infty w(\epsilon) \left[f(x, \Delta - \epsilon) - f(x, \Delta) \right] d\epsilon$$

(The upper limit of integration can be written as ∞ since $f(x, \Delta) = 0$ for $\Delta < 0$ and $w(\epsilon) = 0$ for $\epsilon > E_o$.)

Landau goes on to show how a solution of the above equation can be obtained by applying the Laplace transformation. The result is a general expression for f in terms of an integral over energy loss that contains $w(\epsilon)$. The expression is

$$f(x, \Delta) = \frac{1}{2\pi i} \int_{+i\infty + \sigma}^{-i\infty + \sigma} e^{p\Delta - x \int_0^\infty w(\epsilon)(1 - e^{-p\epsilon})\, d\epsilon}\, dp$$

(see equation 5 of reference (4)).

To proceed further, the function $w(\epsilon)$ must be known. It is at this point that assumptions are made in the Landau solution which cannot be applied to thin samples. Landau takes $w(\epsilon) = \frac{\xi}{x} \cdot \frac{1}{\epsilon^2}$ (Rutherford formula, (6)), which can be shown to be a valid expression to use when the following conditions are satisfied:

$$\xi / \varepsilon_{max} \ll 1 \quad , \quad \xi / \varepsilon_o \gg 1$$

where

$$\xi = \frac{x\, 2\pi N e^4 \rho Z}{m v^2 A}$$

(m = mass of electron, e = electronic charge, v = velocity of incident particle, N = Avagadro's number, ρ = density of medium, Z = atomic number, A = atomic weight). ξ is equal to the energy loss to within a factor of order unity. ε_o is the binding energy of an electron in an atom. ε_{max} is the maximum transferable energy in one collision. The first of these conditions means that the probability of knocking out an electron from an atom with an energy close to ε_{max} is small. The second condition, which is satisfied when typical energy losses are much greater than the binding energy, means that many electrons are created of the order of the binding energy such that their contribution to the fluctuation of ionization losses is negligible.

These conditions are required because they restrict the significant contributions to the integral, in the previous expression for f, to a range of ε in which the expression used for $w(\varepsilon)$ is valid. This range is given by $\varepsilon_o \ll \varepsilon \ll \varepsilon_{max}$. In general the form for $w(\varepsilon)$ when ε approaches ε_o is not known.

For thin absorbers the condition $\xi / \varepsilon_o \gg 1$ is no longer satisfied, which makes the form of $w(\varepsilon)$ when ε approaches ε_o important. Even if $w(\varepsilon)$ is known in this region the solution of the integral becomes difficult and so numerical techniques are resorted to. In principle the integral could be solved numerically but in practice a Monte-Carlo technique was used instead. This should lead to the same results. The Monte-Carlo method attempts to account correctly for energy transfers close to the binding energy. It also accounts for the dielectric properties of the medium. As a penalty, much more detailed knowledge is needed for the

cross sections for the various collision processes that occur. Also the frequency dependence of the dielectric constant of the medium is needed. Fortunately, fairly unreal approximations to these quantities can be taken which will still give good results. This method also eliminates the need for the concept of a 'mean ionization potential' (which is introduced when solving the integral over energy loss in Landau's solution).

To obtain the cross-sections required for the Monte-Carlo calculation the treatment of Fano[37] was followed and is summarised in the next section. However, before this, mention is made of the review article by Crispin and Fowler[38] who show some interesting ways to consider the theory. In particular they show how the energy loss process can be represented by a Feyman diagram with the transfer or propagation of a virtual photon from the incoming particle to an atom, with the resultant emission of an outgoing particle and an ion pair consisting of an electron and a positively charged atom. The single photon exchange is then separated into longitudinal and transverse parts (see page 292 of reference (38) for definition). The two propagators are modified separately to take account of the effect of the medium, by introducing the frequency dependent dielectric constant into Maxwell's equations that describe the 4-vector potential of the incident particle. Also the cross section for absorption of these virtual photons is written as a product of the equivalent cross section for real photons and a form factor. A differential cross section is thus obtained for the energy loss process in the medium. A similar approach is followed below.

Summary of Crispin & Fowler (1st part, anyway)

V.2.2 Fano's Approach

This section is a summary of the parts of Fano's review article[37] relevant to the setting up of the Monte-Carlo program for generation of energy loss distributions. (His notation will be followed exactly. This means a change in notation from the previous section, e.g. $w(\epsilon) \equiv \sigma_n(E_n) \times$ number of collision centres per c.c.)

The cross section for the energy loss of a spinless charged particle in collision with an isolated bound atomic electron is obtained using a Born approximation and can be written as

$$\frac{d\sigma_n}{dQ} = \frac{2\pi z^2 e^4}{mv^2} Z \left\{ \frac{|F_n(q)|^2}{Q^2\left(1+\frac{Q}{2mc^2}\right)^2} + \frac{|\underline{\beta}_t \cdot \underline{G}_n(\underline{q})|^2}{\left[Q\left(1+\frac{Q}{2mc^2}\right) - \frac{E_n^2}{2mc^2}\right]^2} \right\} \left(1 + \frac{Q}{mc^2}\right)$$

where $\underline{q}$ = momentum transfer

$$Q\left(1 + \frac{Q}{2mc^2}\right) = \frac{q^2}{2m}$$

m = mass of the electron

E_n = energy transfer (continuous unless specifically stated others. Note, in the previous section this quantity was ϵ.)

$\underline{\beta}_t$ = component of $\underline{\beta}$ (particle velocity) perpendicular to $\underline{q}$

z = charge of incident charge particle

Z = atomic number

F_n and $\underline{G}_n(q)$ are the form factors for the interaction of the charged particle with a bound atomic electron, and can be described in terms of a longitudinal (Coulomb) interaction and the propagation of transverse virtual photons respectively. They are defined by

$$F_n(\underline{q}) = Z^{-\frac{1}{2}} \sum_j \langle n | \exp(2\pi i\, \underline{q} \cdot \underline{r}_j h) | 0 \rangle ;$$

Parity $|n\rangle$ = Parity $|0\rangle$ for non-zero F,

$$\underline{G}_n(\underline{q}) = Z^{-\frac{1}{2}} \sum_j \langle n | \underline{\alpha}_j \exp(2\pi i\, \underline{q} \cdot \underline{r}_j h) | 0 \rangle ;$$

Parity $|n\rangle$ = − Parity $|0\rangle$ for non-zero G,

where $|n\rangle$ and $|0\rangle$ are the initial and final states of the atom in which the j^{th} electron is being excited. F and $\underline{G}$ are thus matrix elements of operators of the following form.

F: The Fourier integral of the Coulomb interaction is given by

$$\frac{ze^2}{|\underline{r}-\underline{r}_j|} = \frac{ze^2}{2\pi^2}\int d\underline{k}\, k^{-2} \exp\left[i\underline{k}\cdot(\underline{r}_j-\underline{r})\right]$$

each Fourier component representing transfer of momentum $\hbar\underline{k}$.

$\underline{G}$: The absorption of a photon of momentum $\hbar\underline{k}$ is given by

$$e\,c\,\underline{\alpha}_j \cdot \underline{\hat{A}}_s \exp(-i\,\underline{k}\cdot\underline{r}_j)$$

where $e\,c\,\underline{\alpha}_j$ is the relativistic current operator of the j^{th} electron and $\underline{\hat{A}}_s$ is the polarization vector of the photon ($s=1,2$ for two mutually orthogonal directions both at right angles to $\underline{q}$, the momentum transfer). The mechanism of this transverse part of the interaction is electromagnetic in nature and as such, only becomes important when the particle approaches the speed of light.

The transverse, i.e. second, term in the cross section is responsible for the relativistic rise of energy loss as incident particle velocity increases at high energies. Note, because of the parity changes (see expressions for F and $\underline{G}$ above) the longitudinal and transverse terms add incoherently.

The method of Fano is followed fairly closely to obtain, from the above expression for the cross section, an expression for the probability of a particular energy loss (E_n) as a function of E_n and other measurable parameters. Fano divides the cross section up into three intervals of Q, i.e. (i) $Q_{min} \le Q < Q_1$, (ii) $Q_1 \le Q < Q_2$, (iii) $Q_2 \le Q < Q_{max}$. Q_{min} is a function of E_n, the energy loss, and is a kinematic restriction; Q_{max} is also a kinematic restriction, i.e. $Q_{min} \approx E_n^2/2mv^2$; $Q_{max} \approx 2mv^2\gamma^2 = 2mv^2/(1-\frac{v^2}{c^2})$. Q_1 and Q_2 are such that in the region $Q_1 \le Q < Q_2$ the form factor $\underline{G}_n(\underline{q}) \sim 0$. Q_1 and Q_2 are discussed later.

The various approximations and resulting expressions for the cross section are as follows:

(1) Low Q region $(Q_{min} \leq Q < Q_1)$.

Here dipole transitions will predominate so the following approximations can be made:

$$|F_n(\underline{q})|^2 \sim Z^{-1}q^2|(\Sigma_j x_j)_{no}|^2/\hbar^2 = Qf_n/E_n$$

$$|\underline{\beta}_t \cdot \underline{G}_n(\underline{q})|^2 \sim Z^{-1}\beta_t^2 E_n^2|(\Sigma_j y_j)_{no}|^2/\hbar^2c^2 = \beta_t^2 f_n E_n/2mc^2$$

where x_j and y_j are electron coordinates in the directions of $\underline{q}$ and $\underline{\beta}_t$ respectively and f_n is the dipole oscillator strength[39].

For a condensed material Fano shows that, after integrating the expression for $\frac{d\sigma}{dQ}$ (p.84) over Q, the longitudinal component of the cross section can be represented as

$$\sigma_n = 0 \quad \text{for} \quad E_n \neq E_i$$

$$\sigma_n = \sigma_i = \frac{2\pi z^2 e^4}{mv^2} Z \frac{f_i}{E_i} \ln \frac{2mv^2Q_1}{E_i^2} \quad \text{for} \quad E_n = E_i ,$$

where

$i = 1, 2, \ldots,$ number of (atomic) shells

E_i = Binding energy of each shell

f_i = Number of electrons in shell i.

E_i and f_i refer to the 'system' under consideration, the size of which is given by $\sim \hbar/q$ and thus for condensed matter need not necessarily be an individual atom. However, in the Monte-Carlo calculations performed, E_i and f_i are taken as those for an isolated atom unmodified by any bulk effects in the medium, (e.g. there could be effects like upward shifts in the energy levels due to long range Coulomb effects as seen in a crystal lattice). Also we make $Q_1 = E_i$. This will be discussed later

Note, in all previous theories, the cross section used for calculations would not contain individual energy levels, but a 'mean ionization potential' would appear instead.

The transverse component of the cross section in a condensed material is shown to be given by:

$$\frac{d\sigma_n}{dE_n} = \frac{1}{\hbar}\frac{d\sigma_\omega}{d\omega} = \frac{e^2 z^2}{N\pi v^2 \hbar^2}\left\{\frac{\epsilon_2(\omega)}{|\epsilon(\omega)|^2} \ln\left[(1-\beta^2\epsilon_1)^2 + \beta^4\epsilon_2^2\right]^{-\frac{1}{2}} + \left[\beta^2 - \frac{\epsilon_1(\omega)}{|\epsilon(\omega)|^2}\right]\arctan\frac{\beta^2\epsilon_2(\omega)}{1-\beta^2\epsilon_1(\omega)}\right\}$$ *(see footnote)

where

$E_n = \hbar\omega$

N = density of atoms per unit volume

$\epsilon_1(\omega) = \epsilon_1(\omega) + j\,\epsilon_2(\omega)$, is the dielectric constant of the medium and is taken as a sum of Lorentzians, i.e.

$$\epsilon(\omega) = 1 + \alpha(\omega) = 1 + \omega_p^2 \sum_i \frac{f_i}{\frac{E_i^2}{\hbar^2} - \omega^2 - j\gamma_i\omega}$$

where

E_i = binding energy of i^{th} atomic level

f_i = number of electrons in shell i.

γ_i = the 'width' of the effective ionization level.

The somewhat crude approximation to reality involved in writing the transverse cross-section in terms of the Lorentzian form of the dielectric constant leads to problems in the physical interpretation. In the collision processes, atomic electrons are excited from their ground states either to other bound states or to the continuum (i.e. ionization). γ_i must say something about the probability of a particular jump occurring. γ_i has been chosen in the Monte-Carlo calculations performed to be given by $\gamma_i = E_i$.

* See reference (35) for an explanation of how the dielectric constant represents the modification of the transverse virtual photon's range in a medium.

Roughly this assumes that either an electron will be excited to the continuum and will then most likely have a kinetic energy less than E_i, or, an electron will be excited to another bound state which will typically be E_i away from the unbound region.[55] It can be seen that this cross-section includes a part due to excitation processes as well as a part due to ionization. However, often the de-excitation processes associated with an excitation will result in the emission of an Auger electron, hence such an excitation process is effectively an ionization. (Reference will again be made to this particular problem in the discussion following). It should be pointed out that, although the choice of $Y_i = E_i$ cannot be shown to be anything more than vaguely reasonable, the changes to the Landau distributions that are obtained when Y_i is taken as $Y_i = 1\,eV$ or $Y_i = 0.2\,E_i$ are of order 1% (in terms of shape and width).

This transverse term, written in terms of the bulk properties of the medium, leads to the relativistic rise of ionization loss for increasing charged particle velocity and its subsequent curtailing due to the density effect.

(2) Intermediate Q region $(Q_1 \leq Q < Q_2)$

The transverse component is zero for kinematic reasons in this region (see reference (37) p.11). The longitudinal component presents a problem since there is no easy approximation to make for $F_n(q)$. Discussion of this term is deferred until the high Q region is discussed.

(3) High Q region $(Q_2 < Q \leq Q_{max})$

In this region typical energy transfers are much greater than atomic binding energies and so $Q \sim E_n$, therefore the form

factors can be calculated by taking the atomic electrons as free, giving the following cross sections:

$$\frac{d\sigma_n}{dE_n} = \frac{d\sigma_n}{dQ} = \frac{2\pi z^2 e^4}{mv^2} \frac{Z}{E_n} \left[\frac{1}{E_n\left(1 + \frac{E_n}{2mv^2}\right)} \right] \qquad \text{longitudinal component}$$

$$\frac{d\sigma_n}{dE_n} = \frac{d\sigma_n}{dQ} = \frac{2\pi z^2 e^4}{mv^2} \frac{Z}{E_n} \left[\frac{\beta_t^2}{2mc^2} \right] \qquad \text{transverse component}$$

and $\beta_t^2 = \left(1 + \frac{Q}{2mc^2}\right)^{-1} - (1 - \beta^2)$.

[Note the above two cross sections combine to give the familiar Bhaba cross section formula[40].

$$\frac{d\sigma_n}{dE_n} = \frac{2\pi z^2 e^4}{mv^2} Z \frac{1}{E_n^2}\left(1 - \beta^2 \frac{E_n}{E_{max}}\right) \quad \text{where} \quad E_{max} = 2mv^2\gamma^2\Big]$$

In the Monte-Carlo calculation the high Q contribution to the cross section is taken as

$$\frac{d\sigma_n}{dE_n} \approx \frac{2\pi z^2 e^4}{mv^2} Z \frac{1}{E_n^2} \qquad (\underline{cf}\ w(\epsilon)\ \text{on p.81})$$

The high Q transverse term is ignored since in the cases considered (i.e. $E_n \ll E_{max}$) it is negligible

Returning to the question of the intermediate Q region, for the purpose of the Monte Carlo calculation, the approximations are made that $Q_2 = Q_1$ and that

$$\left(\frac{d\sigma}{dQ}\right)_{\substack{\text{long} \\ \text{high Q}}} = \left(\frac{d\sigma}{dQ}\right)_{\substack{\text{long} \\ \text{int. Q}}}$$

i.e. that the atomic electron can be regarded as free in the intermediate Q region as well as the high Q region. This means that at $Q = Q_1$, we go straight from longitudinal low Q approximations (i.e. bound atomic electrons with dipole excitation) to longitudinal high Q approximations (free electrons). This transition is assumed to occur at momentum transfers

whose wavevector corresponds to that of the atomic electron that is being excited, i.e. $Q_{1i} = E_i$. It should be noted that the above crude assumptions for the longitudinal component still satisfy the sum rule: $\int E_n |F_n(\underline{q})|^2 \, dE_n = Q$ (which can be interpreted as the atomic electrons behaving on average, in terms of energy absorbed, as if they were free, regardless of atomic binding.)

V.3 MONTE-CARLO CALCULATIONS

The steps in the Monte-Carlo calculations are as follows:

The cross-sections, whose derivation was summarized in the previous section, are integrated over small energy intervals, ΔE_n. From this, a table is set up which gives the probability for a single collision to produce an energy loss, in the interval $E_n - \frac{\Delta E_n}{2}$ to $E_n + \frac{\Delta E_n}{2}$, versus the mean energy loss of that interval. (This probability table is thus of $w(\varepsilon)$ versus ε, referring to the Landau notation of p.82.) This is summarized mathematically below:

$$\sigma_1 = \int_{E_n-(\Delta E_n/2)}^{E_n+(\Delta E_n/2)} N \frac{d\sigma_n}{dE_n} \, dE_n \,, \quad \text{where}$$

$$\frac{d\sigma_n}{dE_n} = \frac{2\pi z^2 e^4}{m v^2} Z \sum_i \frac{f_i}{E_n} \ln \frac{2m v^2}{E_n} \delta(E_n - E_i) \qquad \text{(low Q longitudinal)}$$

where E_i = binding energy of i^{th} atomic level

$$\sigma_2 = \int_{E_n-(\Delta E_n/2)}^{E_n+(\Delta E_n/2)} N \frac{d\sigma_n}{dE_n} \, dE_n \,, \quad \text{where}$$

$$\frac{d\sigma_n}{dE_n} = \frac{1}{\hbar} \frac{d\sigma}{d\omega} = \frac{e^2 z^2}{N\pi v^2 \hbar^2} \left\{ \frac{\epsilon_2(\omega)}{|\epsilon(\omega)|^2} \ln \left[(1-\beta^2\epsilon_1)^2 + \beta^4 \epsilon_1)^2 + \beta^4 \epsilon_2^2 \right]^{-\frac{1}{2}} + \frac{\epsilon_1(\omega)}{|\epsilon(\omega)|^2} \arctan \frac{\beta^2 \epsilon_2(\omega)}{1-\beta^2 \epsilon_1(\omega)} \right\}$$

where $\underline{\epsilon}(\omega) = 1 + \omega_p^2 \sum_i \frac{f_i}{\frac{E_i^2}{\hbar^2} - \omega^2 - j\gamma_i \omega}$ (low Q transverse)

$$\sigma_3 = \int_{E_n-(\Delta E_n/2)}^{E_n+(\Delta E_n/2)} N \frac{d\sigma}{dE} \, dE \,, \quad \text{where}$$

$$\frac{d\sigma_n}{dE_n} = \frac{2\pi z^2 e^4}{m v^2} Z \frac{1}{E_n^2} \qquad \text{(High Q longitudinal)}$$

for $E_n \geq E_i$.

The differential cross sections giving σ_2 and σ_3, as used in the calculation for Argon/20% CO_2, are shown in Figs.5.1 and 5.2. The cross sections for a variety of different particle velocities are shown and for the transverse cross section the difference giving the relativistic rise is seen. The longitudinal cross section shows very little change with particle velocity. Peaks for these cross sections occur at the atomic binding energies.

Cross section σ_1 is a series of spikes at the atomic binding energies. This is a crude approximation to reality, but as stated earlier it at least satisfies the sum rule and hence the associated physical consequences.

Before proceeding, a possible error in the treatment should be pointed out here. As can be seen in Fig.5.1, the lowest energy loss per collision was taken as 1 eV. For Argon/CO_2 the lowest binding energy is 17.7 eV, thus an energy loss of 1 eV cannot lead to ionization which is the quantity measured. Changing the minimum energy loss to 17.7 eV systematically, shifts the relativistic rise curve down by 0.9%. The results following contain this error, but considering the crudity of the method, the theoretical results are probably not accurate at the 1% level anyway.

The above cross sections lead to the table of probability versus energy loss for a single collision which is shown pictorially in Fig.5.3 for 25 GeV protons in the energy loss range 1-500 eV. (There are a few events above 500 eV not shown.) These figures show the energy intervals taken for the table, each interval corresponding to one bin in the figures (i.e. their size increases with energy loss). Similar distributions are shown for 25 GeV electrons in Fig.5.4. Superimposed (in dots) is the transverse component of the proton distribution from the previous figure. The

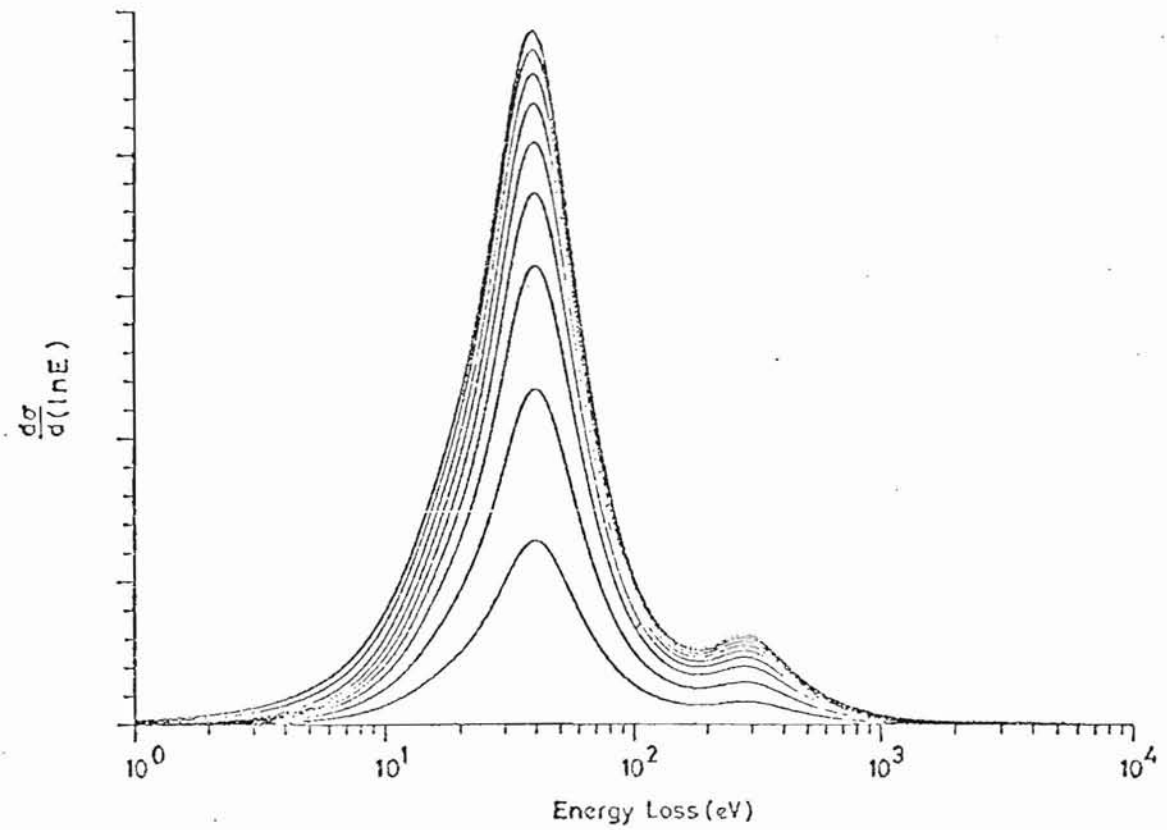

Transverse $\frac{d\sigma}{dE}$ as a Function of Energy Loss from Lowest Peak upwards p/m_0c = 4, 10, 20, 30, 40, 50, 60, 70, 80

Fig. 5.1

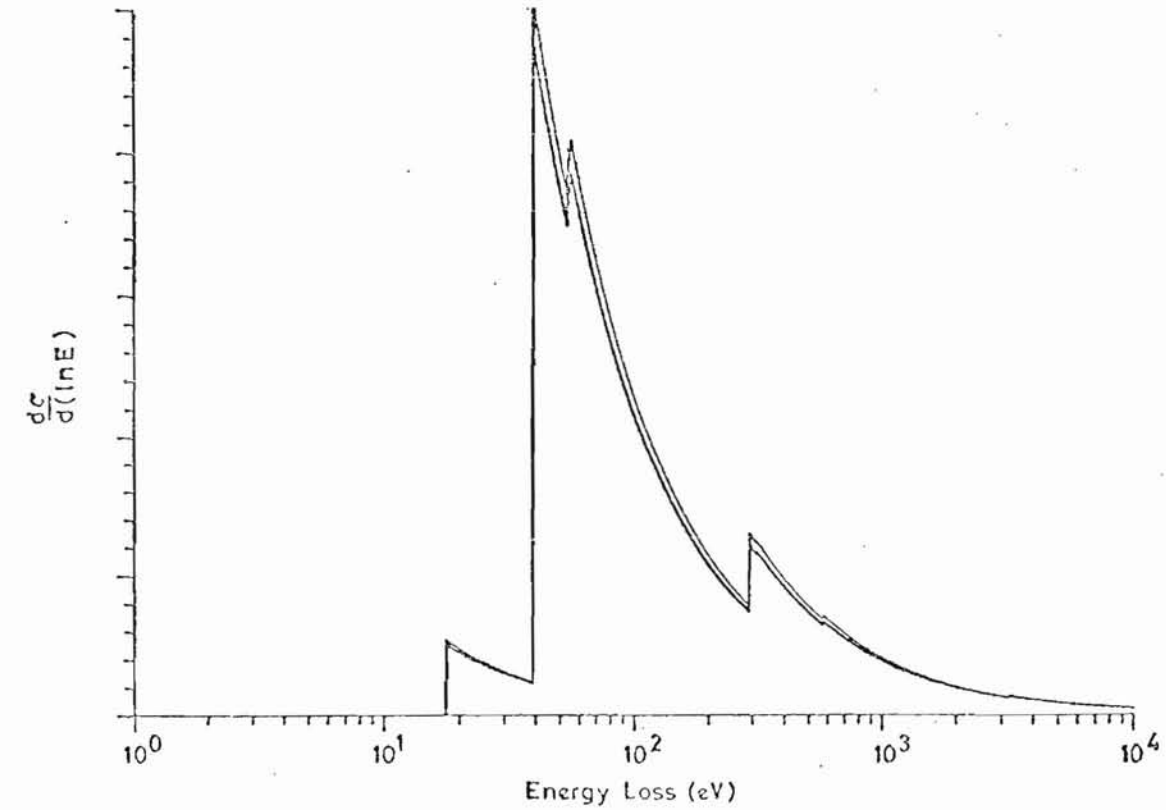

Longitudinal $\frac{d\sigma}{dE}$ as a function of energy loss .

Upper curve is for p/mc = 4 and lower curve for p/mc = 50000

Fig 5.2

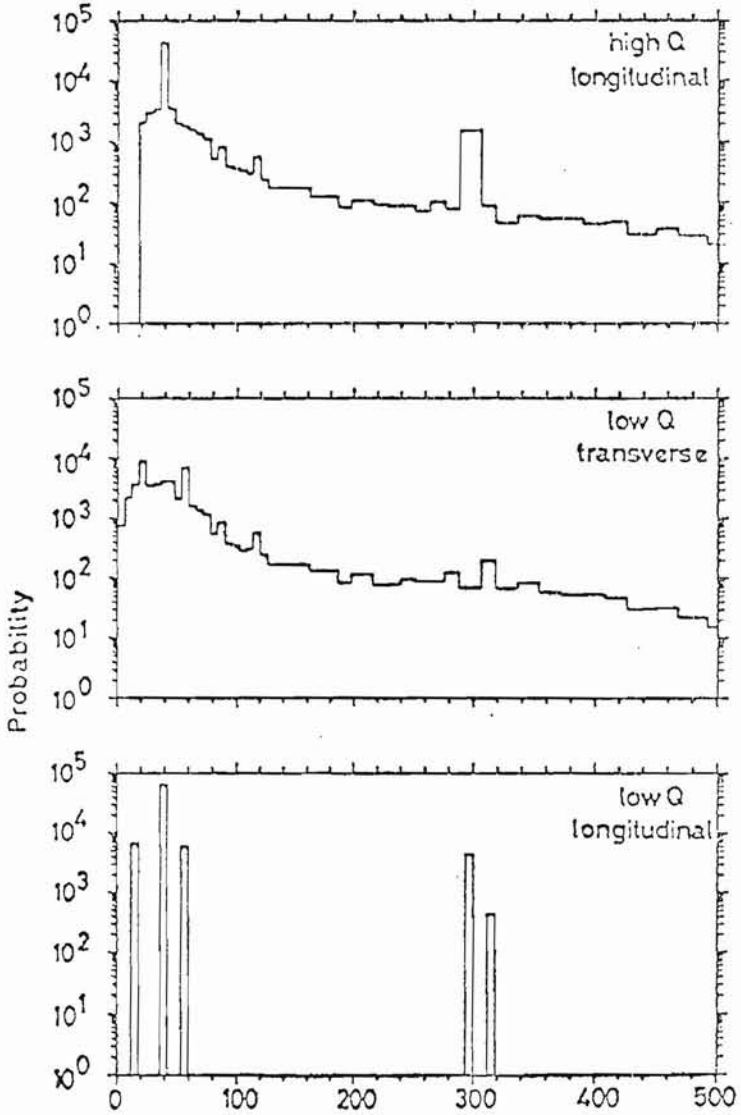

Fig.5.3 Components of Probability Table
25 GeV/c Protons

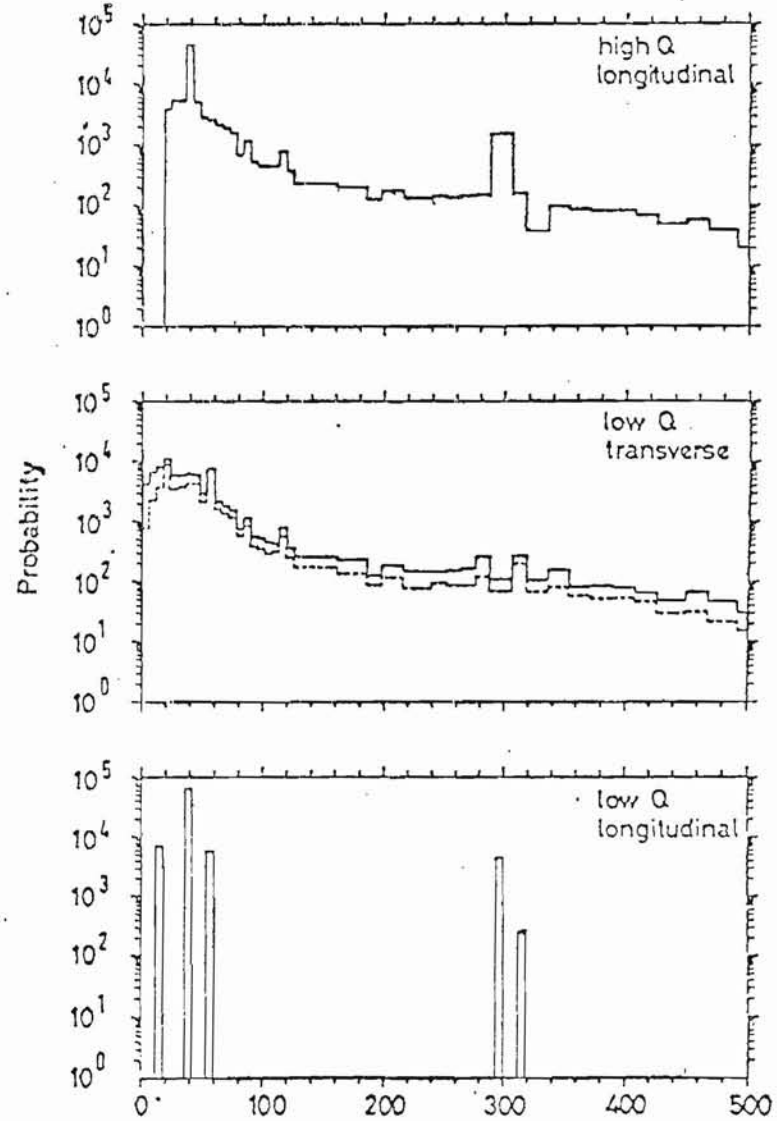

Fig 5.4 Energy Loss per Collision(eV)
Components of Probability Table
25 GeV/c Electrons

components give no detectable change.) From this it should be clear that, in choosing a gas that will show the greatest relativistic rise, the relative magnitude of the transverse to longitudinal terms is as important a consideration as the changes of transverse cross-section with velocity. Both these considerations depend on the plasma frequency and energy levels of the gas.

It should be emphasized that in Figs.5.3 and 5.4, most of the collisions are M shell ionizations of Argon atoms (39.5 eV), which is not so obvious from these figures because they are plotted on log scales.

It would be interesting to compare the cross sections derived here with experimental measurements. However the author has not yet succeeded in finding any data suitable for comparison. This is because experimental measurements seem only to have been made for incident particle energies which are very low (e.g. 500 eV). Also these experiments have measured differential cross sections at particular angles where attention was given to collision processes resulting in excitation, not necessarily ionization, of the atom.

The probability tables, as shown in Figs.5.3 and 5.4, are used to generate probability distributions of energy loss by computer simulating the passage of a charged particle through a sample of gas. The amount of energy loss for each collision that the charged particle makes is obtained from the probability table using a standard Monte-Carlo technique. The total energy loss from all the collisions that the particle makes is thus obtained. This process is repeated for very many charged particle traversals through the sample and so a probability distribution is built up.

To use the distributions obtained by the above method to make theoretical predictions, the following underlying assumption must be pointed out. The theory gives an <u>energy loss</u> distribution whereas most experiments

measure ionization deposited in a medium. It is assumed in all the following comparisons with experiment, that W, the energy lost by an ionizing particle per ion pair created is, on average, a constant for all incident particle energies for a given material. (For gases this energy is always around 30 eV and is about twice the first ionization potential.) It has been shown for a limited energy range that, for noble gases, W appears to be energy independent to better than 1%, but for molecular gases this is only true to within 6%[41]. With this assumption of the constancy of W, then for an experiment such as the one outlined in Chapter IV, comparisons between theoretical energy loss and the experimental ionization loss distributions can be made. This is because the ionization detector is calibrated using an X-ray source with a known energy loss. Thus subsequent ionization measurements are calibrated in terms of the energy absorbed as ionization by the detector from this X-ray of known energy, (assuming no loss of ionization from the boundaries of the detector etc.[42]).

As the Monte-Carlo calculation has been described so far, the only comparisons that can be made with experiment are in terms of the shape and position of the probability distribution. To make the theory give predictions about multi-sampling problems, (e.g. see the multi-sample detector of Chapter IV), a further Monte-Carlo program was used. This simulated the passage of a charged particle through many samples of gas. From this it could determine the 'mean' ionization for one charged particle as measured by the many samples, and hence for many traversals, a mean distribution could be built up. (The definition of 'mean' is discussed in the next section.) This Monte-Carlo program had as its input, the probability distribution of the first Monte-Carlo program.

The Monte-Carlo theory has been applied in the following four ways:

(a) To investigate velocity resolution as a function of various detector parameters and 'mean' ionization estimators. This is related directly to practical application.

(b) To compare the ionization properties of different gases. This is motivated more by theoretical interest since some of the gases are impractical.

(c) To obtain a value for the unknown parameter, β, in the NAL experiment, as outlined in section IV.5. It will not be described further in this section.

(d) To compare theory with experiment in as many cases as possible. See Chapter VI.

V.3.1 Velocity Resolution of a Multi-Sample Ionization Detector

The difference between the distribution of ionization measurements of charged particles at various different velocities, decide the velocity resolution of the detector.

The velocity resolution of a multi-sample ionization detector is dependent on the definition of the 'mean' of the many measurements obtained when a particle passes through it. The qualitative reason for this can be seen in Fig.1.1, which shows the Landau distributions of 25 GeV p's and e's. At the high energy end of the spectrum the difference between the two distributions decreases with increasing energy loss. Thus this tail contains little information and only serves to degrade the variance of the mean of the smaller, more probable measurements. Therefore, for the Landau distribution of output pulses obtained for each charged particle traversal, a fixed fraction of the largest measurements is discarded, and the mean of the remainder is determined. (See reference (43) for other definitions of 'mean' ionization loss - it is shown that this method of estimation is almost as good as a maximum likelihood method.)

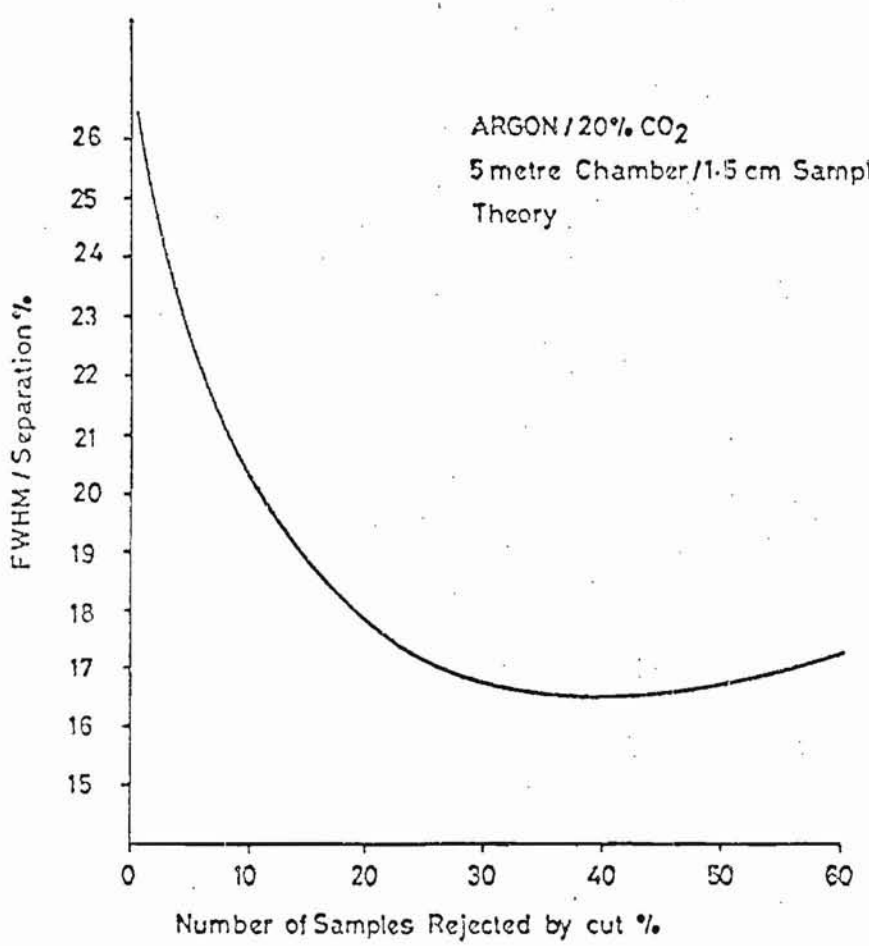

Fig. 5.5

Resolution as a function of cut on mean

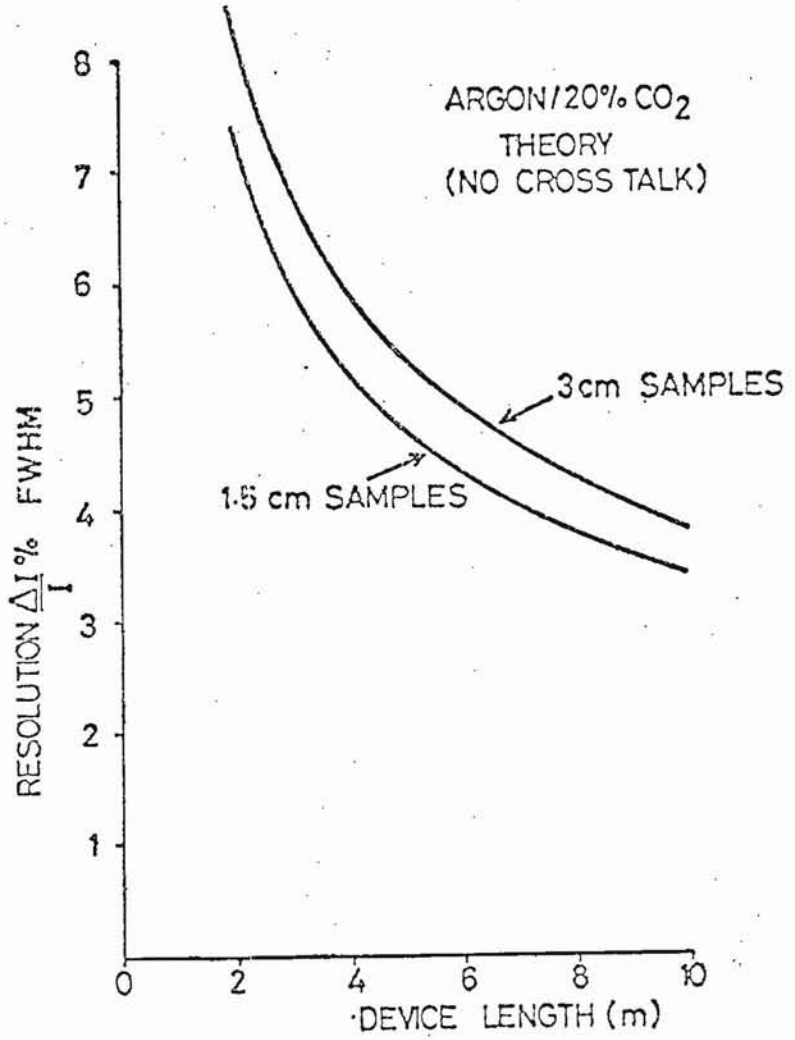

Fig. 5.6

Fig.5.5 shows how resolution varies as a function of this cut. (The resolution in this figure is taken as the spread (FWHM) of the mean ionization measurement divided by the separation of the means, of 25 GeV p's and e's, i.e.

$$\text{resolution} = \frac{\frac{(\Delta I_1 - \Delta I_2}{2}}{I_1 - I_2}$$

where $\Delta I_1 \approx \Delta I_2$.)

As can be seen this quantity is a minimum when the largest 40% of the measurements are rejected. This then was the cut imposed on all experimental and theoretical data.

Figure 5.6 shows how the resolution varies as a function of number of samples and device length. Typically a 5 m device with 1.5 cm samples is comparable to a 7 m device with 3 cm samples. So to get equivalent resolution with a smaller number of channels the device length must be increased, reducing angular acceptance.

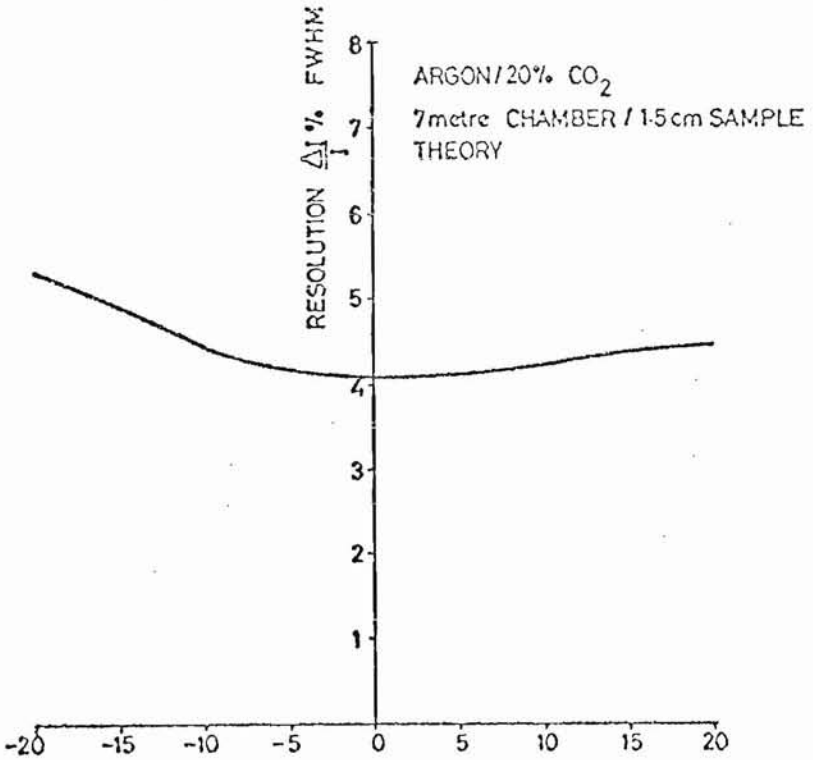

Fig.5.7

Figure 5.7 shows how the resolution is affected if, as is the case in practice, cross talk between adjacent samples is present, i.e. each ionization measurement is dependent to some extent on the adjacent neighbours. It can be seen that the effect is fairly small. (In the NAL experiment analysed previously, this effect was - 4.5%.) The most obvious causes of cross talk in ionization chambers with drift regions (as in the NAL chamber) are as follows:

(a) Capacitative cross talk due to the stray capacitance between signal wires. (Negative, i.e. larger signal on one channel makes the signal smaller on adjacent channel.)

(b) Δ-ray cross talk due to a fast electron from the primary ionization producing secondary ionization in its own sample and then travelling through into a neighbouring sample[32], (Positive).

(c) Diffusion cross talk, due to the diffusion of some electrons produced in the ionization process, diffusing towards other signal wires instead of drifting to the signal wire of their own sample[25] (Positive).

Figure 5.8 shows the response (i.e. mean of lowest 60%) expected from a 5 m ionization detector made up of 330 × 1.5 cm samples of argon, and exposed to a mixture of pions, kaons and protons at 25 GeV/c in the ratio 10:1:1.

Figure 5.9 shows the same at 60 GeV/c and now the separation is marginal. An optimum cut between kaons and pions would result in a loss of about 10% of kaons into the pion peak and the same number of pions misidentified as kaons. In order to make a definitive comparison between different gases, a calculation has been made to find at which momentum the kaon/pion separation is 90% pure in the above sense, see Table 5.1.

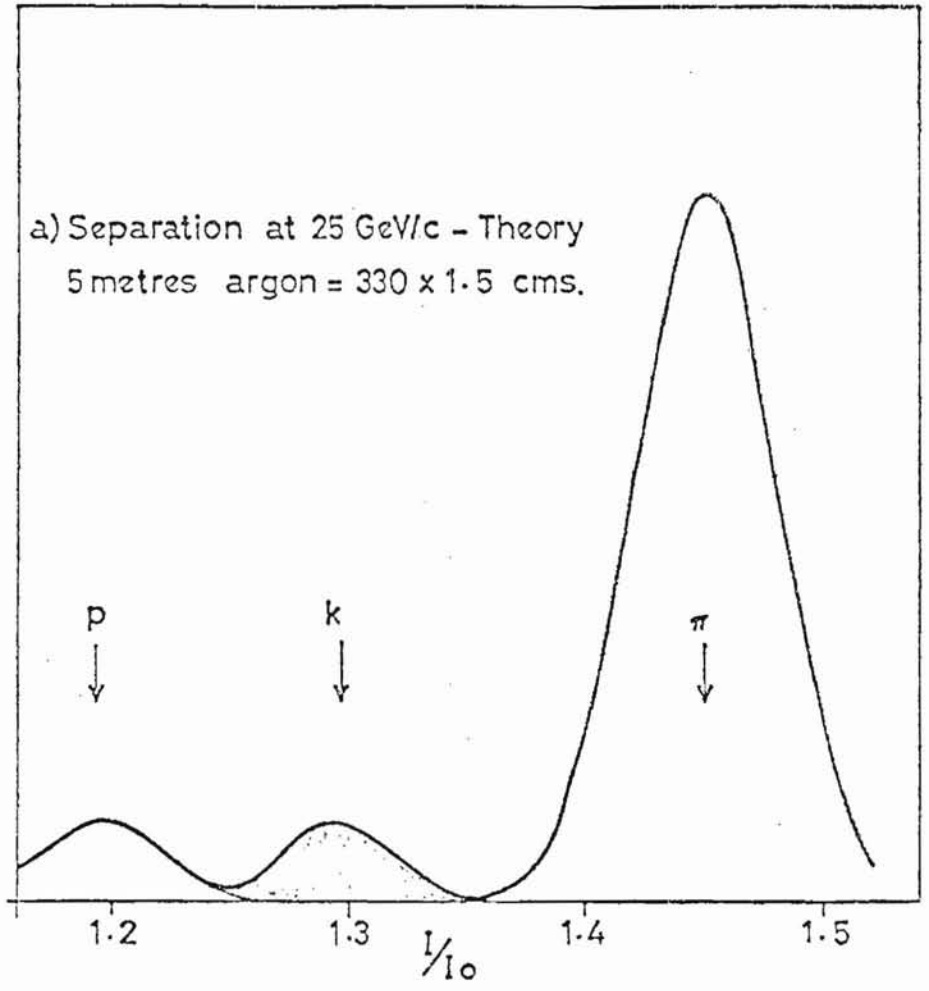
a) Separation at 25 GeV/c - Theory
5 metres argon = 330 x 1·5 cms.
p
k
π
1·2
1·3
1·4
1·5
I/Io

Fig. 5.8

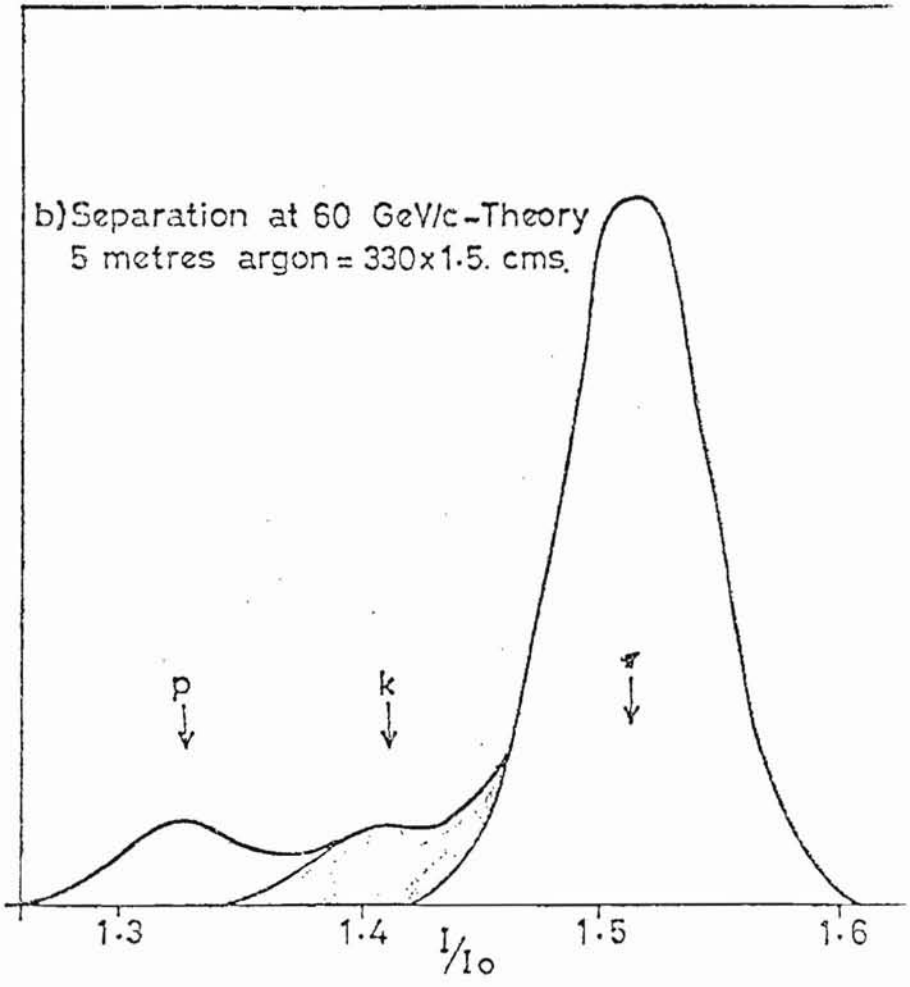
b) Separation at 60 GeV/c - Theory
5 metres argon = 330x1·5. cms.
p
k
π
1·3
1·4
1·5
1·6
I/Io

Fig. 5.9

V.3.2 Comparison of Ionization Properties of Different Gases

The Monte-Carlo programs have been run for a wide range of different gases and incident charged particle velocities. The parameters varied were as follows: (i) atomic energy levels; (ii) number of electrons in each level; (iii) electron density, written in terms of plasma frequency $\left(\omega_p^2 = \frac{Ne^2}{4\pi^2 \epsilon_o m}\right)$; (iv) relative concentrations, in the case of gas mixtures. The value taken for these various parameters are listed in Table 5.2.

The following effects due to variation of these parameters must be considered:

(a) The total number of collisions per unit thickness of gas increases for all parts (i.e. longitudinal and transverse) of the cross-section with increasing plasma frequency, i.e. electron density.

(b) The change in the transverse cross-section with particle velocity, producing the relativistic rise, saturates earlier as plasma frequency is increased. (Due to density effect saturating the range of the transverse virtual photon).

(c) The relative change in the transverse cross-section with particle velocity increases as atomic binding energies increase.

(d) For a given mean energy loss in the medium, the resolution is better when the atomic binding energies are smaller due to the increased statistics of small energy loss collisions.

The results of the various runs made are given in Table 5.1 and are shown in the following figures. (All gases at NTP. Note in Figs.5.10 to 5.13 the ionization, I, refers to the mean ionization of the lowest 60%.)

Figure 5.10, for the noble gases, shows that the relativistic rise increases with increasing atomic number. This is because the mean binding energy is increasing faster than the plasma frequency, (i.e. effect (c) dominates effect (b) in previous list).

TABLE 5.1

CALCULATIONS OF $^{dE}/_{dx}$ for 1.5 cms OF GAS AT NTP

	Truncated mean ionisation loss (eV)					Resolution of mean (FWHM)		Relativistic Rise	K/π limit GeV/c	Most probable ionisation loss (eV)					Relativistic Rise
$P/_{mc}$	4	32	128	512	$5x10^4$	4	5.10^4			4	32	128	512	$5x10^4$	
RARE:															
Helium	254	298	342	358	359	5.2%	4.9%	1.41	45	275	325	372	389	390	1.42
Neon	1115	1359	1583	1696	1714	5.4%	5.1%	1.54	50	1117	1380	1616	1724	1760	1.58
Argon	1961	2408	2783	2995	3095	5.3%	4.8%	1.58	55	2062	2495	2891	3103	3168	1.54
Krypton	3886	4788	5546	5978	6199	5.2%	4.7%	1.60	55	3921	4905	5699	6156	6365	1.62
Xenon	5323	6655	7734	8581	9025	5.5%	5.0%	1.70	95	5339	6704	7878	8726	9242	1.73
FIRST PERIOD:															
Methane	1417	1685	1851	1918	1922	3.9%	3.9%	1.36	30	1459	1744	1916	1988	1992	1.37
Ammonia	1356	1615	1797	1876	1889	4.2%	4.1%	1.39	45	1390	1664	1855	1936	1970	1.42
Neon	1115	1359	1583	1696	1714	5.4%	5.1%	1.54	50	1117	1380	1616	1724	1760	1.58
Nitrogen	1778	2154	2452	2568	2636	4.6%	4.1%	1.48	45	1858	2255	2570	2703	2743	1.48
MIXTURES:															
Argon	1961	2408	2783	2995	3095	5.3%	4.8%	1.58	55	2062	2495	2891	3103	3168	1.54
Argon/20% Co_2	2152	2633	3022	3227	3325	4.9%	4.5%	1.55	55	2244	2713	3096	3363	3404	1.52
Carbondioxide	2915	3523	3969	4167	4226	3.9%	3.7%	1.45	50	3014	3668	4110	4354	4394	1.46
	Number of Collisions/metre														
PRIMARY IONISATION:															
Argon/20% Co_2	2457	2915	3370	3486	3497	2.1%	1.8%	1.42	65						
He/50% Ne	1050	1242	1442	1544	1545	3.3%	2.6%	1.47	85						

For both dE/dx and primary ionisation the quoted resolutions and separations refer to a 5 metre track length.

TABLE 5.2

ATOMIC DATA USED IN CALCULATIONS

	Helium	Neon	Argon	Krypton	Xenon	Methane	Ammonia	Nitrogen	Carbon Dioxide
Plasma energy	0.272	0.609	0.816	1.156	1.414	0.609	0.609	0.721	0.902
Binding energies (eV) and electrons per molecule	24.5(2)	870 (2) 54.4(8)	3196 (2) 294 (8) 39.5(8)	14280 (2) 1754 (8) 152 (18) 39.4(8)	34612 (2) 5073 (8) 831 (18) 169 (18) 25.8(8)	313 (2) 55.8(2) 17.7(2) 13.6(4)	412 (2) 47.6(2) 31.3(3) 13.6(3)	412 (4) 47.6(4) 31.3(6)	313 (2) 55.8(2) 17.7(2) 575 (4) 54.4(4) 39.4(8)

Argon/20% Co_2 Plasma energy = 0.834eV

He/50% Ne Plasma energy = 0.472eV

Atomic data from Sternheimer (1952) Ref. 44 Chemical effects neglected.

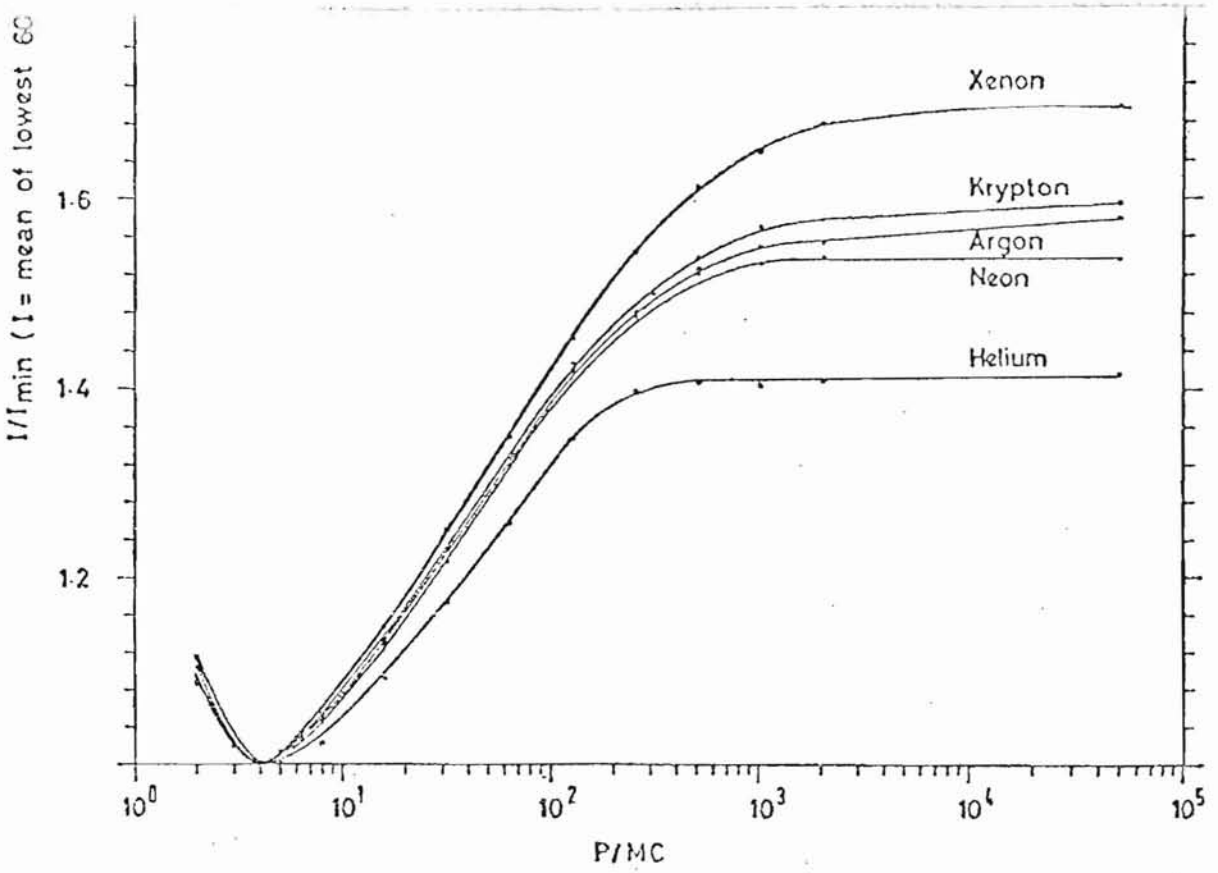

Theoretical relativistic rise curves (noble gases)

Fig.5.10

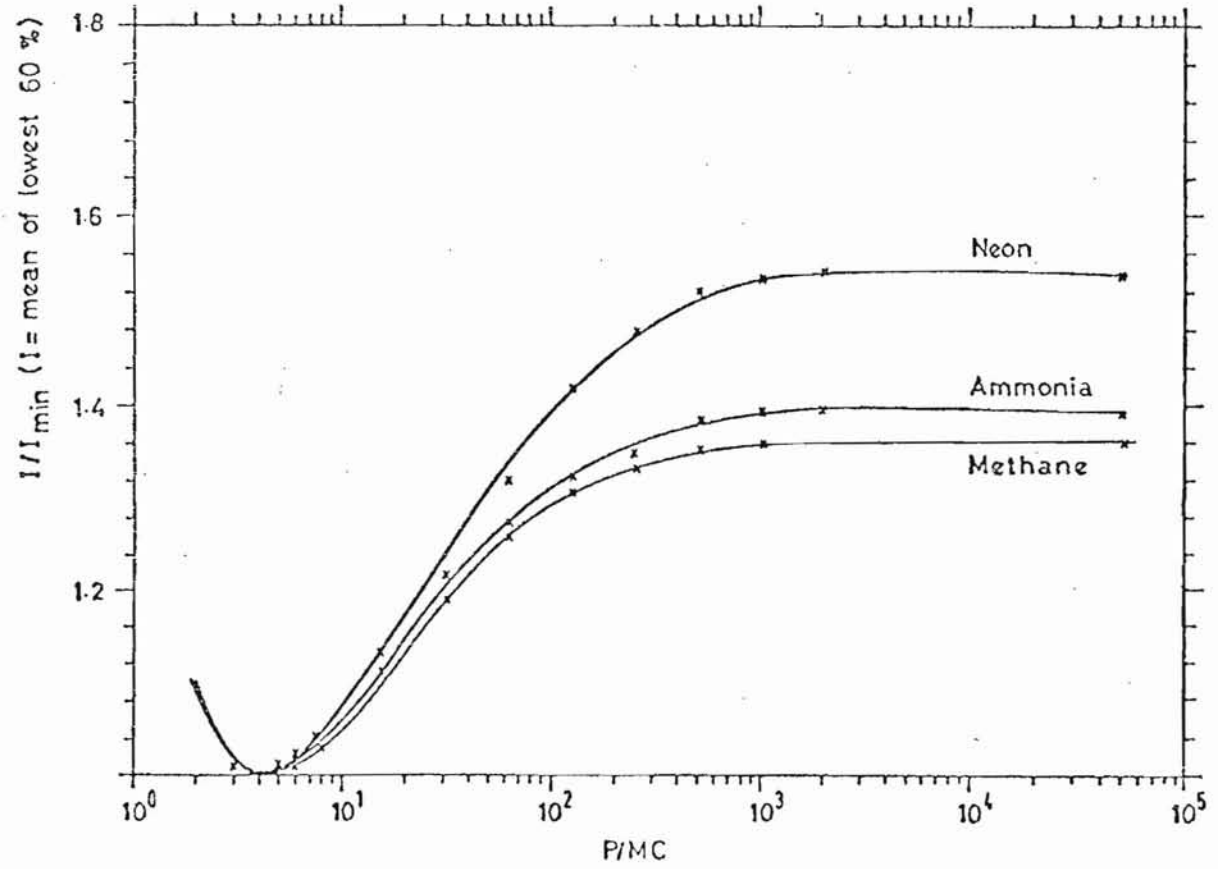

Theoretical relativistic rise curves (first period)

Fig.5.11

Table 5.1 shows that the velocity resolution is approximately constant at $\sim 5\%$ for all the noble gases. This is because for gases of increasing Z the statistics of the collision process (Poisson) improve (in terms of the percent variance of the number of collisions) but the most likely energy loss per collision is greater. These two effects tend to cancel each other out, leaving the percent variance of the mean ionization loss constant.

Figure 5.11 shows the effect of increasing binding energy while keeping plasma frequency constant. (CH_4, NH_3 and Ne have equal numbers of electrons/molecule.) The relativistic rise increases with increasing binding energy. The total probability of a collision process goes down, which results in a decrease of mean energy loss and a slight worsening of the velocity resolution (Table 5.1).

Figure 5.12 shows the small effect that the addition of 20% (by volume) of carbon dioxide has on the relativistic rise of argon. (CO_2 acts as a cooling gas to reduce electron diffusion in drift chambers).

Figure 5.13 compares primary ionization measurements (i.e. number of collisions) with energy loss measurements. The relativistic rise is smaller for a number of collisions due to the equal weighting of large and small energy loss collisions. But on the other hand the velocity resolution (Table 5.1) is very much better. Fig.5.14 shows the probability distributions for 25 GeV protons, pions and electrons, in terms of number of collisions (cf Fig.1.1, which is the same distribution in terms of energy loss). It shows how much easier it would be to obtain a desired velocity resolution using a technique that measured number of collisions. There are practical difficulties though. A streamer chamber[45] is the only suitable device that is available at present for measuring primary ionization and this is no good for accurate measurements because a count of streamers cannot be made with high enough resolution.

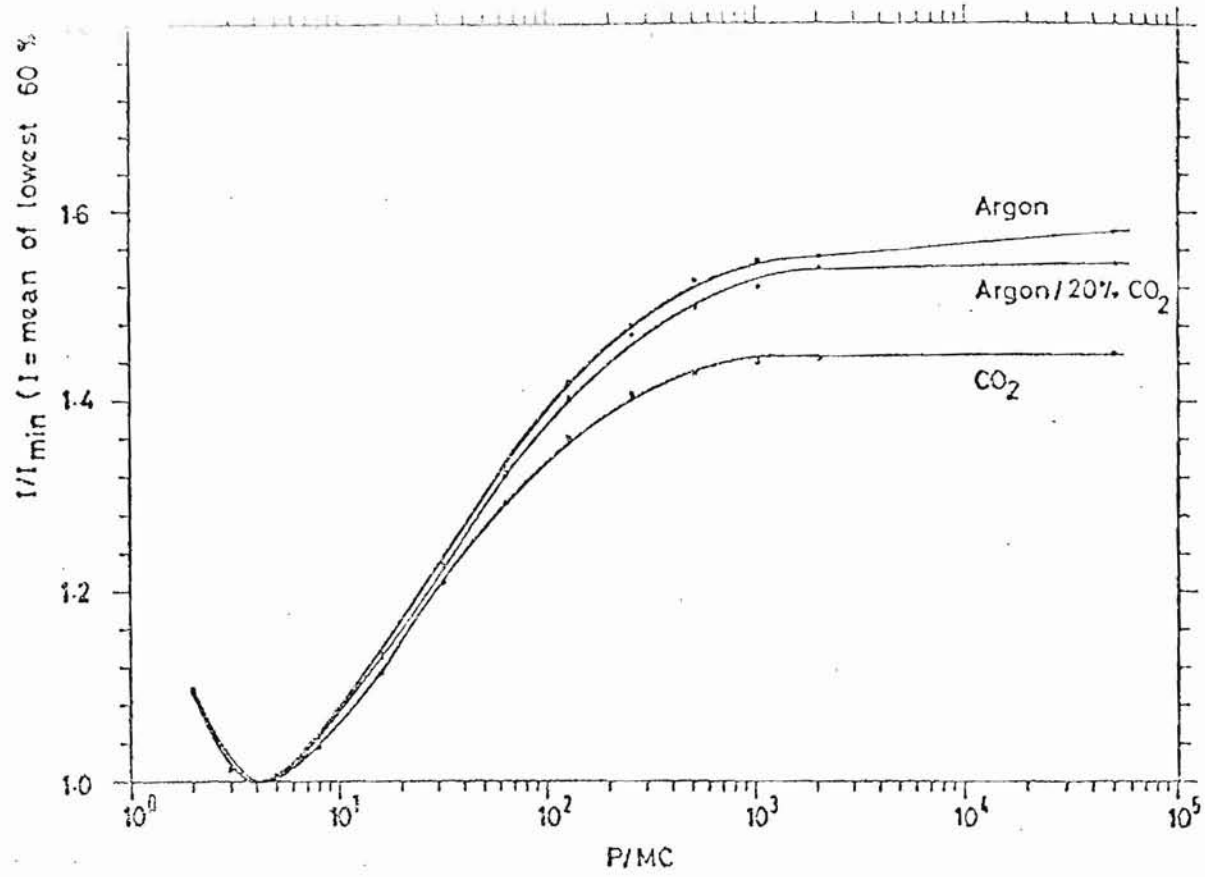

Theoretical relativistic rise curves (mixtures)
Fig. 5.12

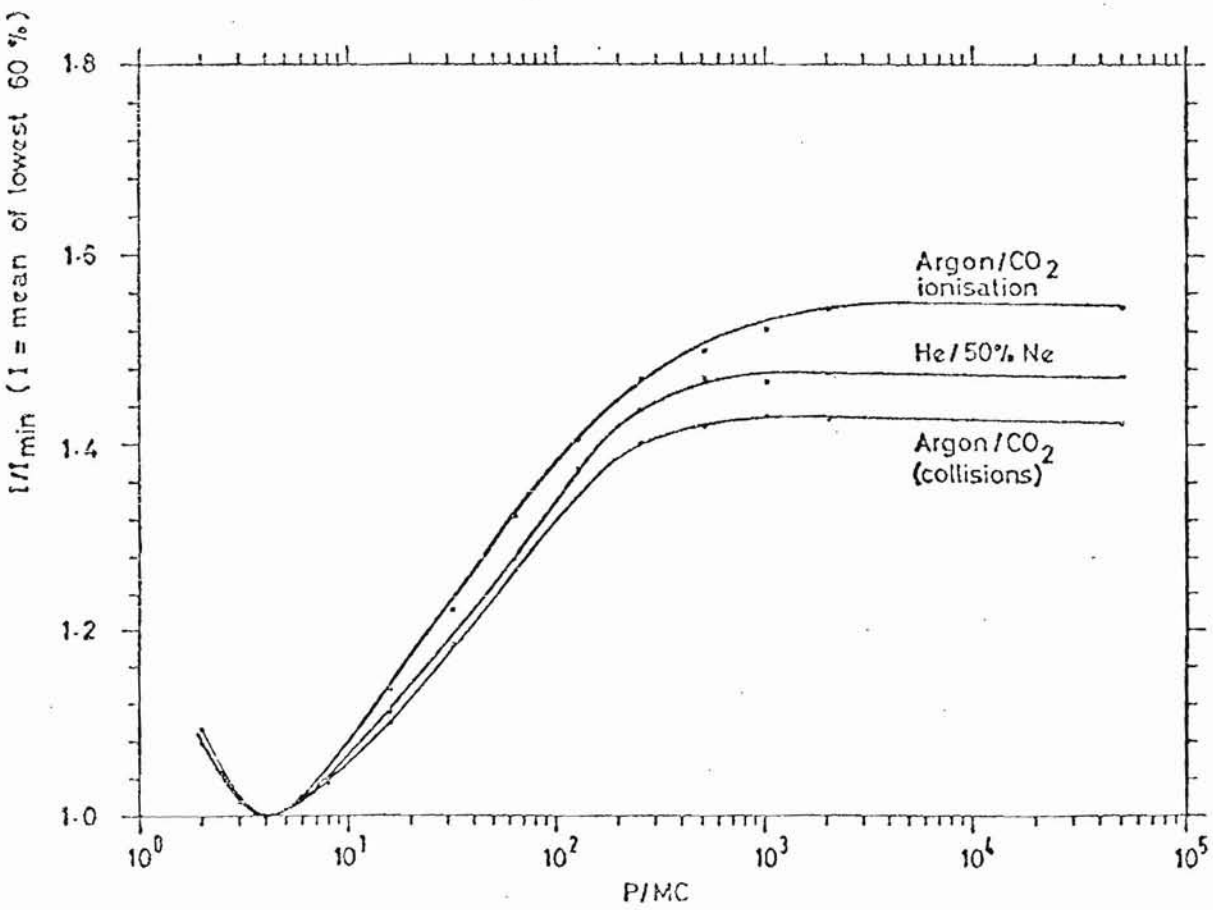

Theoretical relativistic rise curves (no. of collisions)
Fig. 5.13

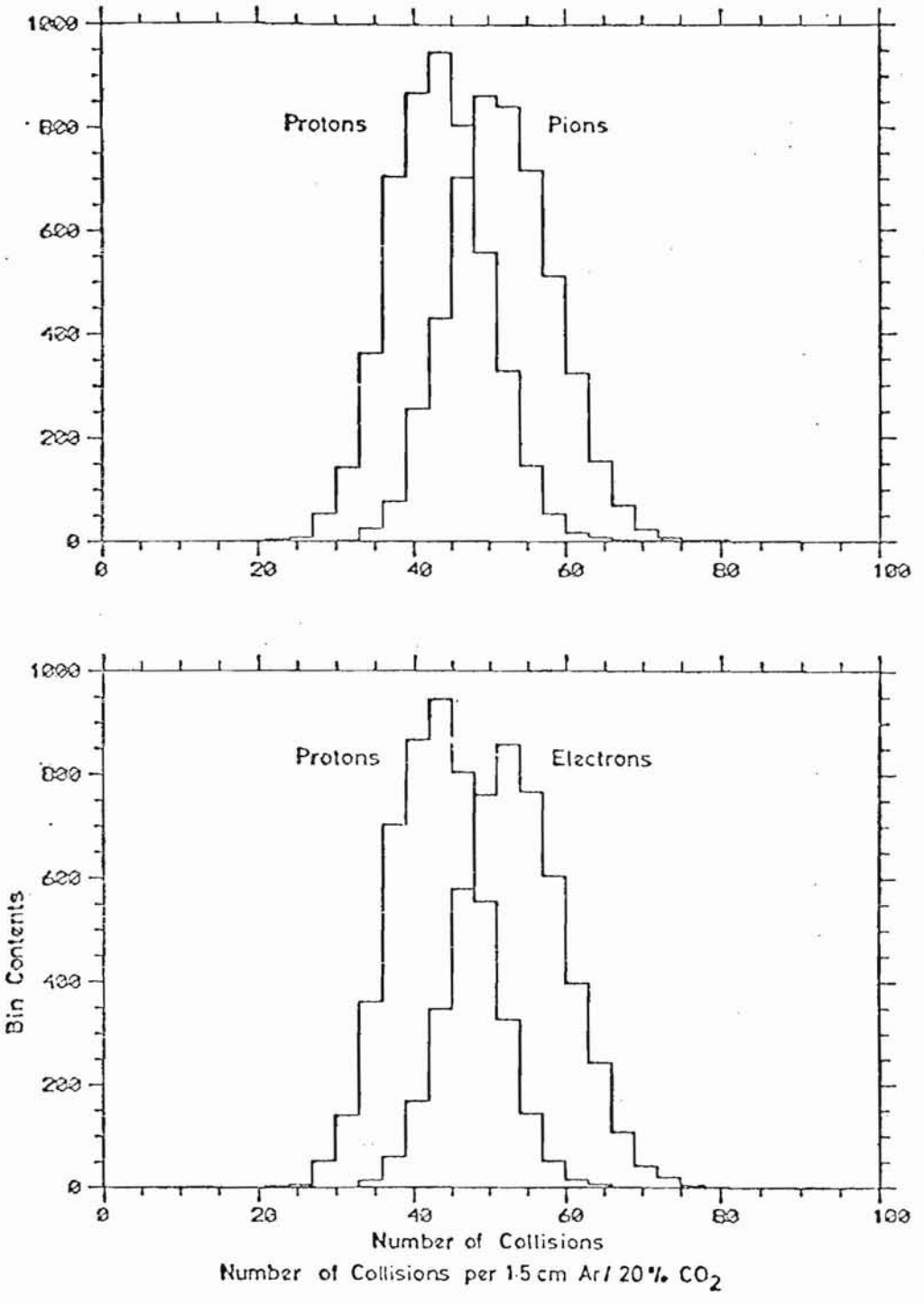
Protons
Pions
Protons
Electrons
Bin Contents
Number of Collisions
Number of Collisions per 1.5 cm Ar / 20 % CO_2

Fig.5.14

Table 5.1 shows that the relativistic rise is approximately the same if measured either in terms of the mean of the lowest 60% of samples, or in terms of the most probable ionization loss (which is in popular use). The most probable is defined here as the peak of a cubic that has been least squares fitted to that part of the Landau distribution above 25% of its peak value.

In Appendix I there will be found a more comprehensive list of the results of all Monte-Carlo calculations performed.

5.4 CONCLUSION

As will be seen, the comparison of the theory with experimental results (Chapter VI) produces good agreement between the two, and removes discrepancies that existed with previous theories. This gives credibility to the predictions, that have been made here, of particle identification properties for different gases. It shows that Argon is very likely an optimum gas for such purposes since it is both effective, practical and cheap.

CHAPTER VI

COMPARISON OF EXPERIMENT AND THEORY

VI.1 INTRODUCTION

This chapter's aim is to summarize, and to compare with theory, the results of various different experiments in which measurements have been made of the ionization loss of relativistic charged particles as they pass through thin samples of gas.

VI.2 COMPARISON OF EXPERIMENT AND THEORY

First, the difference between the results of Landau[4], Blunk and Leisegang[46] and Monte-Carlo calculations of theoretical probability distributions for the energy loss of 25 GeV/c protons in 1.5 cm Argon are shown in Fig.6.1. (The areas under the curves, in the range 1.5 to 6.5 keV, are normalized to each other.) The Blunk and Leisegang theory, which has not been referred to till now, is an attempted modification of the Landau theory to allow for the effects of atomic binding on the energy loss distribution. However, for very thin absorbers this approximation fails for similar reasons to the failure of the Landau theory in this region; (see p.81 and also reference (47) for further elucidation. Note, the agreement for thicker samples is good, e.g. see reference (1).)

In Fig.6.2 the Monte-Carlo fit to experimental measurements of 25 GeV/c protons in 1.5 cm Argon/20% CO_2 is shown. (Chamber resolution and cross-talk effects have been included in the theory; this has little effect on the theory as is also the case with the inclusion of the CO_2, thus making comparisons between Fig.6.1 and 6.2 possible.) Fig.6.2 is a repeat of Fig.4.27, where fits for other energies are also shown. As can be seen, the Monte-Carlo theory gives a very good fit to the shape of the probability distribution which would obviously not be the case with the other two theories shown in Fig.6.1. This is not surprising since, as has been stated previously, these other two theories contain assumptions which are explicitly stated not to hold in this region of thin absorber and high

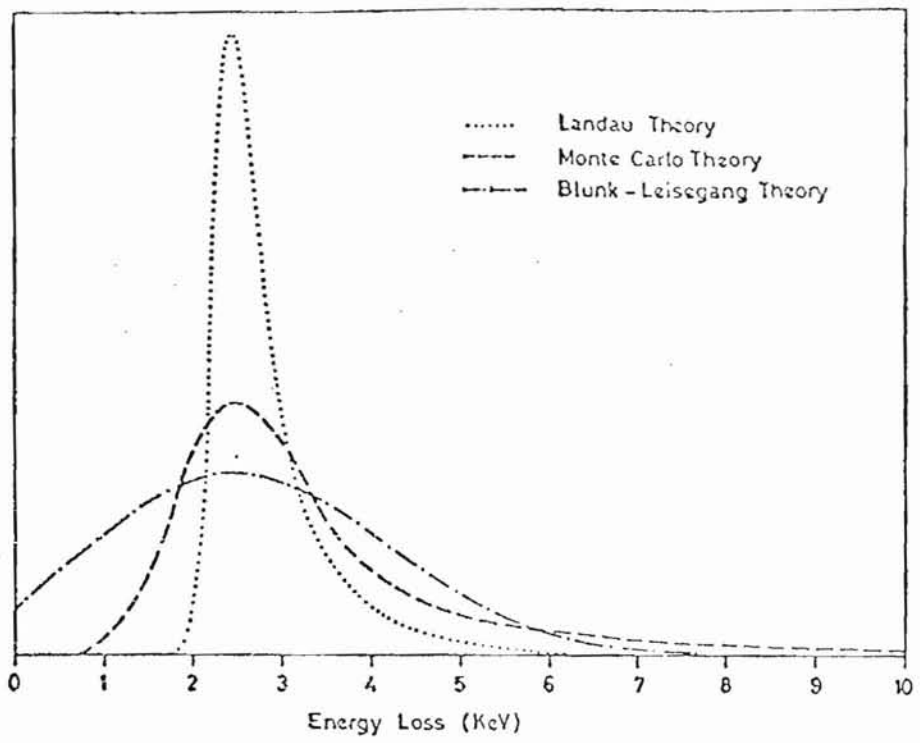

Fig. 6-1 Comparison of Theories for the Energy Loss Distribution of 25 GeV/c Protons Passing Through 1·5 cm Argon

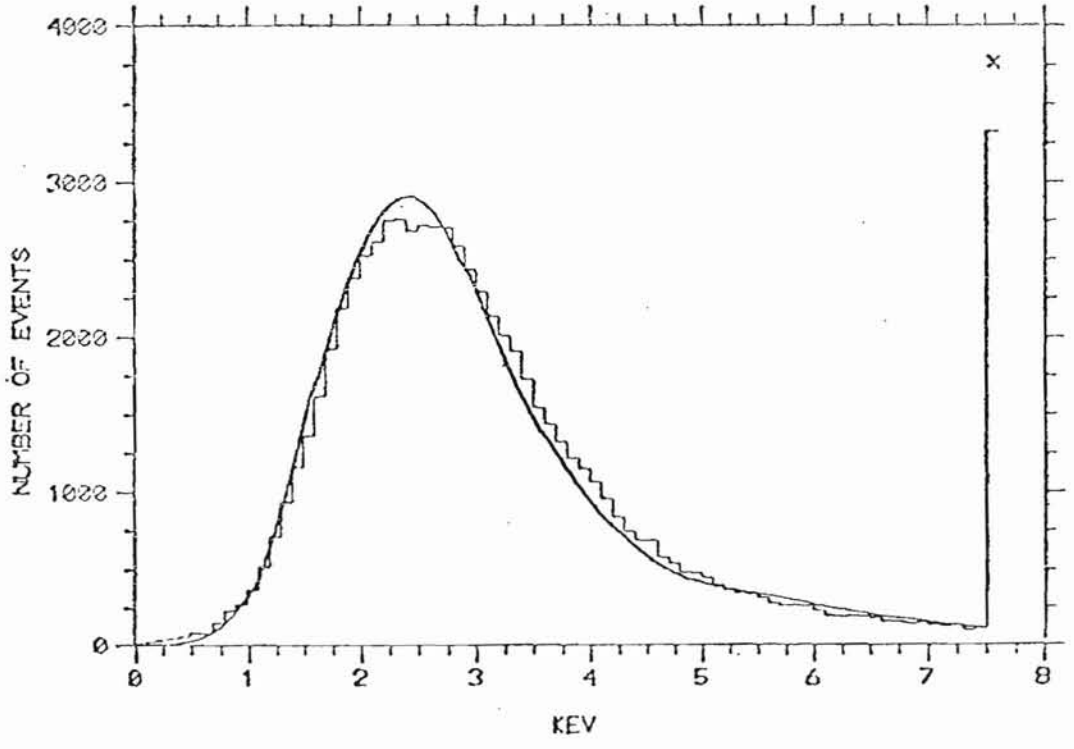

Fig.6.2
Comparison of Monte-Carlo theory (curve) with experiment for 25 GeV/c protons in a 1.5 cm sample of Argon/ 20% CO_2

velocity. However the comparison does serve to emphasize the need for a new calculation to explain this region.

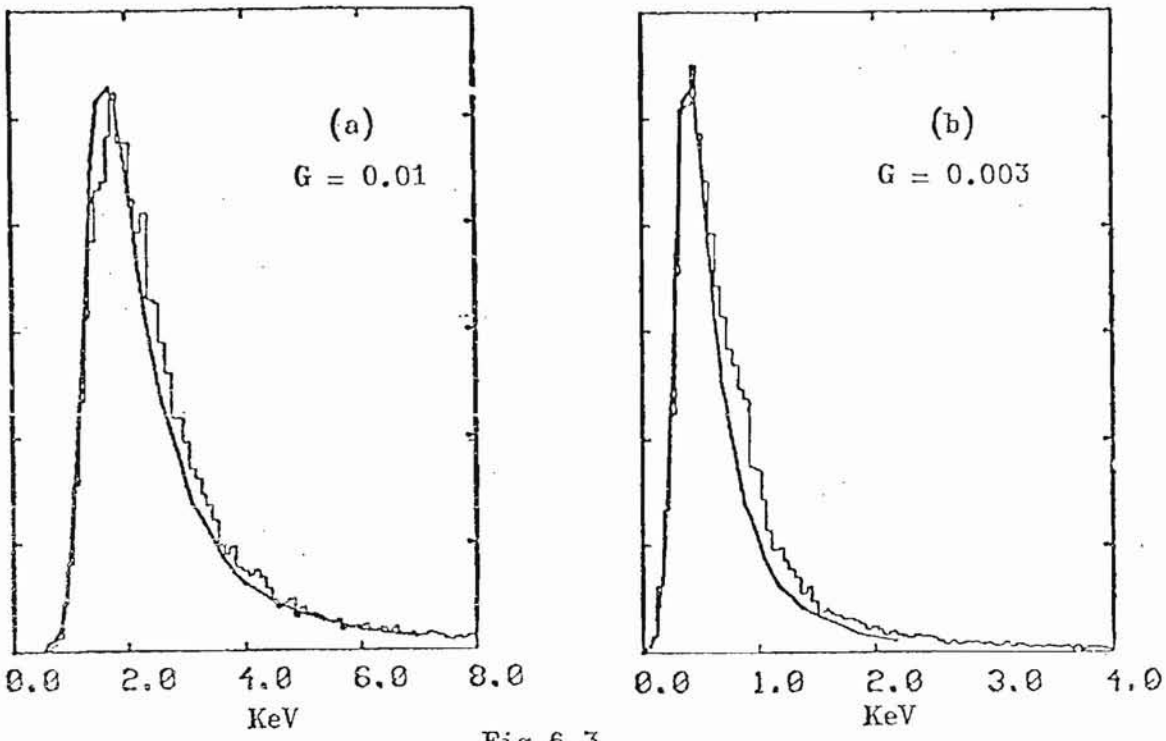

Fig.6.3
Comparison of Monte-Carlo theory (histogram)
with the Symon theory (curve)

To show that the Monte-Carlo theory agrees with other theories in the region where they are supposed to hold, a comparison of the Monte-Carlo theory with the Symon theory[48] is made. The Symon theory can be considered here as a convenient parametrization of the Landau theory. One of the parameters of the Symon theory is given by $G = \xi / \epsilon_{max}$ (see p.82 for definition of ξ and ϵ_{max}). The minimum value of G for which Symon's theory holds is given by G = 0.01, corresponding to the 'thinnest' absorbers (Note: G for Fig.6.2 is $\sim 10^{-6}$). Fig.6.3(a) shows a comparison of Monte-Carlo theory with Symon's theory for G = 0.01. Fig.6.3(b) shows a similar comparison for G = 0.003, which is now just outside the limits of the Symon theory, and where it can be seen that the Monte-Carlo theory has given a slightly wider distribution. Figs.6.3(a) and (b) were chosen because they were used to fit to yield curves in the experiment described in reference (49). This was an experiment in which 4.6 MeV alpha

particles were fired at a Nitrogen-15 gas target to study the reaction $N^{15}(\alpha, \gamma)F^{19}$. When extracting a yield curve for a particular resonance in F^{19}, allowance had to be made for the straggling of the incident α particle energy, hence the need to know the energy loss distribution. The Monte-Carlo curves gave slightly better fits but the difference from the Symon theory was too small, and the test not sensitive enough, to make any definite statements.

A criticism of the comparison made in Fig.6.2 is that the experimental data has been normalized in terms of energy (i.e. shifted along the x axis) to give the best fit to theory, since in this experiment, there was one unknown parameter (see p.70). This though does not invalidate the comparison between the shapes of the distributions. Three further comparisons are now shown of theoretical and experimental probability distributions where no free parameters are used either in experiment or theory.

Figures 6.4(a) - 6.4(d) show the comparison of theory with Xenon data as obtained in the SLAC experiment (Chapter II). As has been mentioned, even though the fits are good, the absolute position of the experimental peaks is uncertain to 9% but the width of the distribution is good to < 1%. Figs.6.5(a) - 6.5(d) show another comparison with Xenon data from an experiment by Willis et al[50]. Again quite good agreement is obtained. The agreement seems better for Figs.6.5(a) and (b) than for Figs.6.5(c) and (d). A possible reason for this is the choice of gas mixture used for the data of the latter two figures, (i.e. 41% Xe / 41% He / 18% Methylal). Xenon and Helium have very different densities and it is thought that this probably resulted in a mixing problem, hence changing the effective composition of the gas. (Note, for the sake of completeness, the binding energies used for Methylal in this theory calculation were the same as those of Carbon dioxide as given in Table 5.1, plus that of Hydrogen (13.6 eV). These binding energies are those for isolated

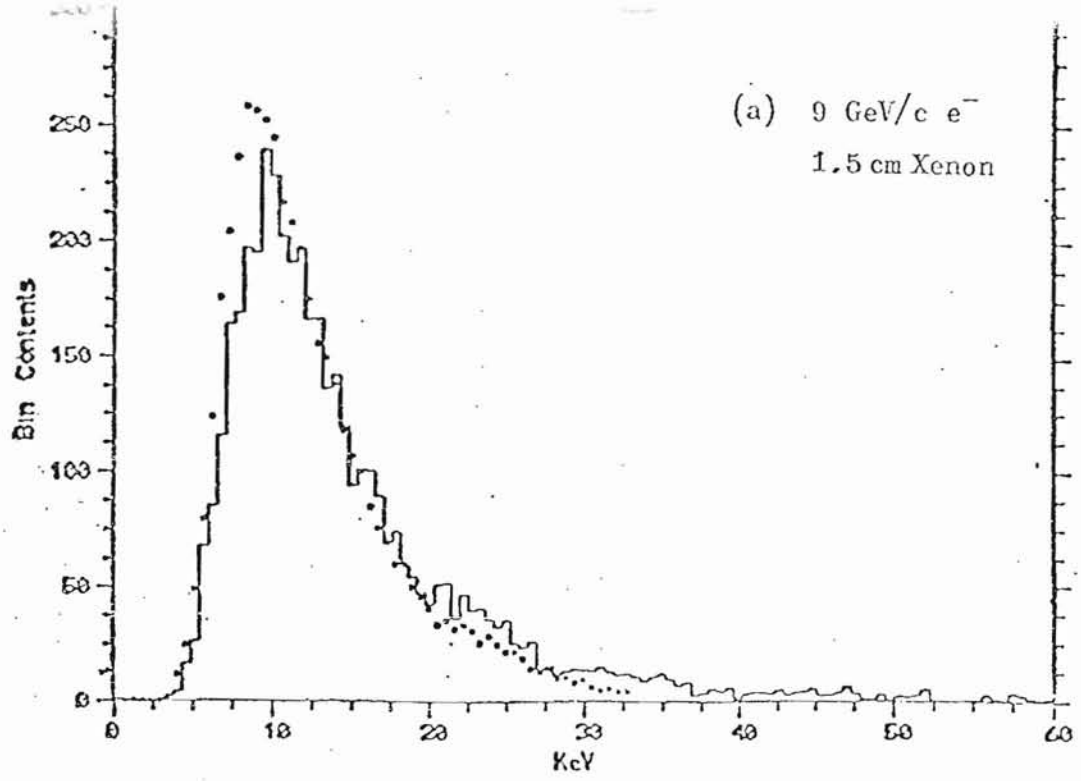

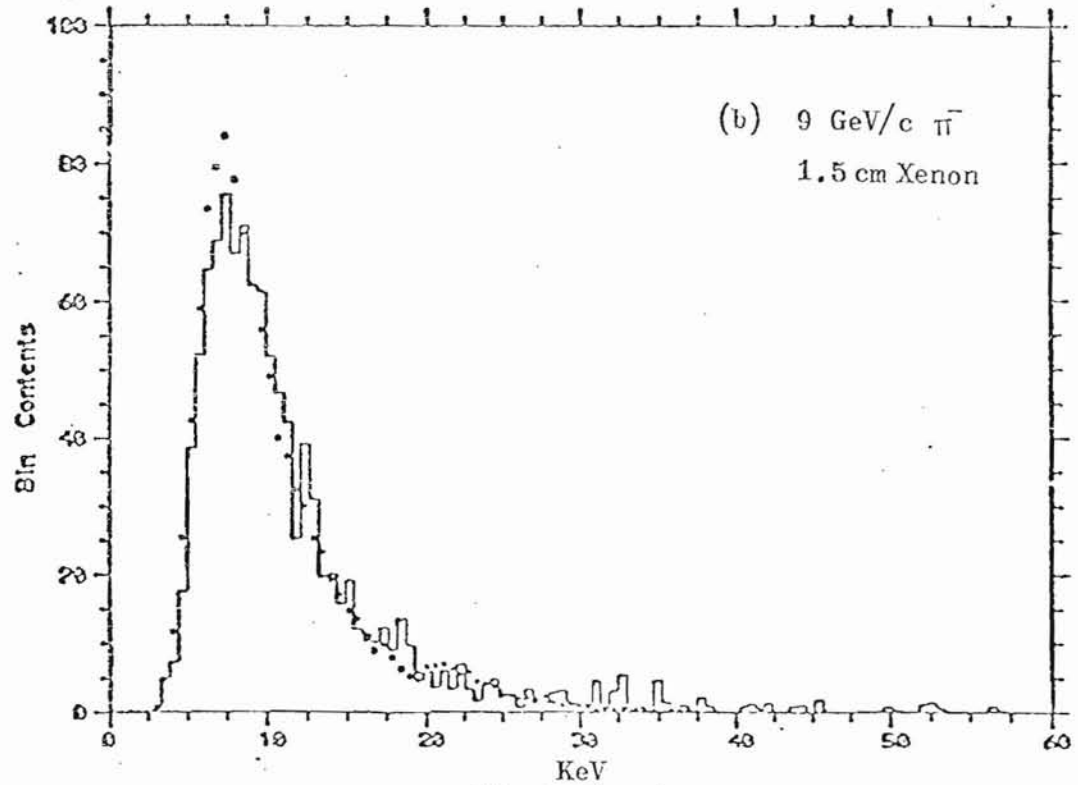

Fig.6.4(a,b)
Comparison of Monte-Carlo theory (crosses)
with the SLAC experiment

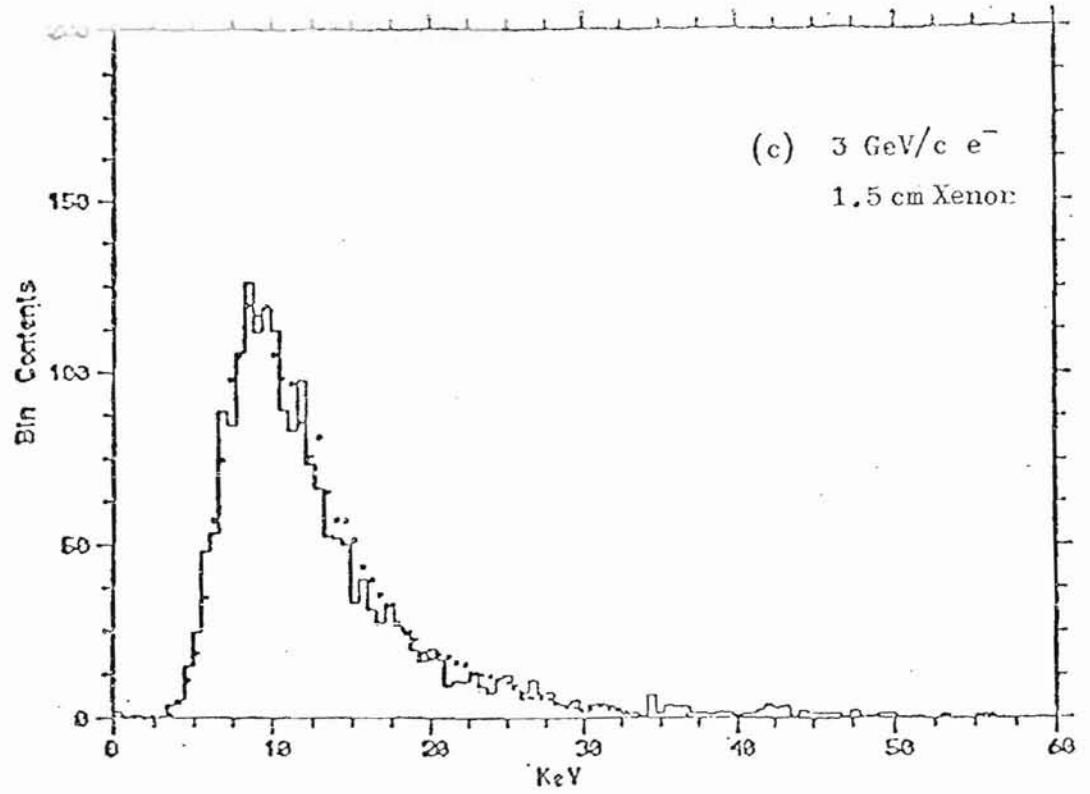

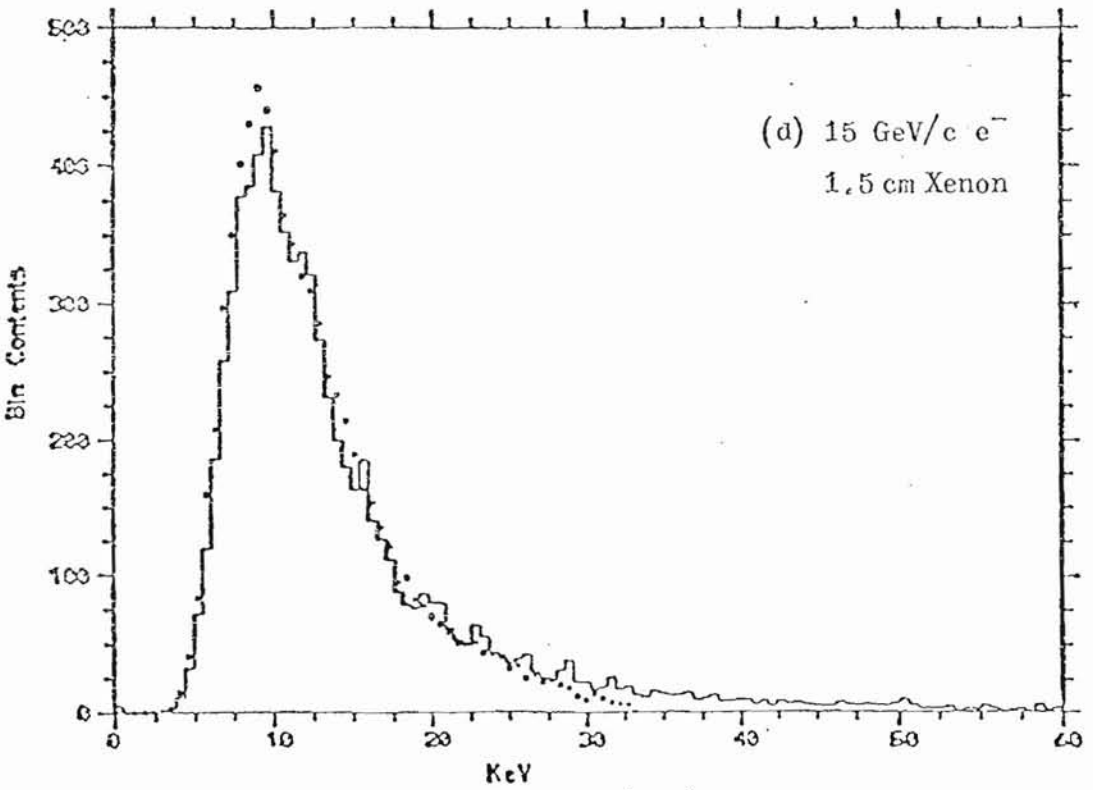

Fig.6.4(c,d)
Comparison of Monte-Carlo theory (crosses)
with the SLAC experiment

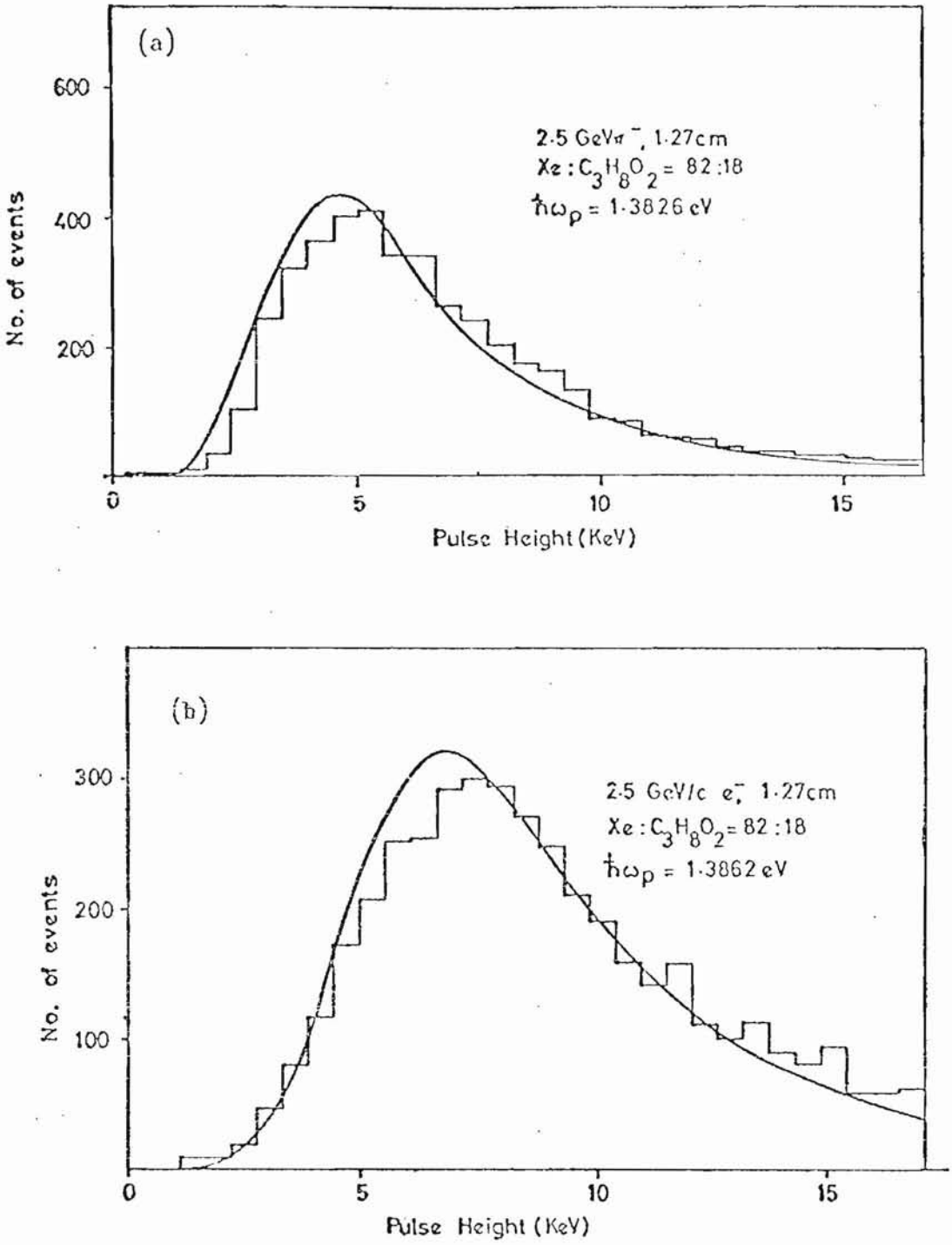

Fig.6.5(a,b)
Comparison of Monte-Carlo theory (curve)
with experiment by Willis et al[50]

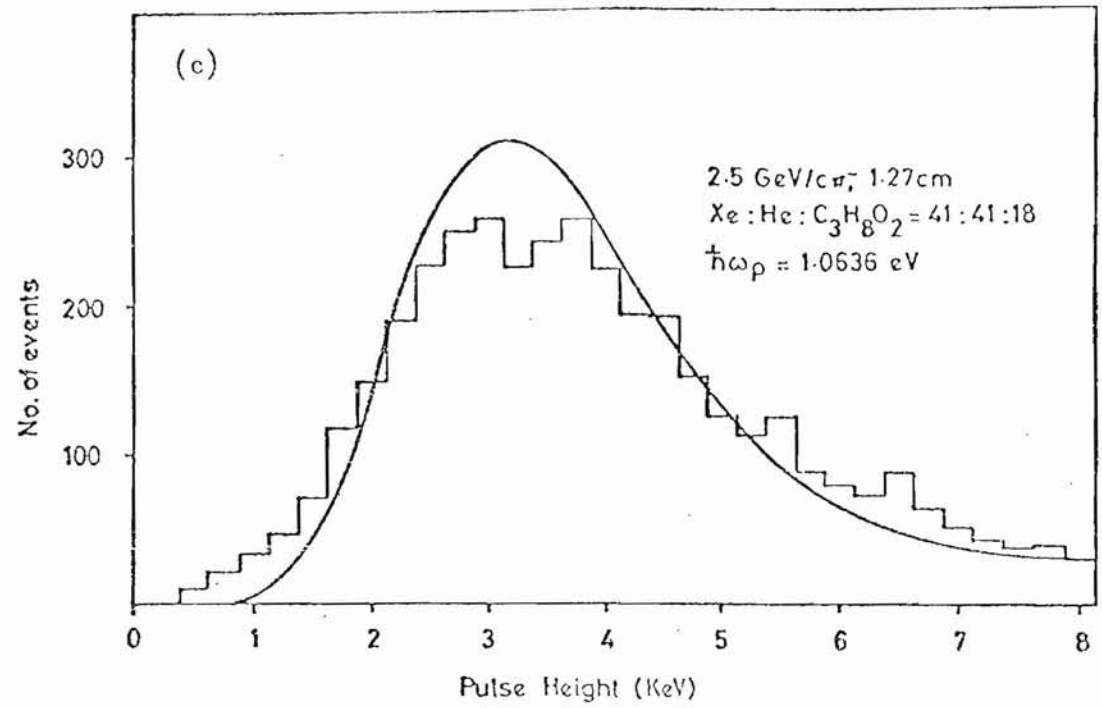

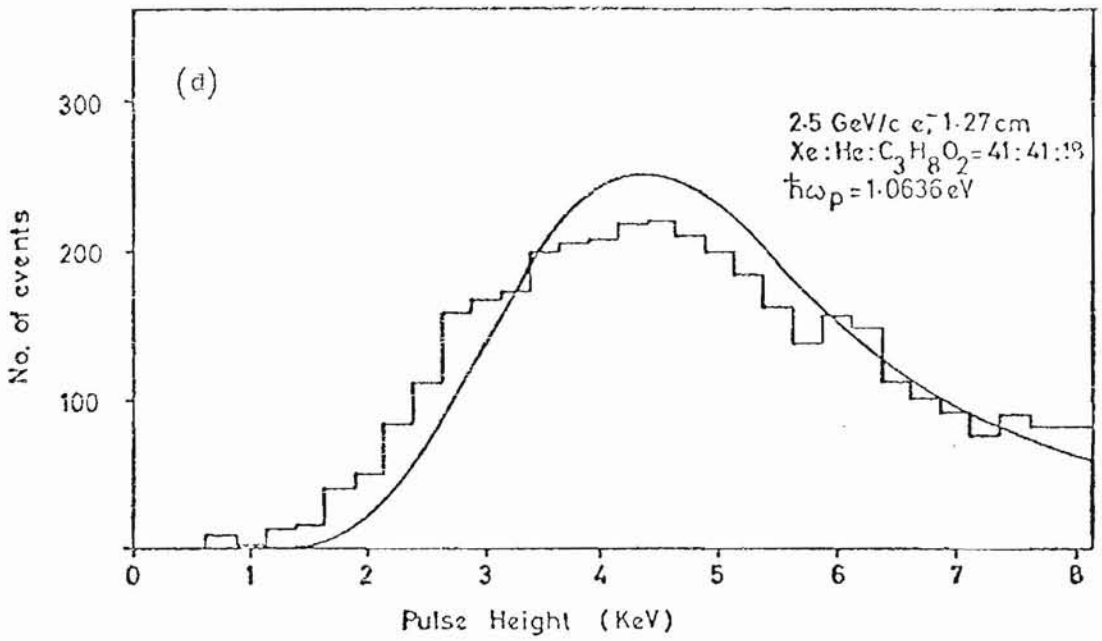

Fig.6.5(c,d)
Comparison of Monte-Carlo theory (curve)
with experiment by Willis et al(50)

atoms. Molecular effects are ignored.) Figs.6.6(a) - 6.6(d) show a comparison, as made by Cobb[3], with Argon data obtained from an experiment by Harris et al[1]. Quite good agreement is obtained.

A comparison is now made of the relativistic rise curve obtained from theory and that obtained from many different experiments. This is complicated by the fact that different experiments have used different gas mixtures and sample thicknesses from each other. A relatively crude comparison is made of all the data available from experiments that have used a thin sample (i.e. 1-20 cm) of a gas mixture, which consisted predominantly of Argon. This is shown in Fig.6.7. As can be seen, instead of plotting straightforward ionization loss (I), the ratio of I / I_{min} was plotted against p/m_0c, hence removing almost completely normalization problems between detectors of different thicknesses etc. The continuous curve is the Monte-Carlo theory prediction and the dotted line is the Sternheimer calculation[44,51]. As can be seen, the Sternheimer calculation gives too much relativistic rise when compared with these experimental points for thin samples. (However, the agreement is good for thick samples, solids, etc., e.g. see reference (53).) This Sternheimer calculation is of the most probable energy loss as calculated by Landau (after a small correction[54] has been made to his original calculation[4]), modified to allow for the density effect due to the dielectric properties of the medium. The effect of the medium is represented classically by a series of dispersion oscillators, the values of the parameters involved (i.e. ionization potentials) being chosen to give agreement with experimentally determined values of mean ionization potential. For the same reasons as for the breakdown of the Landau theory for thin samples (p. 81), the Sternheimer calculation cannot be applied to thin samples.

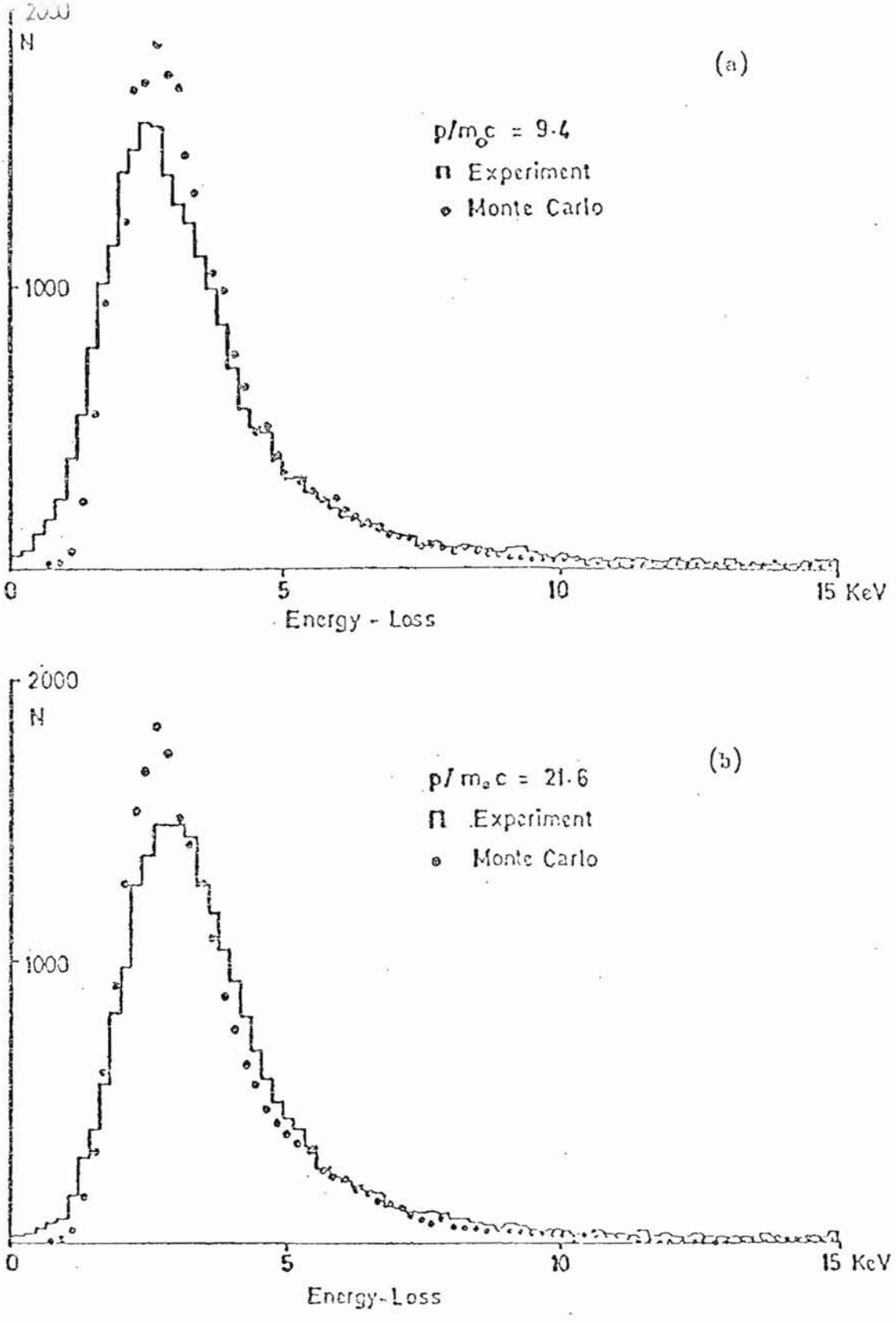

Fig.6.6(a,b)
Comparison between simulated and experimentally observed energy-loss distributions in 1.7 cm of Argon for
(a) 1.3 GeV/c π^- ; (b) 3.0 GeV/c π^-
The pairs of distributions are normalized in the range 1-8 KeV. Experimental data from Harris et al(1)

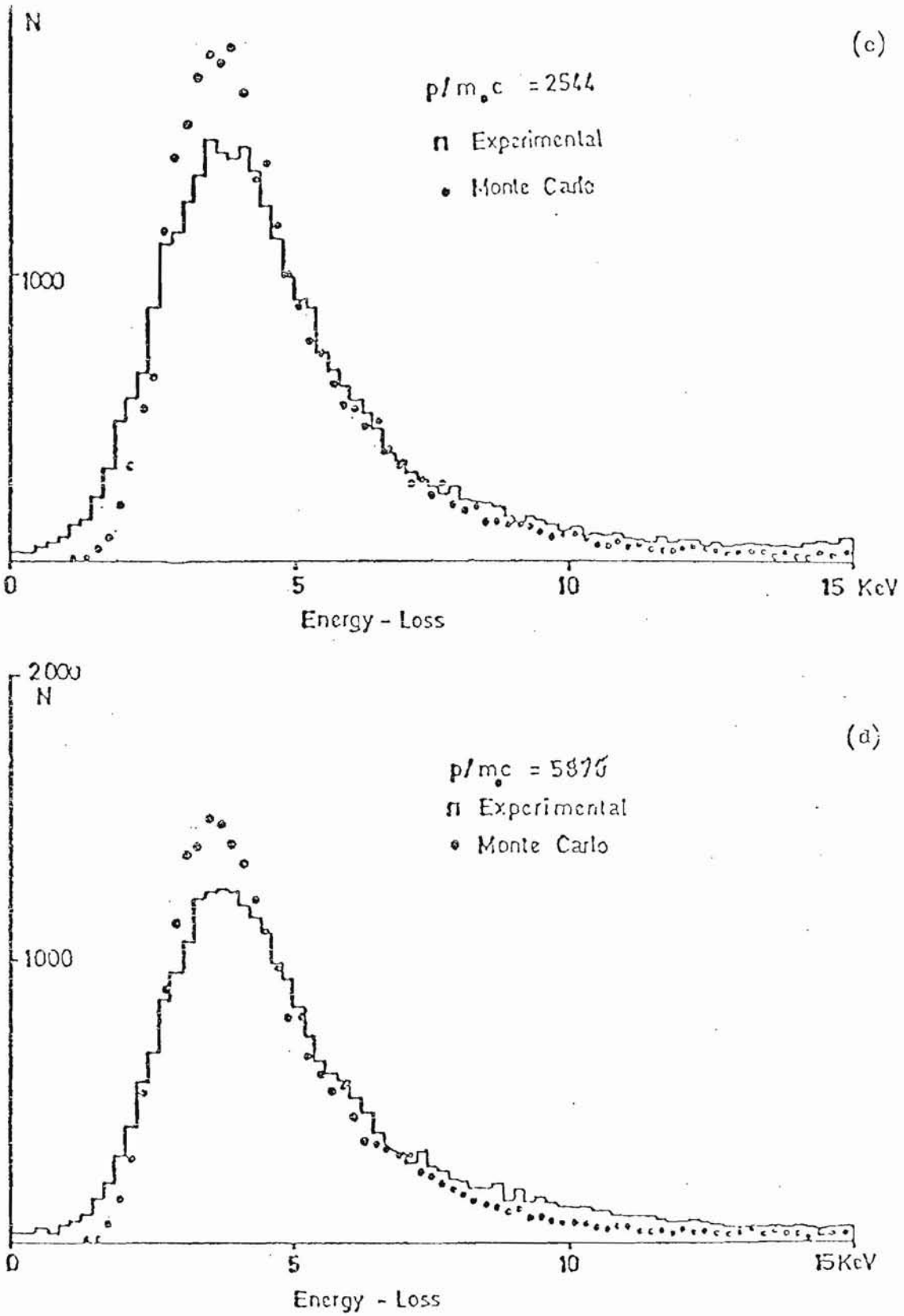

Fig.6.6(c,d)
Comparison between simulated and experimentally observed energy-loss distributions in 1.7 cm of Argon for (c) 1.5 GeV/c e^- ; (d) 5.0 GeV/c e^-
The pairs of distributions are normalized in the range 1-8 KeV. Experimental data from Harris et al(1)

Fig. 6 7

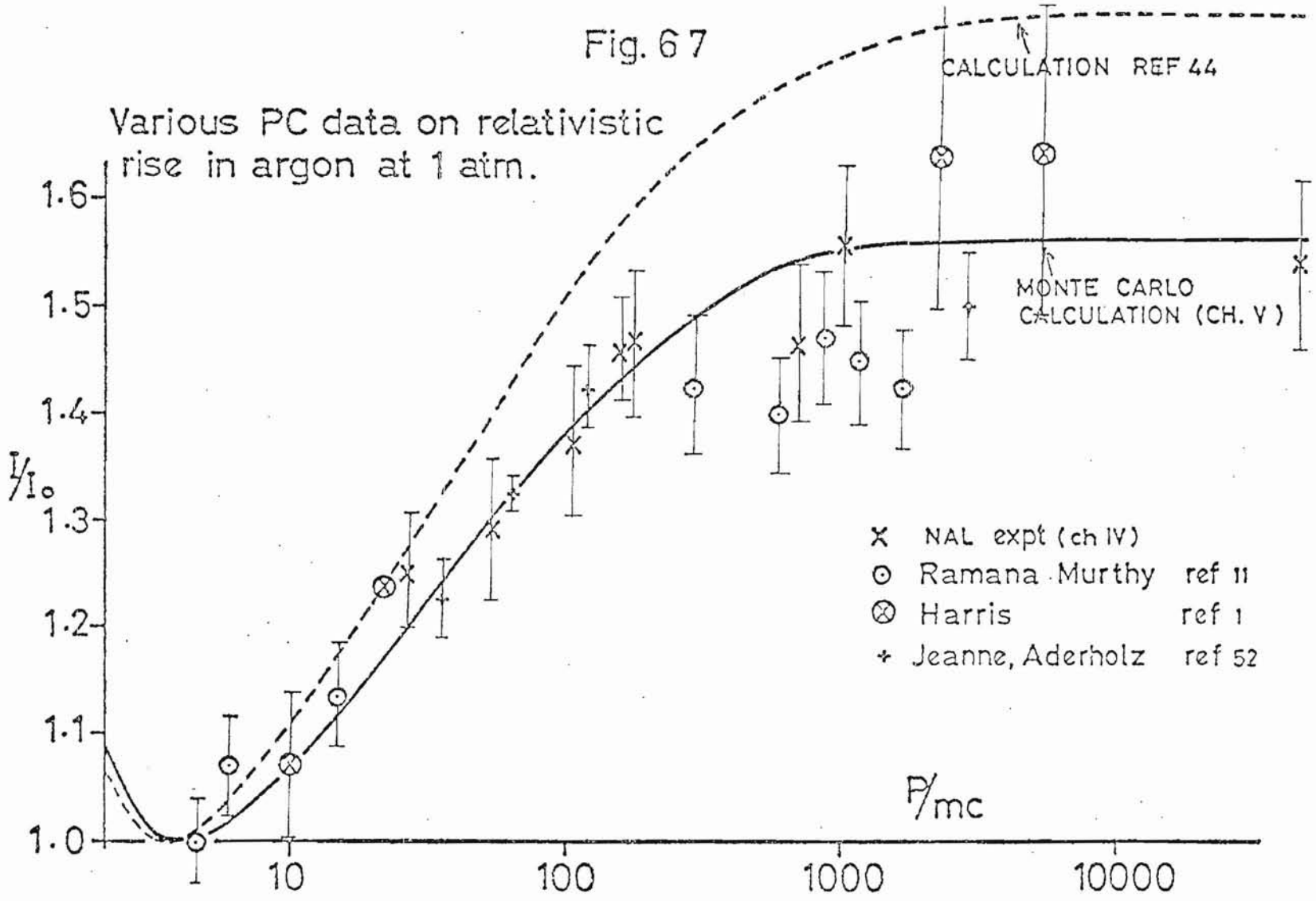
Various PC data on relativistic rise in argon at 1 atm.
CALCULATION REF 44
MONTE CARLO CALCULATION (CH. V)
I/I₀
P/mc
1.0
1.1
1.2
1.3
1.4
1.5
1.6
10
100
1000
10000
NAL expt (ch IV)
Ramana Murthy ref 11
Harris ref 1
Jeanne, Aderholz ref 52

~~In Fig.6.7, error bars have not been included.~~ The errors on the relativistic rises from the various experiments shown, are all of order ± 4% apart from the Ramana Murthy data which is of order ±9%. The general agreement of the data with Monte-Carlo theory seems very reasonable considering the comparative crudity of this comparison.

VI.3 CONCLUSION

The Monte-Carlo predictions fit experimental results fairly well in terms of the shape and position of the ionization loss distribution for thin samples of gas. For thicker samples of gas and lower particle velocities, where other theoretical solutions hold, Monte-Carlo theory agrees with them.

More precise comparisons of theory with experiment would require investigations into the validity of the assumption that the mean energy per ion pair created is a constant. Also, improvements in the theoretical model to give a physically more real interpretation of the dielectric properties of the medium, and to allow for molecular effects, etc., could be made. However the results so far obtained are felt to be very satisfactory.

APPENDIX A.1

MONTE-CARLO RESULTS

This appendix contains a complete list of the results of the theoretical predictions from the Monte-Carlo calculations performed. It is from subsets of these results that Table 5.1 and Figs.5.10 to 5.13 were generated. The atomic energy levels and plasma frequencies used in the calculations are listed in Table 5.2.

In order to explain the tables following, reference is made to Fig. 1.5. On the left of Fig.1.5 will be seen two probability distributions as generated by the first Monte-Carlo program (see p.95). Tables A1.1 and A1.2 respectively, refer to the peak and full width at half maximum of such probability distributions. On the right of Fig.1.5 will be seen two mean of the lowest 60% distributions as generated by the second Monte-Carlo program (i.e. the multi-sampling program - see p.95; for the definition of mean of the lowest 60%, see p.96). Tables A1.3 and A1.4 respectively refer to the peak and full width at half maximum of such mean distributions.

All the results presented in these tables following are for 1.5 cm gas samples. The results in Tables A1.3 and A1.4 are those that would be obtained by a 500 cm detector, in which there was no cross talk between any of its 333 samples.

It should be pointed out that the results of Table A1.2 are subject to errors possibly as large as ±5% (due to problems associated with the finite bin size used to plot the probability distributions from which the FWHM 's were obtained). This problem does not occur in any of the other four tables, where the errors in the determination of the results are ~~negligible~~ of order ±1%.

TABLE A1.1

Gas	p/m_0c	Peak (eV) of Landau distribution for 1.5cm gas samples														
		2	3	4	5	6	8	16	32	64	128	256	512	1024	2048	50000
Helium		309	281	275	278	276	285	309	325	348	372	384	389	387	390	390
Neon		1236	1137	1117	1142	1147	1156	1278	1380	1504	1616	1683	1724	1731	1757	1760
Argon		2200		2062			2157	2302	2495	2734	2891	2997	3103	3161	3116	3168
Krypton		4250		3921			4096	4482	4905	5296	5699	5927	6156	6266	6271	6365
Xenon		5743		5339			5658	6153	6704	7271	7878	8387	8726	9002	9098	9242
Methane		1605	1485	1459	1478	1481	1507	1632	1744	1849	1916	1965	1988	1999	1994	1992
Ammonia		1527	1408	1390	1403	1411	1433	1543	1664	1788	1855	1905	1936	1957	1964	1970
Nitrogen		2042		1858			1938	2087	2255	2421	2570	2673	2703	2756	2757	2743
Argon/CO_2(20%)		2410		2244			2330	2517	2713	2905	3096	3256	3363	3371	3409	3404
Carbon Dioxide		3279	3032	3014	3047	3063	3145	3374	3668	3895	4110	4263	4354	4360	4370	4394

TABLE A1.2

Gas	FWHM (eV) of Landau distribution for 1.5cm gas samples														
p/m_oc	2	3	4	5	6	8	16	32	64	128	256	512	1024	2048	50000
Helium	215	195	188	205	206	213	242	250	260	277	262	284	288	286	291
Neon	920	853	831	783	877	870	969	997	1167	1287	1388	1358	1342	1481	1427
Argon	1618		1475			1655	1759	1778	1937	1978	2086	2178	2158	2149	2195
Krypton	3385		3182			3169	3468	3745	3886	4344	4693	4631	4600	4727	5123
Xenon	4277		3922			4350	4658	4991	5449	5922	6122	6445	7438	7339	7367
Methane	1003	954	959	960	971	948	987	1075	1089	1148	1213	1181	1291	1156	1164
Ammonia	1084	1022	973	988	994	1029	1040	1066	1156	1233	1220	1259	1334	1329	1359
Nitrogen	1461		1338			1425	1496	1552	1624	1606	1822	1825	1849	1817	1818
Argon/CO_2(20%)	1706	1640	1551	1623	1581	1775	1812	1823	1872	2038	2175	2188	2269	2288	2393
Carbon Dioxide	1976	1720	1847	1993	1980	1972	2048	2051	2217	2351	2332	2534	2565	2505	2597

TABLE A1.3

Gas	Peak (eV) of mean of lowest 60% distribution for 333 x 1.5cm samples														
p/m_oc	2	3	4	5	6	8	16	32	64	128	256	512	1024	2048	50000
Helium	283	259	254	254	254	260	277	298	319	342	355	358	357	358	359
Neon	1232	1139	1115	1131	1142	1165	1263	1359	1476	1583	1648	1696	1710	1719	1714
Argon	2143		1961			2057	2214	2408	2602	2783	2901	2995	3039	3049	3095
Krypton	4220		3886			4059	4407	4788	5163	5546	5762	5978	6102	6135	6199
Xenon	5784		5323			5606	6107	6655	7186	7734	8216	8581	8778	8939	9025
Methane	1559	1441	1417	1423	1438	1456	1574	1685	1790	1851	1894	1918	1927	1927	1922
Ammonia	1489	1370	1356	1361	1371	1401	1493	1615	1731	1797	1853	1876	1889	1892	1889
Nitrogen	1953		1778			1849	1994	2154	2311	2452	2531	2568	2618	2635	2636
Argon/CO_2(20%)	2352		2152			2247	2443	2633	2847	3022	3162	3227	3275	3321	3325
Carbon Dioxide	3196	2952	2915	2935	2960	3018	3246	3523	3771	3969	4102	4167	4203	4217	4226

TABLE A1.4

Gas	p/m_oc	FWHM (%) of mean of lowest 60% distribution for 333 x 1.5cm gas samples														
		2	3	4	5	6	8	16	32	64	128	256	512	1024	2048	50000
Helium		5.12	5.33	5.23	5.37	5.27	5.22	5.19	5.15	5.05	4.84	4.63	4.75	4.98	4.96	4.91
Neon		5.38	5.58	5.44	5.45	5.41	5.32	5.31	5.28	5.11	4.96	4.92	4.97	5.21	5.34	5.20
Argon		5.05		5.26			5.03	5.02	4.83	4.70	4.74	4.80	4.77	4.80	4.74	4.81
Krypton		5.09		5.24			4.98	4.90	4.66	4.68	4.65	4.60	4.57	4.58	4.50	4.66
Xenon		5.45		5.48			5.38	5.30	5.23	5.12	5.04	5.05	5.01	4.97	4.96	5.05
Methane		3.81	4.00	3.86	3.92	3.88	3.81	3.79	3.73	3.60	3.59	3.53	3.58	3.79	3.81	3.89
Ammonia		4.19	4.36	4.23	4.21	4.18	4.19	4.10	4.02	3.98	3.85	3.79	3.88	4.10	4.11	4.07
Nitrogen		4.48		4.63			4.47	4.34	4.20	4.12	4.10	4.20	4.17	4.15	4.07	4.06
Argon/CO_2(20%)		4.76		4.92			4.77	4.68	4.52	4.44	4.47	4.47	4.47	4.52	4.47	4.53
Carbon Dioxide		3.86	4.03	3.94	3.97	3.90	3.90	3.80	3.79	3.59	3.57	3.48	3.55	3.67	3.77	3.74

REFERENCES

(1) HARRIS, F. et al., Nucl. Instr. & Methods, 107, 413 (1973).

(2) YUAN, L.C.L. et al., Nucl. Instr. & Methods, 130, 41 (1975).

(3) COBB, J.H., D.Phil. Thesis, University of Oxford, (1975).

(4) LANDAU, L., J. Phys. (USSR), 8, 201 (1944). Also reproduced in 'Collected Papers of Landau'; Ed. Ter Haar, (Gordon and Breach, London), (1965).

(5) JACKSON, J.D., 'Classical Electrodynamics', Wiley, p.432

(6) ROSSI, B., 'High Energy Particles', Prentice Hall, New Jersey, (1952).

(7) LIVINSTON, M.S. and BETHE, H.A., Rev. Mod. Phys., 9, 245 (1937).

(8) PALLADINO, V., and SADOULET, B., Nucl. Instr. & Methods, 128, 323 (1975).

(9) WILKINSON, D.H., 'Ionization Chambers and Counters', Cambridge University Press, (1950).

(10) CHARPAK, G., Ann. Rev. Nucl. Sci., 20, 195 (1970).

(11) RAMANA-MURPHY, P.V., Nucl. Instr. & Methods, 63, 77 (1968).

(12) LEHRAUS, I. and JEANNE, D., Nucl. Instr. & Methods, 93, 257 (1971).

(13) JEANNE, D. et al., Nucl. Instr. & Methods, 111, 287 (1973).

(14) ADEMOLZ, M. et al., Nucl. Instr. & Methods, 118, 419 (1974).

(15) ALLISON, W.W.M. et al, Nucl. Instr. & Methods, 119, 499 (1974).

(16) KATSURA, T., Ph.D. Thesis, University of Hawaii, (1975).

(17) BUNCH, J.N., 'Calibration of MWPC's in SLAC Transition Radiation Experiment' (Internal note - unpublished).

(18) PARKER, S.I. et al., Nucl. Instr. & Methods, 97, 181 (1971).

(19) See reference (15)

(20) LLOYD, J.L., Personal communication.

(21) ALLISON, W.W.M., Oxford Nuclear Physics Lab. Preprint No.68/75. Also to be published in Nucl. Instr. & Methods. (1976).

(22) GARIBYAN, G.M. and ISPIRYAN, K.A., JETP Letts., 16, 585 (1972).

(23) ALLISON, W.W.M., ISIS Internal Note No.26 (unpublished).

(24) FLEMING, R.W., ISIS Internal Note No.11 (unpublished).

(25) ALLISON, W.W.M., ISIS Internal Note No.23 (unpublished).
COBB, J.H., ISIS Internal Notes, 1,2,8. Also see ref. (3).

(26) FLEMING, R.W., ISIS Internal Notes, 18 and 20. (unpublished).

(27) PRUSS, S.M., NAL Report No. TM-470.

(28) BENOT, et al., Nucl. Instr. & Methods, 105, 431 (1972).

(29) See reference (10), p.232.

(30) COBB, J.H., ISIS Internal Notes 9 and 12 (unpublished)
Also see reference (3).

(31) BLEANEY, B.I. and BLEANEY, B., 'Electricity and Magnetism' 2nd ed. (O.U.P.) p.55.

(32) LLOYD, J.L. and WOLFENDALE, A.W., Proc. Phys. Soc., 73, 178 (1959).

(33) See reference (14), Fig.7.

(34) SMITH, G.C. and MATHIESON, E., Nucl. Instr. & Methods, 131, 13 (1975).

(35) COBB, J.H. et al., Oxford Nuclear Physics Lab. Preprint No.67/75; Also to be published in Nucl. Instr. & Methods. (1976).

(36) ISPIRIAN,K.A.,et al., Nucl. Instr. & Methods, 117, 125 (1974)

(37) FANO, V., Ann. Rev. Nucl. Sci., 13, 1 (1963).

(38) CRISPIN, A. and FOWLER, G.N., Rev. Mod. Phys., 42, 290 (1970).

(39) FANO, V. and COOPER, J.W., Rev. Mod. Phys., 40, 441 (1968).

(40) BHABHA, H.J., Proc. Roy. Soc., A164, 257 (1938).

(41) JESSE, W.P. and SADAUSKIS, J., Phys. Rev., 97, 1668 (1955)
107, 766 (1956).

(42) ONUCHIN, A.P. and TELNOV, V.I., Nucl. Instr. & Methods, 120, 365 (1974).

(43) RAMANA-MURTHY, P.V. and DEMEESTER, G.D., Nucl. Instr. & Methods, 56, 93 (1967).

(44) STERNHEIMER, R.M. and PIERLS, R.F., Phys. Rev., B3, 3681 (1971).

(45) DAVIDENKO, V.A, Nucl. Instr. & Methods, 67, 325 (1969).

(46) BLUNCK, O. and LEISEGANG, S., Zeit. fur Phys., 128, 500 (1950)
BLUNCK, O. and WESTPHAL, K. Zeit. Fur Phys., 130, 641 (1951).

(47) KNOP, G. et al., Zeit. fur Phys., 165, 533 (1961).

(48) See reference (6)

(49) SYMONS, T.J.M., D.Phil. Thesis, University of Oxford, (1976).

(50) WILLIS, W.J. et al., Nucl. Instr. & Methods, 127, 525 (1975).

(51) STERNHEIMER, R.M., Phys. Rev., 88, 851 (1952).

(52) See references (13) and (14).

(53) BELLAMY, E.H. et al., Phys. Rev., 164, 164 (1967).

(54) MACCABEE, H.D. and PAPWORTH, D.G., Phys. Letts., 30A, 241 (1969).

(55) POWELL, C.J., Rev.Mod.Phys., 48, 33 (1976) (see fig. 10).